

**MICROFLUIDIC-BASED TOOLS TO INVESTIGATE GENE  
EXPRESSION AND REGULATION WITH TISSUE-SPECIFICITY  
DURING AGING IN *CAENORHABDITIS ELEGANS***

A Dissertation  
Presented to  
The Academic Faculty

by

Jason H. Wan

In Partial Fulfillment  
of the Requirements for the Degree  
Doctor of Philosophy in the  
Wallace H. Coulter Department of Biomedical Engineering

Georgia Institute of Technology & Emory University  
May 2022

**COPYRIGHT © 2022 BY JASON H. WAN**

**MICROFLUIDIC-BASED TOOLS TO INVESTIGATE GENE  
EXPRESSION AND REGULATION WITH TISSUE-SPECIFICITY  
DURING AGING IN *CAENORHABDITIS ELEGANS***

Approved by:

Dr. Hang Lu, Advisor  
School of Chemical & Biomolecular  
Engineering  
*Georgia Institute of Technology*

Dr. Patrick Phillips  
Department of Biology  
*University of Oregon*

Dr. Ahmet Coskun  
Department of Biomedical Engineering  
*Georgia Institute of Technology*

Dr. Shuichi Takayama  
Department of Biological Engineering  
*Georgia Institute of Technology*

Dr. Annalise Paaby  
School of Biological Sciences  
*Georgia Institute of Technology*

Date Approved: April 12, 2022

To 媽媽 and 爸爸 for everything and anything

## ACKNOWLEDGEMENTS

This dissertation would not be possible without the guidance, support, and love from so many people. I first want to thank my advisor, Hang Lu, who gave me an opportunity to grow into the researcher I am today. Her mentorship, support, and advice tremendously impacted and shaped me and my work, and I truly cannot thank her enough. I would also like to thank my committee members for providing constructive feedback and guidance to improve the quality of this dissertation. Additionally, during my time at the University of Wisconsin - Madison, I was an undergraduate researcher in the John Yin lab; without both his and my amazing mentor Bahar Inankur's encouragement, I certainly would not be where I am today.

I would like to thank all my lab mates in the Lu Lab, both past and present, for their invaluable support, insightful feedback, and all the good times both inside and outside of EBB. I want to particularly thank Gongchen Sun and Dhaval Patel for their patient mentorship – especially during the beginning of my PhD experience – and lifelong friendships. Thank you to Kim Le and Jimmy Ding for your support in both lab-related and countless food-related collaborations. Additionally, I want to thank my amazing undergraduate researchers, especially Jocelyn Dient, for their hard work and dedication.

This thesis would not be possible without the support of my friends and family over these past years. Special thanks to Thomas Turner who made every weekend fun. Thank you to Xiaohu for being absolutely adorable. Thank you to Thomas and Jess Wan for your love and enthusiasm about worms. Finally, thank you to Mom and Dad for everything and anything. I am forever grateful to be surrounded by so much love – thank you.

# TABLE OF CONTENTS

<b>ACKNOWLEDGEMENTS</b>	<b>iv</b>
<b>LIST OF TABLES</b>	<b>viii</b>
<b>LIST OF FIGURES</b>	<b>ix</b>
<b>LIST OF SYMBOLS AND ABBREVIATIONS</b>	<b>xiv</b>
<b>SUMMARY</b>	<b>xv</b>
<b>CHAPTER 1. INTRODUCTION</b>	<b>1</b>
1.1 <i>C. elegans</i> as a model organism for aging	2
1.1.1 Gene expression and regulation in aging	3
1.1.2 Effects of stochasticity and variability on gene expression and aging	5
1.2 Methods to study gene expression in <i>C. elegans</i>	6
1.2.1 Population-level techniques to measure gene expression	7
1.2.2 Single animal-level techniques to measure gene expression	11
1.3 Thesis Objective	14
1.4 Thesis Outline	14
<b>CHAPTER 2. Engineering a microfluidic-based pipeline to quantify <i>in situ</i> gene expression in whole organisms using smFISH</b>	<b>16</b>
2.1 Introduction	16
2.2 Background	16
2.3 Materials and Methods	19
2.3.1 <i>C. elegans</i> strains and culture	19
2.3.2 Microfluidic device fabrication	20
2.3.3 Device operation	20
2.3.4 Single molecule fluorescent <i>in situ</i> hybridization	21
2.3.5 Imaging, image processing, and analysis	22
2.4 Results and Discussion	23
2.4.1 Experimental design of the microfluidic-based pipeline	23
2.4.2 Characterization of reagent delivery into individual animals	24
2.4.3 Adapting smFISH in whole organisms on chip	28
2.4.4 Coupling live imaging and smFISH within individual organisms	30
2.5 Conclusions	34
<b>CHAPTER 3. Designing microfluidic-based methods to achieve multiple cycles of smFISH with inter-individual resolution</b>	<b>36</b>
3.1 Introduction	36
3.2 Background	37
3.3 Materials and Methods	40
3.3.1 <i>C. elegans</i> strains, culture, and sample preparation	40
3.3.2 <i>E. coli</i> culture/rep and feeding assay	40

3.3.3	Device fabrication	41
3.3.4	Device operation	42
3.3.5	Imaging, image processing, and analysis	42
3.3.6	Multi-cycle smFISH	43
<b>3.4</b>	<b>Results and Discussion for the Electrokinetic/Microfluidic Hybrid Approach</b>	<b>45</b>
3.4.1	Design of electrokinetic/microfluidic hybrid device to enhance transport	45
3.4.2	Characterization of macromolecular transport through intact tissues	50
3.4.3	Demonstration of faster and multi-cycle smFISH with enhanced transport	52
<b>3.5</b>	<b>Results and Discussion for the Formamide-based Approach to Multi-cycle smFISH</b>	<b>56</b>
3.5.1	Validation of flow- and formamide-based stripping for multi-cycle smFISH	56
3.5.2	Experimental design to investigate the effects of an environmental perturbation on gene expression	60
3.5.3	Quantifying changes of gene expression resulting from different food level diets	62
<b>3.6</b>	<b>Conclusions</b>	<b>66</b>
 <b>CHAPTER 4. Microfluidic Approach to Correlate <i>C. elegans</i> Neuronal Functional Aging and Underlying CHanges of Gene Expression in Mechanosensation</b>		 <b>69</b>
<b>4.1</b>	<b>Introduction</b>	<b>69</b>
<b>4.2</b>	<b>Background</b>	<b>70</b>
<b>4.3</b>	<b>Materials and Methods</b>	<b>74</b>
4.3.1	<i>C. elegans</i> strains	74
4.3.2	<i>C. elegans</i> culture	75
4.3.3	Device design and fabrication	75
4.3.4	Computational deformation modelling	77
4.3.5	Device operation and imaging	77
4.3.6	Image processing and analysis	78
<b>4.4</b>	<b>Results and Discussion</b>	<b>79</b>
4.4.1	Integrated microfluidic pipeline to measure neuronal functional aging and gene expression	79
4.4.2	Computational modelling and empirical validation to measure neuronal health in different aged populations of <i>C. elegans</i>	82
4.4.3	Validating the microfluidic-based strategy to evaluate neuronal health	82
4.4.4	Age-related declines of neuronal function in a mechanosensory neuron	84
4.4.5	Age-related changes of gene expression in <i>mec-4</i> and <i>mec-10</i>	88
<b>4.5</b>	<b>Conclusions</b>	<b>91</b>
 <b>Conclusions and Future Directions</b>		 <b>93</b>
<b>4.6</b>	<b>Thesis Contributions</b>	<b>93</b>
<b>4.7</b>	<b>Future Directions</b>	<b>96</b>
4.7.1	Coupling behaviors and other phenotypic information with gene expression	96
4.7.2	Increasing gene-throughput and expanding spatial gene expression	98
4.7.3	Correlating function and gene expression on an individual level	99

<b>APPENDIX A. Chapter 2 Supplementary Materials</b>	<b>102</b>
<b>A.1 Raw Data for <i>Pdaf-7::Venus</i> and <i>gpa-3</i> expression</b>	<b>102</b>
<b>A.2 Supplemental Figures for Chapter 2</b>	<b>103</b>
<b>APPENDIX B. Chapter 3 Supplementary Materials</b>	<b>105</b>
<b>B.1 Supplementary Text for the Electrokinetic/Microfluidic Hybrid Device</b>	<b>105</b>
B.1.1 Estimating the enhancement of probe transport in the worm my electrokinetics	105
B.1.2 Estimating the enhancement of probe hybridization onto target mRNAs by probe enrichment	106
<b>B.2 Supplementary Figures for the Electrokinetic/Microfluidic Hybrid Device</b>	<b>108</b>
<b>B.3 Supplementary Figure for the Formamide-based Stripping Approach</b>	<b>109</b>
<b>B.4 Gene expression data for each individual animal</b>	<b>110</b>
<b>APPENDIX C. Chapter 4 Supplementary Materials</b>	<b>112</b>
<b>C.1 Supplementary Text for the Computational Deformation Modeling</b>	<b>112</b>
<b>C.2 Supplemental Figures for Chapter 4</b>	<b>114</b>
<b>REFERENCES</b>	<b>115</b>

## LIST OF TABLES

Table 1.1	Generalized comparison of pooled-sample and single-animal techniques	9
Table 4.1	Material properties used in the COMSOL model	77



## LIST OF FIGURES

- Figure 1.1 Conceptual model for gene expression quantification assays. In this example, we want to quantify the gene expression of (a) a population of *C. elegans* with different phenotypes indicated by the shading (white, grey, and black). To perform a pooled-sample assay, (b) the mRNA is extracted from the population of animals and (c) quantified. For single-animal assays, (d) gene expression can be measured within each animal with high spatial resolution. Each color represents a different mRNA sequence, and the numbers represent units of gene expression (A.U.) quantified. 7
- Figure 2.1 Schematic and overview of microfluidic-based pipeline. (a) Programmable syringe pump can consistently deliver multiple reagents over multiple cycles. (b) Microfluidic device has individual, trackable traps that can efficiently load animals and consistently deliver reagents. (c) Individual worms can be tracked over multiple steps to obtain multi-level gene expression information. Here *Pdaf-7::Venus* worms are imaged for *daf-7* expression and then smFISH is performed to quantify *gpa-3* mRNA counts. 23
- Figure 2.2 Multiple cycles of reagent delivery can be consistently delivered using the microfluidic platform. (a) Fluorescence intensity of the individual animal and the reference empty channel directly preceding the worm. Cycles of FITC-Dextran and non-fluorescent buffer are exchanged while tracking the same traps. (b) FITC-Dextran is accumulating in the fixed and permeabilized worms over prolonged exposure to the fluorescent macromolecules. 25
- Figure 2.3 The microfluidic-based platform enhances reagent exchange by introducing convection. (a) On-chip reagent exchange is flow-enhanced. Off-chip reagent exchange is slower as it is diffusion-dominated. (b) After 10 minutes of exposure to FITC-Dextran, worms on-chip were significantly brighter than worms incubated off-chip. (c) On-chip dynamics of FITC-Dextran accumulation is much faster and more consistent than (d) off-chip dynamics. Error bars represent standard deviation. An unpaired T-test was performed. (\* $P < 0.05$ ) 27

Figure 2.4	smFISH on whole animals using the microfluidic-based pipeline. (a) Representative maximum projection image of an individual animal after smFISH. Red puncta represent individual <i>gpa-3</i> mRNA molecules; DAPI staining for nuclei is in blue. Puncta are concentrated on the nerve ring of the animal. (b) Quantification of the puncta is consistent between on- and off-chip controls, repeated in 3 separate experiments. Each experiment was a different cohort of animals while each on- and off-chip comparison was from the same population. Error bars represent standard error mean. The Mann-Whitney U test was performed. (ns, not significant)	28
Figure 2.5	Multi-level gene expression quantification within individual animals. (a) Each point represents an individual animal with its <i>daf-7</i> and <i>gpa-3</i> expression, <i>Pdaf-7::Venus</i> fluorescence and <i>gpa-3</i> mRNA count respectively. $R = 0.39$ , indicating a low-to-moderate positive correlation. (b) Population binned by <i>gpa-3</i> expression reveals a positive relationship. Higher <i>gpa-3</i> expression leads to higher <i>daf-7</i> expression levels. Error bars represent standard error mean. The Mann-Whitney U test was performed. (** $P < 0.01$ ; * $P < 0.05$ )	31
Figure 2.6	The positive relationship between <i>gpa-3</i> and <i>daf-7</i> expression is consistent regardless of bin size. The binning is based on <i>gpa-3</i> mRNA expression quantified from smFISH. Higher <i>gpa-3</i> expression correlates with significantly higher <i>Pdaf-7::Venus</i> expression when the population is divided in (A) 2 bins or (B) 4 bins. The Mann-Whitney U test was performed. (** $P < 0.01$ ; * $P < 0.05$ )	33
Figure 3.1	Overview of device design. (a) Schematic of the microfluidic/electrokinetic hybrid device. (b) Micrograph of individually loaded worms in worm traps. White arrowheads indicate individually loaded adult worms. (c) Image of the device setup.	45
Figure 3.2	Device operation schematic. (a) Operating principle of probe delivery. (b) Fluorescent images of FITC-Dextran (model of smFISH probes) transport into individual worms before and after probe delivery process. The input reservoir received -150 V for 5 minutes. (c) Operating principle of probe removal. (d) Fluorescent images of FITC-Dextran transport out of individual worms before and after probe removal process. The input reservoir received +150 V for 7 minutes. The image settings (brightness and contrast) are consistent for all fluorescent images in (b) and (d).	46

Figure 3.3	Characterization of raw fluorescence intensity profiles of the worms. (a) before and after probe delivery and (b) before and after probe removal. The image settings (brightness and contrast) are consistent for all fluorescent images	47
Figure 3.4	Quantification of fluorescence intensity dynamics in individual worms during the probe delivery process. (a) -150 V was applied at the input reservoir. Arrows indicate when the ion enrichment zone started to establish for each worm. (b) Quantification of fluorescence intensity dynamics in individual worms during the probe removal process. +150 V was applied at the input reservoir. Arrows indicate when the ion depletion front passed through each worm. (c) Quantification of fluorescence intensity of individual worms at baseline and after probe delivery and removal. A one-way ANOVA and Tukey's multiple comparison tests were performed. (**P < 0.01, *P < 0.05; ns, not significant)	50
Figure 3.5	Fluorescent images of individual puncta, each corresponding to a <i>gpa-3</i> mRNA molecule in the neuronal cells. (a,b) On-chip probe delivery by the ICP-based ion pump in the same worm after (a) 4 hours and (b) 24 hours. (c,d) Off-chip diffusion-dominated delivery. (c) Individual puncta were not resolved after 4 hours of off-chip incubation. (d) Puncta are visible only after 24 hours of off-chip incubation. White arrows are added to aid puncta visualization. (e) Signal-to-noise ratio (SNR) of the puncta at each condition. The dotted line corresponds to the minimum value acceptable (SNR = 7). (f) Signal-to-background ratio of each punctum at each condition. An unpaired, two-tailed T test was performed. (**P < 0.01, *P < 0.05; ns, not significant)	52
Figure 3.6	Multi-cycle smFISH of <i>gpa-3</i> within the same worm using ICP-enhanced smFISH. (a) Individual puncta were resolved after initial hybridization. (b) After DNase I treatment for 4 hours, probes were dehybridized and removed by ICP-based ion pump. (c) The same puncta were resolved again after re-hybridization enhanced by ICP. Insets show magnified area at the vicinity of the target mRNA molecule.	54
Figure 3.7	Demonstration and validation of multicycle smFISH using two color imaging channels. (a) smFISH on-chip protocol was used to quantify <i>tph-1</i> in red and <i>daf-7</i> in cyan. (b) Formamide-based stripping successfully washed away bound probes. (c) Re-probing the same sample resulted in similar quality of smFISH as Round 1. (d) Number of puncta between the rounds and genes were not significantly different. A paired, two-tailed T test was performed. (e) Each point is an individual animal and its gene quantification from the 2 rounds. Dotted line indicates a perfect relationship. (f) Each point is an individual	56

animal and its expression for both genes. Images are maximum projections.

- Figure 3.8 Experimental design to study how diet influences gene expression. (a) 60  
The first round of smFISH will probe for *tph-1* and *daf-7*; the second round will probe for *tdc-1* and *cat-2*. (b) After exposing the animals to high or low food diet, we quantify these 4 genes per animal. (c) With this data, we can investigate how diet may influence gene-gene relationships as well as further analyses such as predicting the internal state of the animal based on its gene expression profile.
- Figure 3.9 Food levels influence gene expression profiles. Quantification of gene 62  
expression profiles of animals grown on low and high food conditions. The external stimuli (food), influences *tph-1* and *tdc-1* levels significantly. Unpaired, two-tailed T test was performed (\*\*\*P < 0.01).
- Figure 3.10 Quantifying gene-gene relationships across different food levels. 64  
Measuring 4 genes per animal allow us to measure 6 different gene-gene relationships: (a) *daf-7* and *tph-1*, (b) *daf-7* and *tdc-1*, (c) *daf-7* and *cat-2*, (d) *tdc-1* and *tph-1*, (e) *cat-2* and *tph-1*, and (f) *tdc-1* and *cat-2*. Each relationship has scaled axis. Each point represents a single animal and its expression levels.
- Figure 3.11 Heat map visualization of gene-gene relationships. Each square 65  
represents the value of the Pearson's Correlation (R) between two genes in each of the food conditions.
- Figure 4.1 Microfluidic-based approach to correlate age-related changes in gene 79  
expression and neuronal function. (a) Information from the environment is processed within the animal to elicit a response. (b) The DEG/ENaC channels are responsible for mechanosensation in *C. elegans* gentle touch neurons and have a transmembrane complex made of MEC-4 and MEC-10. (c) The populations are subsampled at different ages, and (d) the microfluidic pipeline enables measuring both gene expression and neuronal function to relate the age-related trends. (e) Imaging fluorescent gene reporters enables gene expression quantification with sub-cellular resolution. (f) Delivering precise, robust, high-frequency stimuli to differently aged animals enables measurement of neuronal function.

- Figure 4.2 Aging leads to a decline in neuronal function in mechanosensation. 84  
Each animal was loaded into the microfluidic chip, which applied stimulus pulses (8 gentle touch presses at ~2.5 Hz) for 3 seconds followed by a 40 second gap. This was repeated 9 times, followed by a longer 30 second stimulus also delivered at ~2.5 Hz. (a,b) The first and 9<sup>th</sup>, stimulus results enlarged. (c) First peaks from individual animals reveal there is a significant increase in neuronal response from Day 2 to 5, followed by a decrease. (d) 9<sup>th</sup> peaks from individual animals reveal no significant differences. The Kruskal-Wallis test was performed followed by Dunn's multiple comparison test (\*P<0.05, \*\*P<0.01).
- Figure 4.3 Age-related changes in dynamics of neuronal function. (a,b) Following 86  
the stimulus, there is a recovery period to baseline. To quantify the changes in dynamics, we fit a one-phase decay curve to the data for the (a) first and (b) 9<sup>th</sup> peaks.
- Figure 4.4 Aging leads to changes in gene expression patterns while regulation is 88  
well maintained. (a) Gene expression patterns across different ages reveals significant increases in MEC-4::mNeonGreen and MEC-10::mScarlet-I expression with age up to Day 10, followed by a decrease at Day 15. (b,c,d,e) With individual-level data, we could examine gene expressions within the same animal across different ages. There is a strong positive correlation between the two genes across the different ages, indicating that the regulation of the genes is well maintained regardless of age.

## LIST OF SYMBOLS AND ABBREVIATIONS

<i>C. elegans</i>	<i>Caenorhabditis elegans</i>
smFISH	Single molecule fluorescence <i>in situ</i> hybridization
<i>E. coli</i>	<i>Escherichia coli</i>
OP50	Strain of <i>E. coli</i> used for culturing <i>C. elegans</i>
C22	Small molecule used for progeny prevention in <i>C. elegans</i>
PDMS	Polydimethylsiloxane
(sc)RNA-seq	(single cell) RNA-sequencing
N2	Wildtype <i>C. elegans</i>
FITC	Fluorescein isothiocyanate
A.U.	Arbitrary Units
CEM	Cation exchange membrane
ICP	Isotachophoresis
TGF $\beta$	Transforming growth factor beta
GTNs	Gentle touch neurons

## SUMMARY

Aging is a complex, universal process that impacts us all differently. An increasingly important aspect of aging research is studying gene expression and regulation. Gene expression is age-, tissue-, and individual-dependent so it is important to capture all these pieces of information. While there are pooled-sample techniques that can measure the entire transcriptome (*e.g.*, RNA-sequencing), they fail to capture this gene expression data on an individual level. There are single-animal techniques to measure spatial gene expression and individual-to-individual variability, but these lack throughput (both sample- and gene-throughput) and are thus difficult to scale for larger studies.

In this thesis, I developed new microfluidic-based tools to address the limitations in single-animal assays to enable more robust gene expression studies in aging research. In **Chapter Two**, I engineered a pipeline that allows for single-animal gene expression quantification with sub-cellular resolution by adapting smFISH in adult *Caenorhabditis elegans* using microfluidics. In **Chapter Three**, I created two platforms to enable multiple cycles of smFISH, directly addressing the gene-throughput limitations. The first device is an electrokinetic/microfluidic hybrid device to enhance the reagent delivery of large, charged macromolecules. The second platform uses gentler reagents and allows for robust multicycle smFISH while retaining the tissue integrity of the samples. In **Chapter Four**, I correlated age-related changes in neuronal functional responses and the underlying gene expressions in the context of mechanosensation. The completion of this thesis creates an array of new tools that can improve the content of information we can gather on a single-animal level, enabling us to ask deeper questions in biology.

## CHAPTER 1. INTRODUCTION

Human life expectancy has doubled in the past 200 years due to vaccines, antibiotics, and improved sanitation practices.<sup>1</sup> The increase in lifespan has in turn brought a burden upon the older population, who now spend a larger proportion of their lives suffering from physical and cognitive aging-related declines. In the coming years, more and more people will suffer from the effects of aging-related disease, and by 2050, the number of people over 60 years old is estimated to double to 2.1 billion.<sup>1</sup> Aging is the single largest risk factor for chronic disease in humans,<sup>2,3</sup> and the most significant obstacle for improving healthcare outcomes for the elderly is our systemic lack of understanding aging.

To explain the aging process, there are many theories that fall under two main categories: (1) programmed and (2) damage or error theories. In the programmed theory, organisms follow a biological timeline where age-related declines are a natural progression.<sup>4,5</sup> One popular explanation is antagonistic pleiotropy where a gene's function has two opposite roles, such as a pro-fitness effect and a late-life detrimental effect. Depending on the exact definition, an example of this could be the gene *daf-2* in the nematode, *Caenorhabditis elegans* (*C. elegans*). This gene is essential to early life development, yet a loss-of-function mutation of this gene leads to a significant extension in lifespan.<sup>2,6</sup> In the damage or error category, theories emphasize environmental effects that induce cumulative damage. One key example is the damage/mutation accumulation theory where natural damage to essential elements of an organism, such as DNA, impact tissue function and lead to age-related declines.<sup>4</sup> Although certain theories of aging are



more compelling, neither of these categories fully explain the complete process, yet both of these theories are predicted to cause changes in gene expression with age.<sup>5</sup>

Since aging impacts specific tissues and individuals with variability,<sup>2</sup> it is necessary to study a comprehensive system. *C. elegans* are a popular model organism for aging studies due to their conserved molecular and genetic pathways and relatively short lifespans (~2-3 weeks).<sup>7</sup> This model has already demonstrated its usefulness in discovering aging pathways, such as the insulin/IGF-1-like signaling (IIS) pathway,<sup>2,6</sup> but there are key limitations to the methods available to handle these samples and perform larger-scale gene expression studies with individual- and tissue-level specificity.

In this thesis, I detail microfluidic-based tools to investigate gene expression and regulation with tissue-specificity during aging in *C. elegans*. Along with engineering new assays, this work aims to highlight new biological applications and demonstrate examples of answering deeper biological questions in aging research. The following sections serve as a brief review on prior literature and research on aging in *C. elegans*, with a focus on gene expression-based studies, and introduce the objectives of this work.

## **1.1 *C. elegans* as a model organism for aging**

In contrast to aging studies in humans and mammalian models, *C. elegans* have a relatively short natural lifespan (~2-3 weeks), are low-cost, and it is easy to culture large, isogenic populations. These powerful features of this organism make it a popular model for large-scale aging studies. In addition, this nematode also shares a significant amount of genetic homology to humans (~38% for protein-coding genes);<sup>7</sup> further, the first genes shown to modulate lifespan in any organism were found in *C. elegans*.<sup>2,3,6</sup> These genes

belong to the IIS pathway, whose role in aging is now known to be conserved among other animals including humans.<sup>3</sup> Other aging pathways (*e.g.*, TOR signaling and AMP kinase) found in the worm have also been extended to other organisms, suggesting aging-related genes are highly conserved.<sup>3</sup>

*C. elegans* are also an ideal model organism for monitoring gene expression due to their optical transparency. This key feature allows for fluorescence-based studies to be easily adapted to the animal. For example, many strains of *C. elegans* have been engineered to have fluorescent reporters of gene or protein expression, such as genetic transcriptional reporters. Other fluorescence-based staining techniques, such as single molecule fluorescence *in situ* hybridization (smFISH) and immunohistochemistry (IHC), have also been demonstrated in the organism, allowing relatively easy quantitative imaging of the whole animal. Further, the lineage and position of all 959 somatic cells, including the 302 neurons, have been mapped.<sup>3</sup> With the existing knowledge of the worm and its well-developed genetic toolkit, this is an ideal model for a gene expression-driven investigation of aging.

### 1.1.1 *Gene expression and regulation in aging*

Genetic factors are known to regulate and impact aging. Organisms adapt and respond to environmental sensory input, which influence their gene expression and regulation and lead to further implications on the aging process and overall lifespans. One of the most well-studied examples is the role of *daf-2* and the IIS pathway.<sup>6,8</sup> When *daf-2*, which encodes the insulin/IGF-1 receptor in *C. elegans*, has a loss-of-function mutation, the lifespan of the animal is more than doubled.<sup>6</sup> Animals grown in environments with less

food, such as in dietary restriction (DR) experiments, have decreased insulin/IGF-1 signaling.<sup>2,8</sup> This inhibited signaling leads to changes in gene expression through downstream transcription factors including DAF-16/FOXO, HSF-1, and SKN-1, which further upregulate or downregulate a diverse set of genes, significantly increasing lifespan.<sup>2</sup> These genetic pathways have a wide range of influences from proteostasis to protective stress responses to fertility, and they act together to impact the overall aging process.

Genes typically act in networks. For example, genes from the conserved TGF $\beta$  and serotonin pathways have dynamic interactions across tissues where one gene in the ASI neuron (*daf-7*) regulates the gene-expression variability, and the other in the ADF and NSM neurons (*tph-1*) regulates the dynamic range of the gene-expression responses.<sup>9</sup> Gene interaction networks are also context dependent. For instance, investigations in *C. elegans* have discovered that a food-sensing gene (*daf-7*) is typically expressed in one pair of neurons; however, when presented with pathogenic bacteria, its expression location shifts to other neurons.<sup>10</sup> Another approach to study gene regulation, in the context of aging, is measuring co-expression relationships. The assumption is that certain genes within the same family or class have similar changes of gene expression with age (*e.g.*, *sod-1* and *sod-2* should increase and decrease in expression similarly since they play similar roles).<sup>11</sup> By measuring the variability of the relationship with age, described as transcriptional drift, this can be a metric of aging health (*e.g.*, perhaps an anti-aging drug decreases the transcriptional drift, thus slows aging).<sup>11</sup>

### 1.1.2 Effects of stochasticity and variability on gene expression and aging

Gene expression is a fundamentally stochastic process. The inherent noise in transcription and translation lead to cell-to-cell and organism-to-organism variations in levels of mRNA and protein expressions.<sup>12,13</sup> As a canonical example, Elowitz *et al.* (2002)<sup>12</sup> introduced two copies of the same promoter, one driving the expression cyan fluorescent protein and the other driving the expression of yellow fluorescent protein, into *E. coli*. Although the bacteria were isogenic, the population still had a wide spectrum of colors due to the stochasticity of gene expression and the variability between individuals. In their analysis, they were able to identify the sources of noise as two categories: extrinsic and intrinsic. Extrinsic noise refers to elements related to the environment, such as the amount of food available, that influence gene expression; these tend to have more global effects. Intrinsic noise is the inherent stochasticity associated with transcription and translation, such as the diffusion and Brownian motion required for molecular interactions.<sup>12,13</sup>

On an organism-level, stochasticity has major impacts on aging. For example, even in isogenic populations and controlled laboratory conditions, individuals live to different ages.<sup>11,14-16</sup> These differences can also be attributed to extrinsic and intrinsic sources of noise. Extrinsically, animals may be experiencing slightly different local environments, such as the amount of food or pheromones present, which can thus alter gene expression/regulation and lifespan.<sup>8,9,14,17</sup> Intrinsically, there will be variability in gene expressions between animals due to randomness. These sources of stochasticity can all influence the lifespan of the organism. For example, variable expression profiles of certain

genes, such as for some microRNAs, have been identified as early-life predictors of longevity.<sup>15</sup>

In the aging field, the stochasticity of gene expression has been an increasingly interesting point of discussion. It has been generally accepted that the stochasticity or variability in gene expression, between organisms and within tissues, increases with age across multiple models, which contribute to age-related declines and dysregulations.<sup>18-21</sup> However, a study in yeast has shown that there is actually a decrease in variability with age, which is followed by a period of increased variability and noise towards the end of the lifespan.<sup>22</sup> With these somewhat conflicting reports, there is a need to further understand how the variability in gene expression, perhaps in an essential regulatory pathway, may influence the overall aging process. Current methods are limited in either inherent practicality (*e.g.*, losing inter-individuality in single cell RNA-sequencing) or throughput (*e.g.*, imaging individual fluorescent transcriptional reporter animals) to measure gene expression variability within a population. Consequently, there are limited studies that comprehensively measure this gene expression variability, especially in the context of aging. There are hypotheses that the age-related increase in stochasticity and variability contributes to dysregulation and the overall decline of the organism;<sup>18-22</sup> however, it is difficult to definitively test these ideas due to the lack of tools available.

## **1.2 Methods to study gene expression in *C. elegans***

Gene expression and regulation play diverse and important roles ranging across defining phenotypic traits and heredity to the cause of stochastic emergent behaviors. By quantifying the expression, whether in a sample of single cells, a specific tissue, or in a

whole animal, one can gain insights into the underlying biology. Many biological questions now require single-animal and tissue-specific resolution, such as why individuals, even within an isogenic population, have variations in development and aging across different tissues and organs. The popular techniques that quantify the transcriptome (*e.g.*, RNA-sequencing) process populations of animals and cells together and thus, have limitations in both individual and spatial resolution. There are single-animal assays available (*e.g.*, fluorescent reporters); however, they suffer other technical bottlenecks, such as a lack of robust sample-handling methods. Microfluidic technologies have demonstrated various improvements throughout the years, and it is likely they can enhance the impact of these single-animal gene expression-based assays.<sup>23</sup>

### 1.2.1 Population-level techniques to measure gene expression

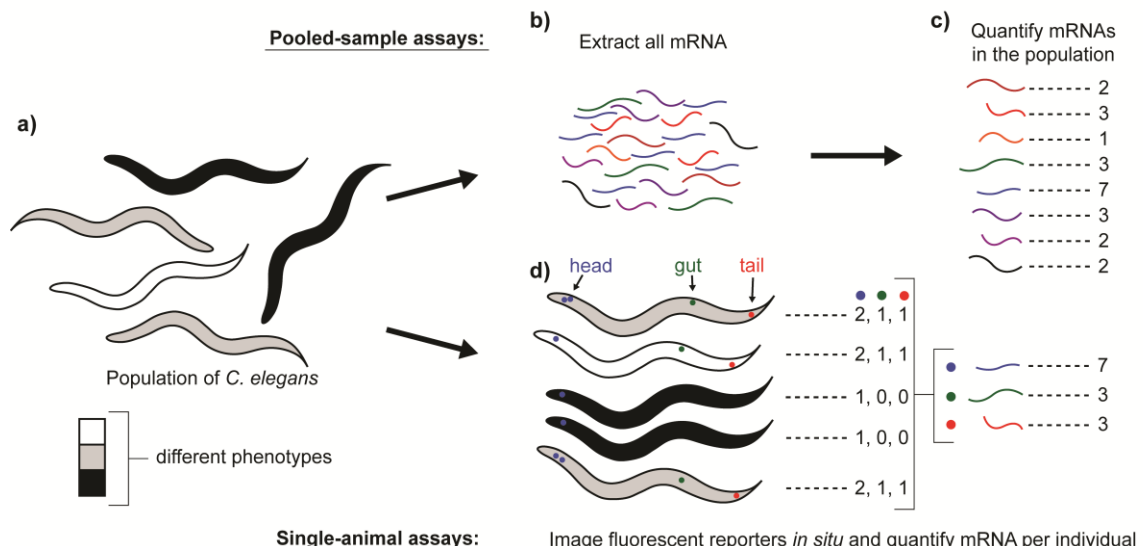


**Figure 1.1 Conceptual model for gene expression quantification assays.** In this example, we want to quantify the gene expression of (a) a population of *C. elegans* with different phenotypes indicated by the shading (white, grey, and black). To perform a pooled-sample assay, (b) the mRNA is extracted from the population of animals and (c) quantified. For single-animal assays, (d) gene expression can be measured within each animal with high spatial resolution. Each color represents a different mRNA sequence, and the numbers represent units of gene expression (A.U.) quantified.

Pooled-sample techniques that measure gene expression include cDNA microarrays, RNA-seq, and single cell RNA-seq (scRNA-seq), which have been reviewed in depth<sup>24-27</sup> (Fig. 1.1, Table 1). Although each of these tools work differently, the overall pipeline and results are similar (Fig. 1.1). Briefly, the total mRNA is extracted from the sample (Fig. 1.1b), and through different mechanisms, the mRNA is quantified (Fig. 1.1c). cDNA microarrays were one of the first methods to study gene expression on a transcriptome level. With these first investigations in model organisms, such as in flies<sup>28,29</sup> and worms<sup>30</sup>, we began to understand how the gene expression networks and patterns can change due to perturbations, such as aging or genetic mutations. The next major advancement in assays was RNA-seq. Rather than profiling predefined transcripts and genes via hybridization in microarrays, RNA-seq can fully sequence and quantify each mRNA species of the sample. Although these tools can measure the entire transcriptome, the mRNA extraction and processing require the entire population of samples to be pooled together.<sup>26,27</sup> This loses inter-individuality (*i.e.*, we do not know which cell or animal the transcripts are being measured); further, while cellular identity could be inferred for cells with characteristic expression profiles, inferring other complex cell identities are not precise and thus, the spatial information of gene expression is not precise. Together, while these key methods give a rough indication of which genes are important to a particular process, spatial, temporal, and inter-relational details may be missing. This lack of information can prevent deeper insights into the biological processes.

In order to localize gene expression to specific tissues, these methods have been performed on dissected organs or body parts,<sup>28,31,32</sup> which require expertise and intensive manual labor. While these studies can quantify gene expression in each tissue, they cannot

preserve any individuality. The samples are still pooled together; the information quantified is averaged over the population, and importantly, they still lack cellular specificity. To retain inter-individuality, RNA-seq has been adapted to single worms; however, the tissue- and cellular-specificity are still lost.<sup>33</sup>

**Table 1.1. Generalized comparison of pooled-sample and single-animal techniques**

	Technique	Single animal	Spatial resolution	Gene throughput	Ease-of-use	Other notes
Pooled-sample Techniques	cDNA Microarray <sup>26,27,30</sup>	No	Whole animal to dissected body parts	Transcriptome level	Complex manual handling	Profiles pre-defined transcripts
	RNA-seq <sup>24,26,34</sup>	No*	Whole animal to dissected body parts	Transcriptome level	Complex manual handling	*RNA-seq has been adapted to single worms <sup>33</sup>
	scRNA-seq <sup>24,35-37</sup>	No	Inferred/predicted cells	Transcriptome level	Complex manual handling	Requires large populations (~1,000 to 10,000 animals)
Single-animal Techniques	Fluorescent Transcriptional Reporter <sup>38-40</sup>	Yes	Cell to subcellular	Typically, 2-3 genes	Strain engineering and manual handling	Gene throughput limited by number of resolvable fluorophores
	smFISH <sup>41-43</sup>	Yes	Subcellular	Typically, 2-3 genes	Probe design and manual handling	Gene throughput can be increased with alternative strategies, <sup>44,45</sup> but these have not been achieved in whole animals

One strategy to overcome this and measure gene expression with high spatial resolution is to capture the transcripts *in situ* and then perform sequencing *ex situ*.<sup>46</sup> This type of approach was first introduced as “spatial transcriptomics” and demonstrated on thin tissue slices.<sup>47</sup> Briefly, fixed tissue samples are annealed onto glass slides that have barcoded reverse transcriptase primers in a known pattern. The transcripts are sequenced



and, since the location of each different bar code is known, computational reconstruction can reveal the spatial distribution of the transcripts. Recently, there have been advances to the technique, such as Slide-seq.<sup>48</sup> Here, the barcodes are attached to 10  $\mu\text{m}$  beads rather than printed on a glass slide. While this type of approach can measure genome-wide expression at high spatial resolution, this has only been demonstrated on thin tissue slices ( $\sim 10 \mu\text{m}$  thick); it may be difficult to scale to whole animals, and certainly not at population levels.

Perhaps the most advanced assay currently available to measure gene expression is scRNA-seq.<sup>49</sup> Briefly, the cells of the sample, such as a population of animals, are isolated and individually sequenced. While this can reveal very high-detailed information, there are some notable caveats. Along with the need for large population sizes ( $\sim 1,000$ s to  $\sim 10,000$ s of animals)<sup>35,50</sup> and lack of individual-level quantification, scRNA-seq can only infer each cell's identity based on its expression profile.<sup>37</sup> For example, there may be a panel of known neuronally expressed genes for a particular animal; cells that have higher expression of these genes will thus more likely be from a neuron. To be accurate, these methods rely on existing spatial expression data for an array of panel genes.<sup>51</sup> While larger tissues or cells with well-defined transcriptomes may have accurate predictions, smaller tissues or more ambiguous cells may be incorrectly labelled. This level of noise is perhaps further amplified as scRNA-seq is unable to reliably measure or detect transcripts in low abundance. In addition, the sample processing steps are nontrivial and lose many of the cells, or worse, cell types.<sup>35,37</sup> These technical limitations can complicate data analysis and overlook more subtle details of gene expression, such as the natural biological variation in the system.

While scRNA-seq computational predictions have significantly improved,<sup>51,52</sup> their inferences for cell identification still require validation.<sup>53</sup> There have been improvements in these various pooled-sample techniques, but even the most advanced technologies lack either the ability to quantify gene expression on an individual level or to have true spatial localization. Although this may not be an issue for unicellular models, such as performing scRNA-seq in yeast,<sup>22</sup> it cannot be applied to multi-cellular organisms.

### 1.2.2 *Single animal-level techniques to measure gene expression*

To measure finer details, there are high resolution single-animal techniques such as fluorescent transcriptional reporters<sup>40</sup> and smFISH<sup>42</sup> (Fig. 1.1d, Table 1). These methods allow researchers to use fluorescent microscopy to visualize and quantify gene expression with tissue specificity (Fig. 1.1d). In addition, single-animal resolution enables us to find if there are any correlations between the phenotypes of the animals and their unique gene expression profiles. This would enable us to ask questions, such as how the phenotypic variability is influenced by the gene expression variability. It may be that, among the population of animals, differences in local environments contribute to variability in gene expression and behavior (Fig. 1.1a,d). For example, *daf-7* is a gene that is typically only expressed in one pair of neurons in *C. elegans*; however, when the animals are exposed to pathogenic bacteria, *daf-7* expression occurs in different neurons, and the animals display an avoidance behavior.<sup>10</sup> There are other assays to measure expression on a single-animal or single-cell level such as the cell-based MS2-MCP system,<sup>41,54-56</sup> immunohistochemistry to quantify protein expression, and newer, emerging technologies such as CRISPR-dCas13a<sup>57</sup> to measure mRNA *in vivo*. In this work, we chose to focus on these two more popular and commonly used methods in model organisms: fluorescent transcriptional

reporters and smFISH. These approaches can be complimentary, and their quantifications are based on fluorescent microscopy.

Fluorescent transcriptional reporters allow us to measure gene expression activity in live animals with tissue specificity. Here, a fluorophore, such as GFP, is driven by the promoter fragment of the gene of interest. The genetically modified animal will express the fluorophore; by measuring the fluorescence intensity, we can determine the promoter's activity as well as where it drives expression in the animal.<sup>39,40,58</sup> There are variations to this approach such as translational fusion reporters where the fluorophore is directly fused to the protein of interest; this can provide a better measurement on protein expression rather than the transcriptional activity.<sup>40</sup> Further, for transparent transcriptional reporter systems, such as cells,<sup>59</sup> yeast,<sup>38</sup> and *C. elegans*<sup>40</sup>, imaging can be done *in vivo* without much perturbation to the samples, allowing for researchers to track the expression levels in individual samples over time. However, it is important to note that the long half-life of fluorophores (~24 hours)<sup>39,60,61</sup> can limit studies dependent on measuring dynamic phenotypes and require higher temporal resolution. To reflect meaningful promoter activity and detect the subtleties of gene expression, it may be necessary to have the fluorescent transcriptional reporters as single copy integrants.<sup>62</sup> Having a single copy ensures that the amount of fluorescence intensity accurately represents the promoter activity. Integrating the exogenous transgene into the genome prevents mosaicism (*i.e.*, integration ensures all cells in the sample have copies of the promoter-driven fluorophore transgene). The major drawback for this method is that it can be difficult and time-consuming to create new strains, which is often the bottleneck for large-scale studies on many genes.

Another single-animal technique to measure *in situ* gene expression is smFISH. In this approach, gene-specific, fluorescently labelled probes are delivered into a fixed and permeabilized sample. In contrast to fluorescent transcriptional reporters, this method does not require any genetic manipulations. This makes smFISH particularly attractive for many genomic-based studies that require non-transgenic animals (*e.g.*, studying wildtype animals, genome-wide association studies, etc.). In smFISH, a gene-specific probe set consists of 20-40 fluorescently labelled short nucleic acids (each ~25 nts); each individual probe within the set has a different sequence that binds specifically to the target mRNA. To ensure specificity and prevent false-positive signals from non-specific binding, a fluorescent punctum only becomes resolvable when 20-30 probes hybridize onto the same mRNA molecule due to the high local concentration of the probes.<sup>41,42</sup> This approach allows us to visualize and measure individual mRNA molecules within the fixed sample with sub-cellular spatial resolution. Along with quantifying the amount of gene expression, its use in model organisms is often to localize gene expression and evaluate spatial organization.<sup>10,63,64</sup> Despite its advantages, there are also several drawbacks to this method. Along with long incubation times (*i.e.*, many hours to days) for different reagents, durations, and temperatures, it requires sample fixation and permeabilization, typically limiting its use to an endpoint assay.

While both single-animal techniques offer much more detailed information and allow us to study more subtle details of gene expression, they lack gene- and sample-throughput. These techniques are based on fluorescent microscopy; this limits the number of genes studied per animal to the number of spectrally resolvable fluorophores on an imaging setup (typically 2-3). Another shortcoming is that these methods require slow, manual handling

and imaging of each sample. Increasingly, transcriptome-level studies using pooled-sample techniques are inspiring questions in biology that depend on single-animal resolution. These shortcomings to these methods have not yet been completely addressed, and thus present engineering opportunities.<sup>23</sup>

### 1.3 Thesis Objective

There is a systemic lack of our understanding of aging. To improve healthcare outcomes for our increasingly aging population, we need better tools to study the aging process. Investigations using *C. elegans* have demonstrated the significant roles of gene regulation and expression; however, the current reagents and techniques available fail to efficiently quantify gene expression with high detail. Pooled-sample techniques (*e.g.*, RNA-seq) are able to quantify the entire transcriptome, but importantly, they fail to capture individual- and tissue-level data. Fluorescent transcriptional reporters and smFISH allow researchers to study gene expression with these details. However, traditional approaches using these reagents are low throughput (time consuming, manually intensive, and low number of genes studied). The purpose of this thesis is to address these limitations found in single-animal approaches by engineering new microfluidic-based tools. By resolving these shortcomings, this work aims to demonstrate and provide a framework for future studies to improve the content of information we can gather on a single-animal level.

### 1.4 Thesis Outline

The content of this thesis is divided into five chapters. **Chapter Two** presents a microfluidic-based pipeline to quantify *in situ* gene expression in whole organisms using smFISH. This work aims to directly address the need for multiple manual reagent

exchanges in smFISH as well as its limitation as typically a single timepoint assay. By creating a microfluidic-based pipeline to deliver reagents while retaining the individual identities of each animal, I can couple live-imaging information with gene expression quantification from smFISH. **Chapter Three** builds upon this work by further enabling multiple cycles smFISH to address the gene-throughput limitation. The number of genes quantified in smFISH is limited to the number of resolvable fluorophores of an imaging setup (typically 2-3 genes). To resolve this shortcoming, I engineered two approaches to strip and re-probe the same biological samples, enabling us to perform multiple rounds of smFISH. **Chapter Four** delivers a microfluidic strategy to correlate underlying changes of neuronal gene expression with neuronal functional aging in the mechanosensory pathway. While measuring age-related changes of gene expression can be useful, correlating this information with functional imaging serves as a more powerful tool to possibly uncover or further support different aging mechanisms. **Chapter Five** is a summary of the thesis contributions as well as a discussion of possible future work.

## **CHAPTER 2.     ENGINEERING A MICROFLUIDIC-BASED PIPELINE TO QUANTIFY *IN SITU* GENE EXPRESSION IN WHOLE ORGANISMS USING SMFISH**

This chapter is adapted from “smFISH in chips: a microfluidic-based pipeline to quantify *in situ* gene expression in whole organisms” published in 2020 in *Lab on a Chip*.<sup>65</sup>

### **2.1    Introduction**

In this chapter, I describe the development and optimization of a microfluidic-based pipeline that enables efficient reagent exchanges necessary for biological assays, such as smFISH, and the ability to track individual animals. By automating a robust microfluidic reagent exchange strategy, I adapted and validated smFISH on chip and combined this technology with live imaging of a fluorescent transcriptional reporter. Together, this multi-level information enabled us to quantify a gene expression relationship with single-animal resolution. While this microfluidic-based pipeline is optimized for live-imaging and smFISH *C. elegans* studies, the strategy is highly adaptable to other biological models as well as combining other types of live and end-point biological assays, such as behavior-based toxicology screening and immunohistochemistry.

### **2.2    Background**

With techniques such as fluorescent transcriptional reporters and smFISH, imaging and studying gene expression within individuals has become much more accessible. Fluorescent transcriptional reporters are often used in small model organisms to quantify

protein expression with tissue-specificity. Here, animals are genetically modified to express a fluorescent marker under the same regulatory control of a gene of interest; typically, the promoter region of the gene is used to drive the expression of a fluorescent protein.<sup>40</sup> Although not an exact measurement of the target protein, live imaging of these animal strains can reveal the relative expression levels and patterns with tissue-specificity. Further, for transparent organisms such as *C. elegans*, imaging can be done in live animals, and thus the experiments can be coupled with other manipulations, such as environmental perturbations or longer time-scale studies (*e.g.*, aging). To reflect meaningful promoter activity and measure the subtleties of gene expression, transcriptional reporters are preferred to be single copy integrants. One drawback for this technique is that creating new reporter strains is difficult, time-consuming, and can often be a bottleneck for large-scale studies on many genes or genetic networks simultaneously. Another disadvantage is the typical long half-life of fluorophores (~24 hours),<sup>60,61</sup> which can limit the temporal resolution of studies with dynamic phenotypes.

An orthogonal approach to study gene expression *in situ* within a whole organism, at the single-organism level, is smFISH. In this process, gene-specific, fluorescently labeled probes are delivered into a formaldehyde-fixed and ethanol-permeabilized sample, and these probes hybridize to the target mRNA molecules. Each probe set consists of ~20-40 fluorescently labeled short nucleic acids with different sequences that bind specifically to the target mRNA. A fluorescent punctum only becomes resolvable when ~20-30 probes hybridize to the same mRNA molecule; this strategy ensures specificity, and the sequence-specific probes prevent false-positive signals from non-specific binding.<sup>42,66</sup> Through fluorescent microscopy, we are able to image these hybridized probes as individual puncta,



corresponding to individual target mRNA molecules, which enables us to quantify and localize a specific gene's expression with sub-cellular spatial resolution. In contrast to transcriptional reporters, smFISH directly investigates mRNA expression, which is innately different than protein expression to infer promoter activity. An advantage of the technique over transgenic approaches, such as transcriptional reporters, is that smFISH can be performed on native samples without genetic modification, and thus is more generalizable. Using new smFISH multiplexing and barcoding techniques, some have been able to characterize gene expression on a transcriptome-level in mounted cells and thin tissue slices.<sup>43,44</sup> However, these multiplexing techniques have not been achieved in whole animals, perhaps due to a combination of transport and sample-mounting challenges further discussed in **Chapter 3**. In addition, for subcellular features such as the axonal process or synapse of a neuron, localization of the smFISH puncta can be difficult; here, fluorescent transcriptional reporters are more appropriate as these smaller features are easily resolvable in live animals. Along with long incubation times (*i.e.*, days) and multiple manual reagent exchanges, which makes keeping inter-individual identities extremely challenging in large populations, a major limitation of smFISH is its need for fixed samples; thus, smFISH can only be used as an endpoint assay.

Live imaging of transcriptional reporters provides a real-time, relative gene expression readout, while smFISH can efficiently profile a snapshot of the animal's true mRNA expression but only at an endpoint. To study complex gene networks in multiple tissues with high spatial resolution in many individuals, we present a platform that combines the advantages of live-imaging and smFISH in the same animals. In this work, I engineered a microfluidic-based pipeline to capture large populations of *C. elegans* in

individual, trackable traps and investigate multi-level gene expression (*i.e.*, protein and mRNA) (Fig. 2.1). Using this microfluidic platform, I can robustly load and isolate individual animals and effectively deliver different reagents over multiple cycles; the ability to track an individual over multiple steps allows us to relate multiple gene expressions and uncover their relationship. We automated and characterized the on-chip reagent exchange, validating that the smFISH process and reagent transport with our on-chip method is more robust and much faster than the off-chip approach. Current methods to study gene expression relationships rely on multiple strains of animals with knockout or gain-of-function mutations to examine how these influence each other. Here, I use our microfluidic platform to image a transcriptional reporter and then perform smFISH for another gene on the same population of animals while tracking individuality. By relating their expressions as single animals, it enabled us to discover a relationship between these genes in a single genetic background. Furthermore, this platform is highly adaptable to study other genes as well as introduce multiplexed approaches by using spectrally distinct smFISH probes for multiple genes.

## **2.3 Materials and Methods**

### **2.3.1 *C. elegans strains and culture***

The *C. elegans* strains used in this work were N2 strain (QLN2) and *Pdaf-7::Venus* strain (QL89). The *daf-7* reporter, QL89, was previously constructed and validated (*drcSI7[pdaf-7::Venus:unc-119] II; unc-119(ed3) III*).<sup>9</sup> The N2 strain (wildtype) was used in the pipeline characterization and smFISH validation. The *daf-7* reporter was used for all experiments with live imaging. All worms were grown following standard protocols on

NGM agar plates with *Escherichia coli* (*E. coli*) OP50 lawns and maintained at 20 °C. For all studies in this Chapter, hermaphrodite worms were synchronized to Day 1 adults.

### 2.3.2 *Microfluidic device fabrication*

Microfluidic device fabrication has been previously described.<sup>67</sup> Briefly, the master mold of the microfluidic device was fabricated with SU-8 2050 (Microchem), a negative photoresist, by UV photolithography. The microfluidic devices were fabricated in polydimethylsiloxane (PDMS, Dow Corning Sylgard 184) by traditional soft lithography. Prior to the micromolding process, the surfaces of the master mold wafers were treated with tridecafluoro-1,1,2,2-tetrahydrooctyl-1-trichlorosilane vapor (Sigma-Aldrich). A uniform layer of PDMS (10:1 ratio) was added on the master mold to a height of ~5 mm. The PDMS was cured at 70 °C overnight (~16 hours) and peeled off. We found that the exact ratio between PDMS components (*i.e.*, 10:1 rather than a higher ratio like 15:1) and the long curing time is crucial to prevent the device from swelling during the overnight ethanol incubation step in the smFISH process. Devices were cut into shapes, two holes (one inlet and one outlet) were punched with 19-gauge needles (McMaster-Carr) per device, and each device was bonded to a cover glass by plasma bonding.

### 2.3.3 *Device operation*

For each experiment, the microfluidic device was first filled with S Basal solution to remove air bubbles. The worms cultured on NGM agar plates were washed off using S Basal solution and transferred into a 15 mL tube. After allowing the animals to settle to the bottom of the tube, the supernatant was removed. Animals were loaded into a syringe and delivered into the device manually using a flow rate of ~3 mL/hr for 1 minute, as described

in the previous literature.<sup>65,67</sup> After the animals were loaded into the microfluidic device, reagents were delivered using a programmable syringe pump. For device characterization, we flowed alternating cycles of fluorescein isothiocyanate (FITC)-Dextran at 150  $\mu\text{L}/\text{min}$ . For all smFISH experiments, we flowed in the new reagent at 15  $\mu\text{L}/\text{min}$  for 3 mins then 10  $\mu\text{L}/\text{hr}$  for the various incubation times necessary. These reagents can be found below.

#### 2.3.4 *Single molecule fluorescent in situ hybridization*

Probe design and the protocol to perform smFISH in *C. elegans* have been previously described.<sup>42</sup> In this study, we ordered custom Stellaris smFISH probes for targeting *gpa-3* labeled with Cal Fluor Red 610. For each reagent exchange done off-chip, animals were gently spun for 10 s using a tabletop centrifuge, the supernatant was removed, and the new reagent was added. For each exchange done on-chip, we flowed in the new reagent at 15  $\mu\text{L}/\text{min}$  for 3 mins then 10  $\mu\text{L}/\text{hr}$  for the various incubation times necessary.

All reagents for on- and off-chip experiments were the same. For all N2 experiments, animals were fixed off chip; for all *Pdaf-7::Venus* (QL89) experiments, animals were fixed on chip. For fixation, animals were exposed to 3.7% formaldehyde for 45 minutes. After, they were washed and incubated in 70% ethanol to permeabilize overnight at 4 °C. For smFISH probe hybridization, animals were washed in wash buffer (10% formamide, 2X SSC, in nuclease-free water) for 5 minutes. Next, they were incubated in a solution of the custom probes (1.25  $\mu\text{M}$ ) in hybridization buffer (1 g dextran sulfate, 40  $\mu\text{L}$  RNase-free BSA (50 mg/mL), 10% formamide, 9 mL nuclease-free water) at 30 °C overnight. Samples were washed with wash buffer for 30 mins then DAPI stain (5 ng/mL) for 30 mins. Prior to imaging, animals were washed with or suspended in GLOX antifade solution.

### 2.3.5 Imaging, image processing, and analysis

For device characterization we used FITC-Dextran (1 mg/mL) in S-Basal. The molecular transport was recorded with whole field illumination on a fluorescence dissecting scope (Leica, MZ16F). We quantified the dynamics and intensities using a custom MATLAB code. The plots and statistics were created and performed using GraphPad Prism and MATLAB.

For all other imaging experiments, we used a spinning disk confocal microscope (PerkinElmer UltraVIEW VoX) equipped with a Hamamatsu FLASH 4 sCMOS camera and a 60x oil immersion objective. All smFISH images were analyzed using a standard software, FISH-quant,<sup>68</sup> to identify and count the puncta. In order to have accurate comparisons between the on- and off-chip results, we matched our sample size for each experiment. For the experiments using the *Pdaf-7::Venus* strain, animals were loaded into the device and washed with 50 mM tetramisole for immobilization. Animals were immediately fixed for smFISH after live imaging. To quantify the *daf-7* expression, we used a custom MATLAB code to draw an ROI that encompasses the two ASI cell bodies in a maximum projection and quantifies the average fluorescence intensity after average background subtraction. In order to have consistent quantification, we only included worms with the correct orientation where the ASI neurons did not overlap. The plots and statistics were created and performed using GraphPad Prism and MATLAB.

## 2.4 Results and Discussion

### 2.4.1 Experimental design of the microfluidic-based pipeline

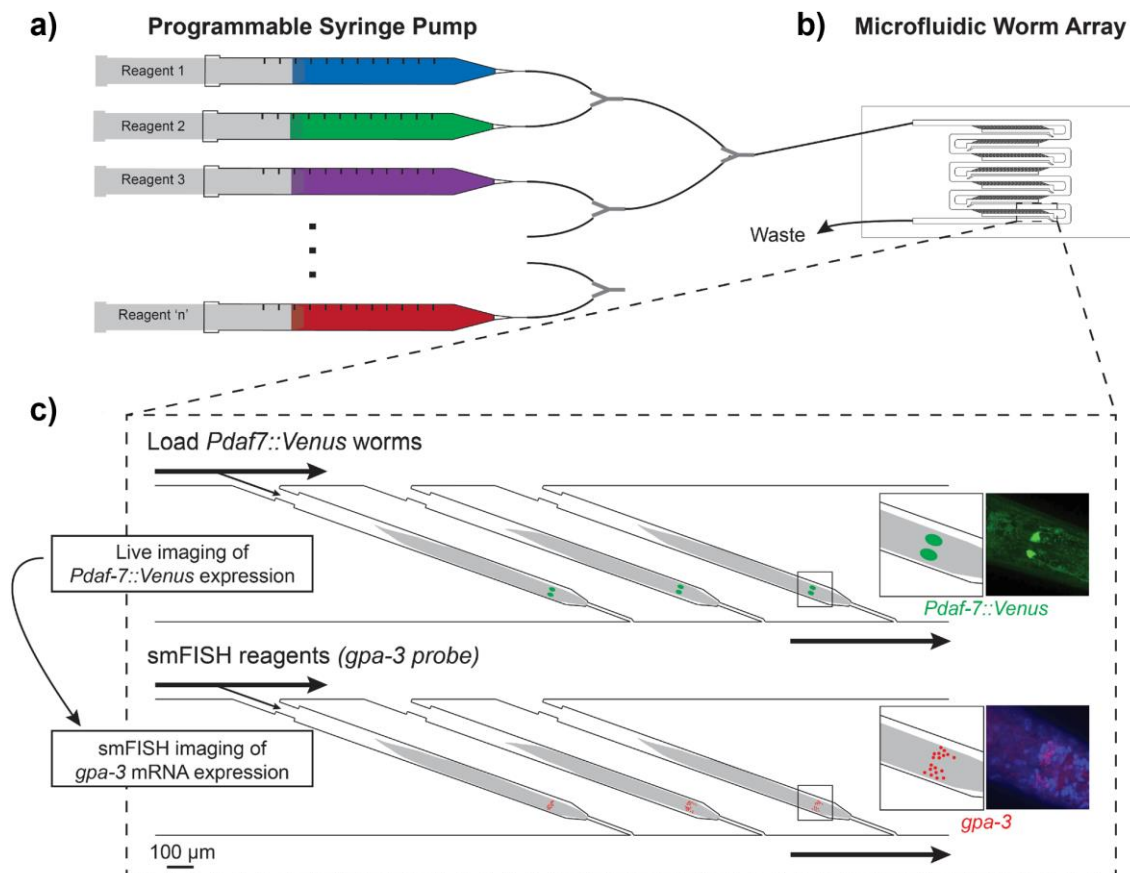


**Figure 2.1 Schematic and overview of microfluidic-based pipeline.** (a) Programmable syringe pump can consistently deliver multiple reagents over multiple cycles. (b) Microfluidic device has individual, trackable traps that can efficiently load animals and consistently deliver reagents. (c) Individual worms can be tracked over multiple steps to obtain multi-level gene expression information. Here *Pdaf-7::Venus* worms are imaged for *daf-7* expression and then smFISH is performed to quantify *gpa-3* mRNA counts.

To collect multi-level gene expression information from the same worm in a large population of worms, I developed a pipeline based on a microfluidic array device<sup>67</sup>; this protocol loads animals individually into separate traps and delivers reagents driven by a programmable syringe pump (Fig. 2.1a,b). By retaining inter-individuality, this platform enables us to study multiple pieces of information from single worms. Here, I first

completed live imaging of *Pdaf-7::Venus* animals to measure *daf-7* gene expression as an example of a live phenotype. The same worms are then fixed and permeabilized, and I performed smFISH to measure *gpa-3* expression (Fig. 2.1c). This experiment requires many complex reagent exchanges, which would have been difficult if not impossible to perform on the laboratory-scale with conventional tools: (1) live animals needed to be immobilized in tetramisole for *in vivo* fluorescence microscopy, (2) after *in vivo* imaging, animals must be quickly fixed in formaldehyde to ensure preservation of the transcriptional states in each cell, (3) animals were permeabilized in ethanol overnight, (4) animals were washed in wash buffer, (5) smFISH probes were delivered overnight, (6) excess probes were washed with wash buffer, (7) DAPI stain was added, and (8) anti-fade solution was delivered for smFISH imaging. Each step adds more complexity, which makes tracking an individual animal off-chip more challenging. With our pipeline, we could obtain this rich, individual-level dataset to study the relationship between the two genes; in this Chapter, we investigated the relationship between *daf-7* and *gpa-3*. Further, this approach is generalizable to multiple live reporters and smFISH probes as well as other microfluidic array-based platforms.

#### 2.4.2 Characterization of reagent delivery into individual animals

Along with many other end-point assays, smFISH requires multiple reagent exchange steps. Since there is natural variability between even isogenic animals, consistent reagent delivery across different animals is essential to minimize experimental noise and have accurate quantification of gene expression. Thus, it was important for us to characterize the device and its reagent transport. As a model for the smFISH fluorescent probes, I used fluorescein isothiocyanate (FITC)-Dextran. This reagent has a similar

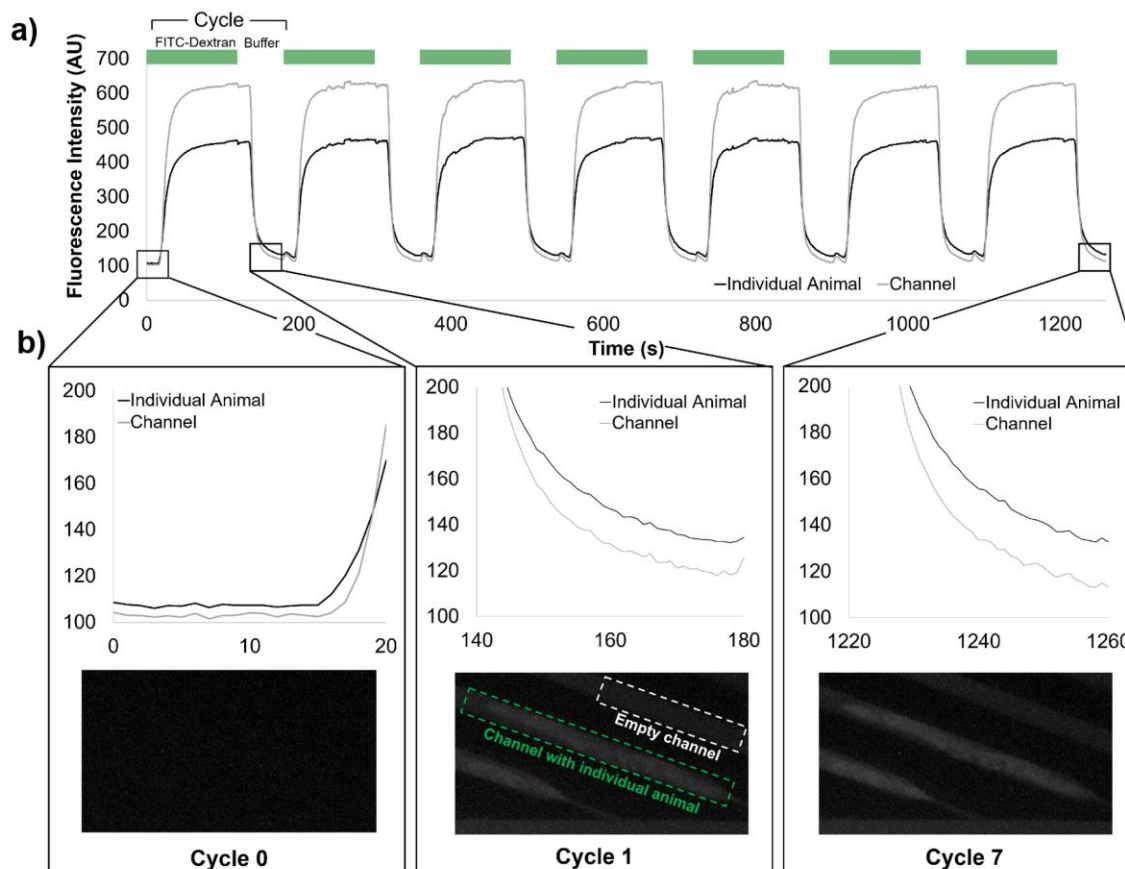


**Figure 2.2 Multiple cycles of reagent delivery can be consistently delivered using the microfluidic platform.** (a) Fluorescence intensity of the individual animal and the reference empty channel directly preceding the worm. Cycles of FITC-Dextran and non-fluorescent buffer are exchanged while tracking the same traps. (b) FITC-Dextran is accumulating in the fixed and permeabilized worms over prolonged exposure to the fluorescent macromolecules.

molecular weight and charge to the smFISH probes, providing a visual, fluorescent representation of the transport. To quantify the extent and the dynamics of the reagent exchange on chip, we measured FITC-Dextran's fluorescence intensity in different areas on the chip over multiple cycles of reagent exchange (Fig. 2.2). By design of the device, the worms were loaded and trapped by the narrow width of the resistance channel at the end of each trap. The channel was high enough to leave space above the worms for sufficient fluidic exchange, even when the worm was properly loaded. Each cycle of



exchange was 120 s of FITC-Dextran and 60 s of S Basal, a nonfluorescent buffer. We quantified both the intensity in the fluidic channels (characterizing fluid delivery) and the intensity on the worm (characterizing the reagent delivery into the worm). The results showed that the reagent exchanges over multiple cycles was efficient and has consistent dynamics across all traps (Fig. 2.2a). The time between starting reagent delivery and its transport into the worm traps was consistent as well as its dynamics. Further, over the multiple exchanges of FITC-Dextran, the exposure to the fluorescent molecules led to its delivery and accumulation into the fixed and permeabilized animals on-chip (Fig. 2.2b). This implied that the smFISH probes would also be transported into the organisms, further demonstrating that reagent delivery into the whole organisms was successfully achieved. We then compared reagent delivery efficiency with the traditional off-chip technique.

After the fixation and permeabilization steps of smFISH, the worm became a hydrated nanoporous matrix. The reagent transport in the traditional off-chip approach is dominated by diffusion. To enhance the transport into other biological systems, vortex shakers can be used; however, this treatment introduces harsh shear that may damage the fragile worms' tissues. In contrast, gentle flow on the microfluidic chip introduced convection, enhancing the transport of reagents into the worm. We hypothesized that reagent delivery was more consistent and much faster than the off-chip approach (Fig. 2.3a). When quantifying the amount of FITC-Dextran delivered into the worm after 10 mins of exposure to the fluorescent FITC-Dextran solution, the on-chip worms were significantly brighter than when using the off-chip protocol (Fig. 2.3b). This indicated that more of the fluorescent reagent was transported into the worm in the same time frame.

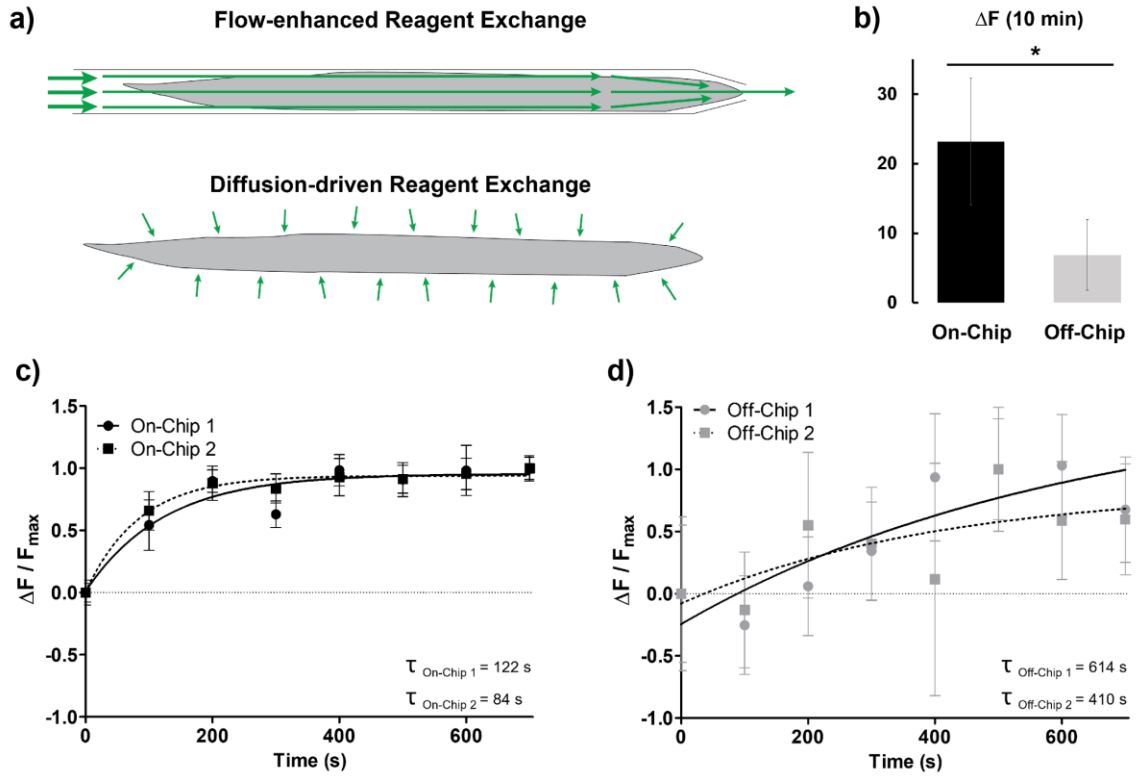


**Figure 2.3 The microfluidic-based platform enhances reagent exchange by introducing convection.** (a) On-chip reagent exchange is flow-enhanced. Off-chip reagent exchange is slower as it is diffusion-dominated. (b) After 10 minutes of exposure to FITC-Dextran, worms on-chip were significantly brighter than worms incubated off-chip. (c) On-chip dynamics of FITC-Dextran accumulation is much faster and more consistent than (d) off-chip dynamics. Error bars represent standard deviation. An unpaired T-test was performed. (\* $P < 0.05$ )

To characterize the kinetics of the reagent delivery, I quantified the dynamics of reagent delivery over time and fit a one phase association curve to each trial, allowing for the calculation of the transport time constants,  $\tau$  (Fig. 2.3c,d), to compare the speeds of delivery. This demonstrated that not only did the on-chip approach have shorter time constants on-chip, which corresponds to faster delivery, but also, they were much more consistent and repeatable when compared to off chip (Fig. 2.3c,d). This consistency was crucial for smFISH in order to minimize any experimental variability and capture true biological variability. Overall, we found the dynamics and delivery of reagents were more

efficient on-chip than off-chip, supporting that our flow-enhanced reagent exchange was more effective than diffusion.

### 2.4.3 Adapting smFISH in whole organisms on chip

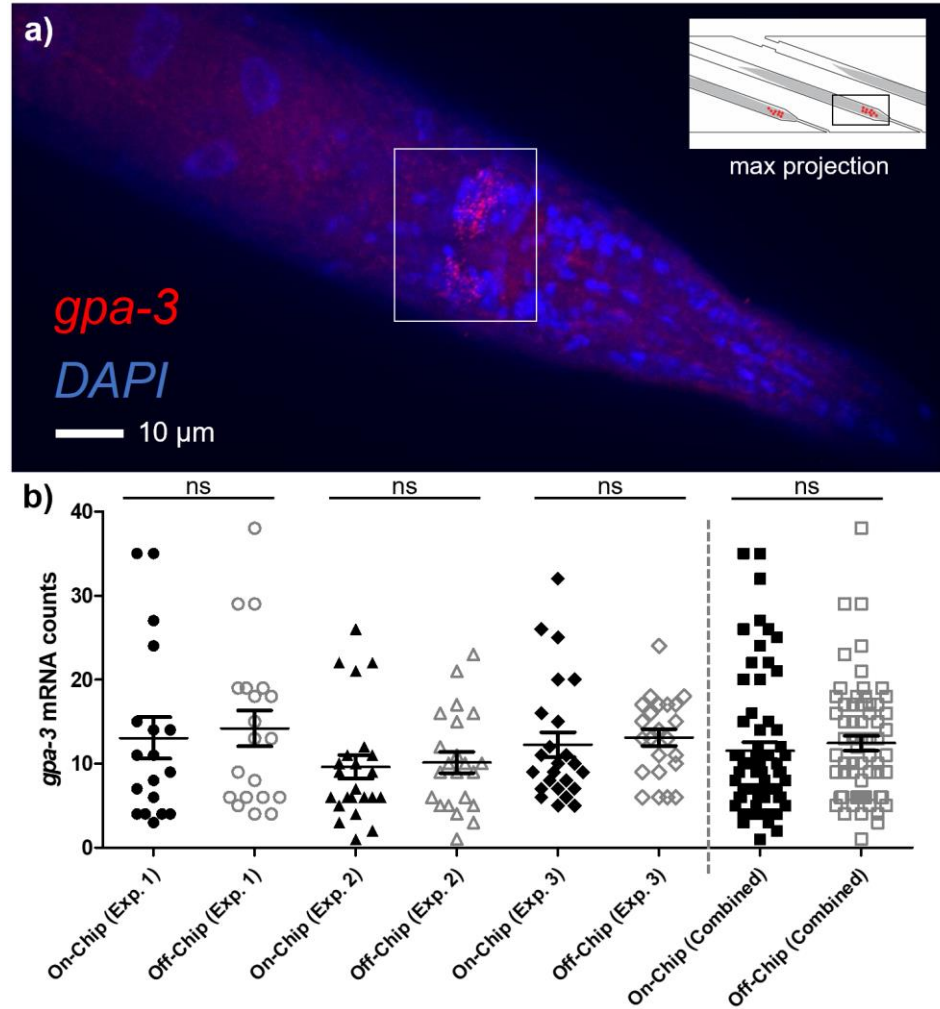


**Figure 2.4 smFISH on whole animals using the microfluidic-based pipeline.** (a) Representative maximum projection image of an individual animal after smFISH. Red puncta represent individual *gpa-3* mRNA molecules; DAPI staining for nuclei is in blue. Puncta are concentrated on the nerve ring of the animal. (b) Quantification of the puncta is consistent between on- and off-chip controls, repeated in 3 separate experiments. Each experiment was a different cohort of animals while each on- and off-chip comparison was from the same population. Error bars represent standard error mean. The Mann-Whitney U test was performed. (ns, not significant)

We next aimed to demonstrate the utility of the device, using smFISH as an example of an end-point assay. smFISH in whole organisms requires multiple reagents to be delivered over multiple days. By using our microfluidic-based platform, we eliminated the need for difficult manual handling of the samples. Our device also allowed us to maintain individuality from loading the device to performing smFISH. Qualitatively, we were able to validate our process by visualizing individual smFISH puncta for the neuronally-expressed gene, *gpa-3* (Fig. 2.4a). With DAPI staining, we were also able to localize the expression to individual cells in neurons and inter-neurons, with most of the expression concentrated in the nerve ring of the animals (Fig. 2.4a). Along with this visual verification, we validated the quantitative smFISH results (*i.e.*, number of puncta or mRNA molecules).

To do so, groups of worms that were cultured together were separated for smFISH on- and off-chip over multiple experiments. Three independent biological and technical repeats were performed. We used FISH-quant, a standard MATLAB program developed by Mueller et. al,<sup>68</sup> to quantify the mRNA counts. We found that the mRNA counts were consistent between the on- and off-chip conditions (Fig. 2.4b). We also found that the standard error of the mean was similar between our on- and off-chip conditions (Appendix A.2.1), suggesting that the measured biological noise was similar between the two conditions, and our on-chip protocol did not introduce significant experimental variability. In this example, we investigated *gpa-3*, a gene expressed in the neurons and inter-neurons of the animal.<sup>10,69</sup> Overall, these experiments validated that our smFISH protocol was reliable and compatible on-chip, did not bias the population, and was properly optimized for future investigations.

#### 2.4.4 Coupling live imaging and smFISH within individual organisms

We next sought to highlight the power of our microfluidic platform's ability to maintain individuality by examining the relationship between two food-sensing genes, *daf-7* and *gpa-3*. *daf-7* expression has been characterized to be responsive to bacterial food levels. In comparison to well-fed worms, *daf-7* expression in starved populations was reduced.<sup>9</sup> DAF-7 functions in many diverse pathways, and its expression is particularly important for organismal development, physiology, and longevity.<sup>16,70,71</sup> *gpa-3* encodes for a G protein  $\alpha$  subunit and has olfactory receptor binding activity. Its function is primarily in chemosensation (*e.g.*, chemoattraction and chemoaversion).<sup>72-74</sup> There was evidence from mutant-based studies that *gpa-3* acts upstream of *daf-7*, but the overall relationship is unclear: one study used qRT-PCR to find that *gpa-3* negatively regulates *daf-7*, while another used a *daf-7* fluorescent transcriptional reporter strain and smFISH for *daf-7* to conclude that *gpa-3* positively regulates *daf-7* in the presence of pathogenic bacteria.<sup>10</sup> These traditional approaches to study multiple genes used mutant strains (*e.g.*, gain-of-function and knockout). This allowed researchers to study how expressions of one gene can influence the expression of another gene. However, importantly, these studies relied on strong genetic perturbations that could potentially carry more significant, unintended consequences.

In contrast, this presented microfluidic-based approach enables us to capture and quantify multiple pieces of information within the same animal, eliminating the reliance on population-based mutant studies (Fig. 2.5). In this demonstration, I loaded a population of *Pdaf-7::Venus* transcriptional reporter strains and imaged them to measure the activity of the *daf-7* promoter. Immediately after live imaging, I delivered fixation and smFISH

reagents to the same samples within an hour of imaging. This fixation process crosslinked biomolecules, including the native mRNA, to its surrounding tissues. A second round of imaging these worms allowed me to quantify the *gpa-3* mRNA counts using smFISH. Since the physiologically relevant time scale for significant *gpa-3* mRNA change, *Pdaf-7::Venus* fluorescence intensity change, and the Venus fluorophore's turnover rate (*i.e.*, days)<sup>11,61</sup> was much longer than our live imaging and fixation time scale (1-2 hours), both measurements can be considered as a single time point.

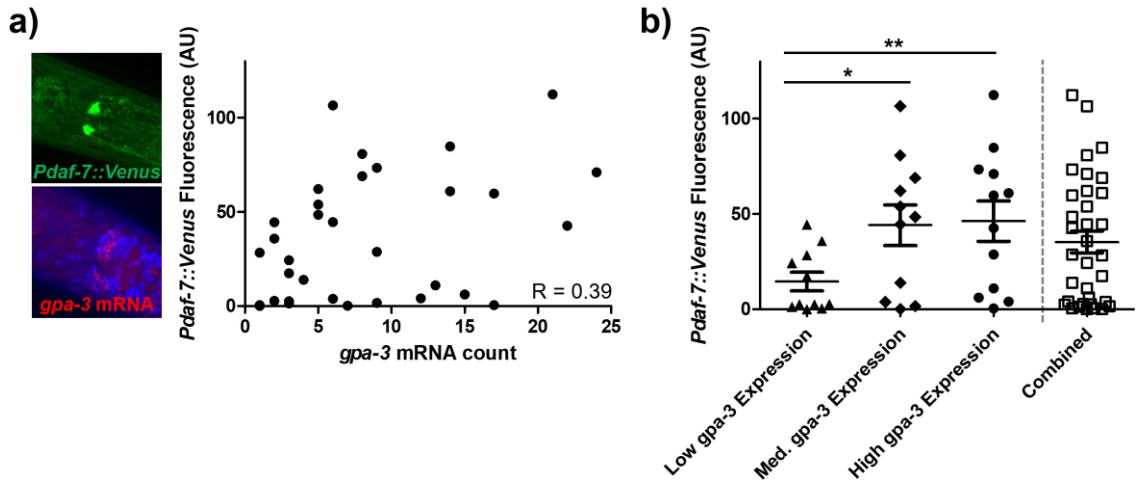


**Figure 2.5. Multi-level gene expression quantification within individual animals.** (a) Each point represents an individual animal with its *daf-7* and *gpa-3* expression, *Pdaf-7::Venus* fluorescence and *gpa-3* mRNA count respectively.  $R = 0.39$ , indicating a low-to-moderate positive correlation. (b) Population binned by *gpa-3* expression reveals a positive relationship. Higher *gpa-3* expression leads to higher *daf-7* expression levels. Error bars represent standard error mean. The Mann-Whitney U test was performed. (\*\* $P < 0.01$ ; \* $P < 0.05$ )

Our microfluidic device retained the individuality at each step, enabling us to measure the *daf-7* and *gpa-3* expression levels in each animal (Fig. 2.5a, Appendix A.1.1). By comparing the gene expression levels in individuals of the whole population, we found a weak-to-moderate positive correlation ( $R = 0.39$ ) between the two genes (Fig. 2.5a). *daf-*

7 plays important roles in many biological processes, and it receives inputs from additional genes including *gpa-3*. We also observed that the natural variability in *daf-7* expression increases with higher *gpa-3* expression, where worms with medium- and high-expression of *gpa-3* tend to have more stochasticity in their *daf-7* expression (Appendix A.2.2). This was expected as an increase of *gpa-3* expression led to a stronger, competing input to *daf-7*, which added complexity to its expression.

This approach enabled us to study the biological expression distributions of *gpa-3* and *daf-7* in detail with single-animal resolution. Since *gpa-3* acts upstream of *daf-7*, our platform allowed us to quantify the resulting *daf-7* expression of the natural stochasticity of *gpa-3* expression. By separating and binning the individuals based on their *gpa-3* expression, we found that the populations also had the same positive trend where higher *gpa-3* expression led to significantly higher *daf-7* expression (Fig. 2.5b, 2.6), and this conclusion was robust to the exact binning (Fig. 2.6). This type of binning allowed us to recapitulate the traditional methods using mutants: a knockout or loss-of-function mutant (low *gpa-3* expression), a wildtype condition (medium *gpa-3* expression), and an overexpressing or gain-of-function mutant (high *gpa-3* expression).

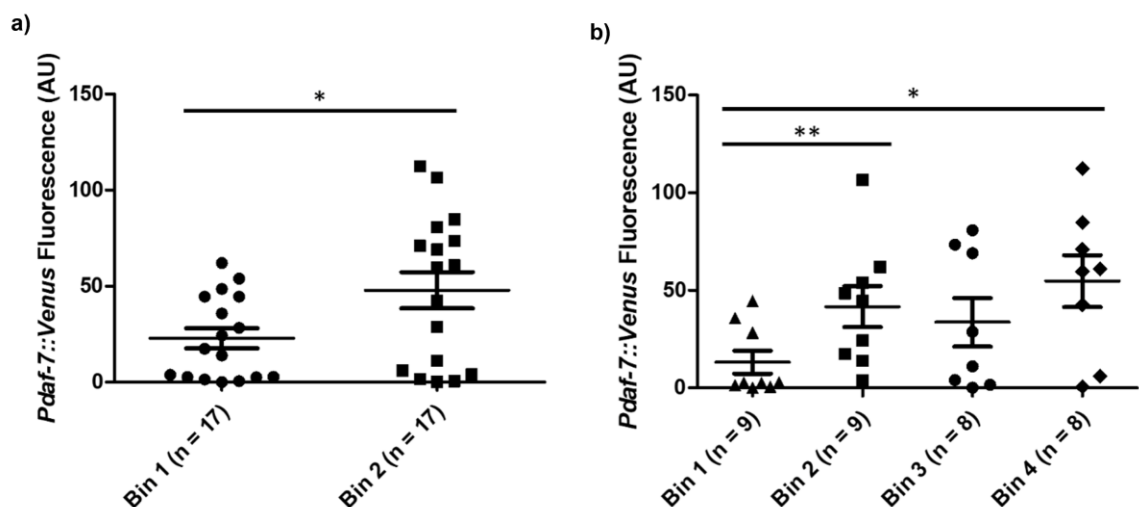


**Figure 2.6 The positive relationship between *gpa-3* and *daf-7* expression is consistent regardless of bin size.** The binning is based on *gpa-3* mRNA expression quantified from smFISH. Higher *gpa-3* expression correlates with significantly higher *Pdaf-7::Venus* expression when the population is divided in (A) 2 bins or (B) 4 bins. The Mann-Whitney U test was performed. (\*\* $P < 0.01$ ; \* $P < 0.05$ )

Using mutants, previous studies suggested that the relationship between *gpa-3* and *daf-7* is complex.<sup>10,14</sup> It was possible that the subtle nuances and natural variability of the relationship between this pair of genes were masked in the traditional off-chip population-based comparisons, while our method can preserve such information. Further, genetic mutations and manipulations may affect the expressions of related genes in unforeseen ways. Here, I presented a complementary approach to traditional mutant-based studies. This work demonstrated and validated an approach to measure gene expression and the gene-gene relationship in a single, native genetic background. When comparing the binned populations (Fig. 2.5b, 2.6), we could see these trends emerge where higher *gpa-3* expression correlated with higher *daf-7* expression. These trends would have been less obvious when considering whole population averages, similar to our measurements in



Figure 2.5a. Our gene-gene correlation result in single worms suggested that *gpa-3* may play indirect roles in via *daf-7* in processes, such as development and longevity.

## 2.5 Conclusions

In this study, I engineered a novel microfluidic-based pipeline and approach that enables us to discover gene expression relationships by retaining the inter-individuality of whole organisms throughout multiple bioassays. By automating reagent exchanges on-chip, I was able to perform complex biological assays robustly, repeatedly, and significantly faster than traditional, diffusion-dominated off-chip approaches. Next, I demonstrated the biological utility of our platform by adapting and performing smFISH. Following, I applied the microfluidic-based approach and discovered the relationship between two food-sensing genes, *gpa-3* and *daf-7*. By quantifying both gene distributions, I could examine how the natural variability of *gpa-3* correlated with the stochastic *daf-7* expression within individuals. While the traditional off-chip approach relied on the use of functional mutants, the microfluidic platform enabled us to preserve the native gene expression networks, presenting a new complementary technique to study gene expression relationships in a single genetic background.

In this work, I demonstrated an example of how coupling live imaging of a fluorescent transcriptional reporter with an endpoint assay, smFISH, can result in multi-dimensional data. This strategy is readily adaptable to other existing microfluidic devices, such as *Drosophila* embryo traps to study embryogenesis<sup>75</sup> and arrays for high-throughput single-cell analysis,<sup>76</sup> to couple other dynamic live-imaging phenotypes to gene expression analysis. Additionally, live imaging does not have to be limited to fluorescent imaging; one

possible example is first quantifying the behavior in a population of *C. elegans* using a microfluidic chamber array and then performing smFISH in the same array to identify genes related to the behavioral phenotype. Further, many genomic-based studies require non-transgenic animals, such as genome-wide association studies (GWAS), which also makes smFISH an attractive method. This integrated tool presented here can also be applied to other popular small model organisms, such as tunicate, Hydra, *Drosophila*, and other roundworms, where one can investigate gene expression in a natural population and couple it to live phenotype.

In summary, this work established a generalizable pipeline to investigate and quantify gene expression relationships. In this field alone, this pipeline could be adapted for future studies such as quantifying development- or age-related changes of gene expression, measuring the weights of expression relationships, or even studying how external perturbations impact gene expressions (*e.g.*, toxicology screening, food/diet levels, temperature, etc.). This tool presents a new opportunity to help uncover gene networks, pushing us one step closer to understanding how these networks arise and revealing any underlying mechanisms that govern living systems.

## **CHAPTER 3.     DESIGNING MICROFLUIDIC-BASED METHODS TO ACHIEVE MULTIPLE CYCLES OF SMFISH WITH INTER- INDIVIDUAL RESOLUTION**

This chapter describes two approaches to achieve multiple cycles of smFISH. The first portion discussing the electrokinetic and microfluidic hybrid device is adapted from “Rapid and multi-cycle smFISH enabled by microfluidic ion concentration polarization for *in situ* profiling of tissue-specific gene expression in whole *C. elegans*,” published in 2019 in *Biomicrofluidics*<sup>77</sup> and was co-authored in collaboration with Dr. Gongchen Sun. The second approach details a formamide-based stripping reagent used in a previously published microfluidic device.<sup>78</sup>

### **3.1 Introduction**

smFISH is a powerful technique to characterize gene expression with tissue-specificity in whole organisms. While some of this assay’s limitations were addressed in the previous chapter’s work, the traditional protocol requires lengthy incubation times, and importantly, it is challenging to perform multiple cycles of smFISH in a whole organism. Currently, only single round smFISH has been achieved in whole organisms, severely limiting gene expression studies to 1-3 genes (*i.e.*, the number of resolvable fluorophores) per animal. In mounted cells and thin slices of tissue (~10  $\mu\text{m}$ ), others have shown that multiplexing techniques can reach transcriptome-level information, but they require sequential probing of different genes and demand efficient transport.<sup>79</sup> The major bottleneck to adapting this technology to whole animals is the inefficient macromolecule

exchange through traditional diffusion-dominant techniques across dense tissues and retaining inter-individual identities. In this aim, I address this challenge with two approaches: (1) developing a microfluidic/electrokinetic hybrid platform to enhance transport using DNase I as the stripping reagent, and (2) using a formamide-based stripping reagent and convection-based approach to enable multi-cycle smFISH in an intact organism. It was important to investigate both reagents as neither have been used for smFISH probe stripping in *C. elegans* and each reagent has its own advantages which we aim to highlight in this chapter.

### **3.2 Background**

Investigations using model organisms, such as *C. elegans*, *Drosophila*, and *Danio rerio*, have shown that gene expression is cell-/tissue-, age-, and individual-dependent.<sup>12,13,80,81</sup> One promising technique to capture all these pieces of information is smFISH, as introduced in the previous chapter. Advanced smFISH technologies that use multiplexing and barcoding techniques can quantify the entire transcriptome.<sup>43,44</sup> This approach requires multiple rounds of hybridizing the smFISH probes, stripping the probes (with DNase I<sup>82</sup> or formamide-based<sup>44</sup> reagents), and re-hybridizing them in the same sample. Although robustly achieved in simple systems, adapting multiplexing techniques to whole organisms presents significant transport challenges to achieve a sufficient probe concentration in the organism as well as probe removal. Whole *C. elegans*, for example, are thicker (~50-70  $\mu\text{m}$ ) than tissues slices (~10  $\mu\text{m}$ ) and contain complex, heterogeneous tissue types. Even single rounds in whole animals usually require long incubation times for probe hybridization due to the combinatorial probing nature of smFISH strategy.

Therefore, when using smFISH in whole organisms, the number of genes studied is usually limited by the number of fluorophores the imaging setup can resolve.

Intact whole organisms have dense tissues. Even after fixation and permeabilization, transporting reagents in and out of the sample can be difficult – especially in larger adult animals. In the traditional approach, multiple organisms are typically incubated together in a single small tube with smFISH probes overnight, the reagent delivery is diffusion-dependent, and individual identities are lost.<sup>83</sup> smFISH probes are expensive and maintaining individuality (*i.e.*, using a separate tube for each animal) is extremely costly, time-consuming, and labor intensive. Although the traditional approach is sufficient for a single round of smFISH, multiplexing requires multiple reagents to be delivered in and out of the sample over multiple steps while tracking the same individual: (1) the original probes need to be delivered, (2) the stripping reagents need to be delivered, (3) the de-hybridized probes and stripping reagents need to be removed, and (4) the new probes need to be re-delivered. With the ability to perform multi-cycle smFISH, we can potentially examine complete gene networks and expression dynamics with tissue- and cellular-specificity within individual whole organisms; however, the major limitation to adapting these higher-level strategies is the precise reagent delivery and removal needed in different steps.

To address these requirements, we propose 2 solutions. First, we engineered a platform that combines the advantages of microfluidics and electrokinetics (EK) to enable rapid and multicycle smFISH in *C. elegans*.<sup>77</sup> Our device consists of two components: a microfluidic trap array and an ICP-based ion pump using a nanoporous cation exchange membrane (CEM). By efficiently transporting and enriching probes across tissue barriers in the whole worm, we shorten the smFISH process by an order of magnitude. Similarly,

our second solution allows us to track individuals over multiple cycles by using a traditional microfluidic chamber array device. Although the kinetics of transport are not as fast as the EK-based hybrid device, formamide is a gentler reagent and preserves the integrity of the animals' tissues. In addition, the geometry of this device allows for larger sample sizes (60 traps vs. 20 traps in the EK device).

Increasing gene expression studies from 1-2 genes to 2-4 genes with multicycling is a demonstration to directly addresses the practical limitations of traditional smFISH. Current smFISH-based studies can only study 1-2 interactions within a complex gene network. Although this can be useful for specific studies, such as studying the relationship between related genes *daf-7* and *gpa-3* in **Chapter 2**, it severely limits the types of questions researchers can ask. Increasing investigations to 2-4 genes, we can begin to ask how networks may respond to perturbations, measure how genes are regulating each other, and possibly describe how external stimuli may influence different pathways. For example, food levels greatly influence lifespan and corresponding gene expression. With the ability to study multiple genes, we can examine genes specific to different food/environment sensing pathways (*e.g.*, *daf-7* for TGF $\beta$ , *tph-1* for serotonin, *cat-2* for dopamine, *tdc-1* for octopamine) within a single animal and measure how they might be influenced differently. We demonstrate in this work that we can achieve 2 rounds of smFISH, and we believe that this technology can be further developed to perform even more cycles with simple modifications.

### 3.3 Materials and Methods

#### 3.3.1 *C. elegans strains, culture, and sample preparation*

The worms used in this work were N2 strain (QLN2). All worms were grown on standard NGM agar plates with *Escherichia coli* (*E. coli*) OP50 lawns and maintained at 20 °C for two generations. Synchronized L1 larvae of the F2 generation were obtained from a 2 hour hatch off. For the electrokinetics/microfluidic work, hermaphrodite worms were synchronized to Day 2 adults before being washed off plate for experiments using S Basal. For the formamide-based work, worms were synchronized to young adults (Day 0 adults). The formamide-based work used younger animals because the genes selected for those studies are more highly expressed in younger stages.

The populations of worms were then sacrificed and fixed in 3.7% formaldehyde for 45 minutes; this process crosslinks the biomolecules including native mRNAs with the surrounding tissues. After fixation, they were washed and incubated in 70% ethanol overnight at 4 °C for permeabilization of the tissues.

#### 3.3.2 *E. coli culture/rep and feeding assay*

Using the formamide-based stripping approach, I quantified the gene expressions of animals fed on different food levels. QLN2 animals were grown on standard NGM agar plates with *E. coli* OP50 lawns and maintained at 20 °C for two generations. Synchronized L1 larvae of the F2 generation were obtained from a 2 hour hatch off and directly transferred to plates seeded with either OD<sub>600</sub> 1 (low food) or OD<sub>600</sub> 10 (high food).

Bacterial culture protocols are similar to previously published protocols.<sup>9,78</sup> Briefly, *E. coli* OP50 was grown overnight in filtered and autoclaved LB at 37 °C within a shaking incubator. Following, the cultures were shocked in streptomycin at 50 µg/mL for 30 min while shaking and then chilled on ice for 15 min before being centrifuged at 4500 x g for 25 min. The supernatant was decanted, and the bacteria were resuspended in S Basal containing streptomycin (50 µg/mL). The volume required was determined by measuring the OD<sub>600</sub> of the sample prior to centrifugation and then calculating the volume required to give the resuspended culture an OD<sub>600</sub> of 10. This was then diluted 10x for the OD<sub>600</sub> 1. The bacteria were then seeded on 10 cm NGM plates and left to dry for 2 days.

### 3.3.3 Device fabrication

For both devices, the master mold of the microfluidic device was fabricated with a negative photoresist, SU-8 2050 (Microchem) by UV photolithography. The microfluidic device used in the formamide-based studies was fabricated in polydimethylsiloxane (PDMS, Dow Corning Sylgard 184) by soft lithography as previously described.<sup>78</sup>

For the electrokinetic/microfluidic hybrid devices,<sup>77</sup> briefly, we spin-cast the microchannel layer PDMS (10:1 ratio between the elastomer and the curing agent) on the master mold at 750 rpm for 30 seconds. This microchannel layer was partially cured at 75°C for 15 minutes. Cut pipette tips with a filter paper at the bottom as buffer reservoirs and a 1.5 × 25 mm CEM strip (Mega a.s., Czech Republic) were placed at the designated positions on the partially cured PDMS layer, fixed by Kapton tape. More PDMS (10:1) was poured onto the microchannel layer to embed the cation exchange membrane and buffer reservoirs. The entire device was then cured at 75 °C for 90 minutes. After peeling



off the device from the SU-8 master, through-holes for electrical connection were cut underneath the CEM and the buffer reservoirs, and the through-holes for fluidic connection were punched by 19-gauge needles (McMaster-Carr). Finally, the device was bonded onto a pre-cleaned coverslip using corona discharge followed by thermal bonding at 75 °C for 24 hours. After the device was completed, 200  $\mu$ L 2% agarose gel were placed in the input reservoir to prevent fluid leaking from the channel into the reservoir. All devices were filled with 1X S-basal buffer for 48 hours to let the CEM swell properly prior to test.

#### *3.3.4 Device operation*

For the electrokinetic/microfluidic hybrid device, the external electric voltage signal was generated by a Keithley 2450A SourceMeter Instrument (Tektronix) and transmitted into the microfluidic device using platinum electrodes. The electrodes were placed in buffer reservoirs separated from the main microfluidic channel by 2% agarose gel plugs to prevent electrochemical byproducts, such as bubbles and pH changes, leaking into the microfluidic channel.

The formamide-based microfluidic approach was operated as described in the previous chapter using syringe pumps<sup>65</sup> with a previously published device.<sup>78</sup>

#### *3.3.5 Imaging, image processing, and analysis*

For the electrokinetic/microfluidic hybrid approach, imaging was performed on a spinning disk confocal microscope (PerkinElmer UltraVIEW VoX) using a Hamamatsu FLASH 4 sCMOS camera. For the formamide-based microfluidic approach, imaging was performed on a spinning disk confocal microscope (Nikon W1 Spinning Disk Confocal)

using a Hamamatsu ORCA-Fusion Gen-III sCMOS camera. Images were analyzed and puncta were identified using a standard software, FISH-quant.<sup>68</sup> To quantify the signal-to-noise ratio (SNR), we measured the maximum intensity of each puncta (signal) and divided by the standard deviation of the intensities of the head of the worm, anterior to the gut (noise), using ImageJ. To quantify the signal-to-background ratio, we measured the maximum intensity of each punctum (signal) and divided by the average intensity of the head of the worm, anterior to the gut (background), using ImageJ. The plots and statistics were created using GraphPad Prism.

We used fluorescein isothiocyanate (FITC)-Dextran (1mg/mL) in either the hybridization buffer or the wash buffer for smFISH to characterize the probe delivery and removal to the worms in the electrokinetic/microfluidic device. FITC-Dextran was chosen as an approximation of smFISH probes in this characterization because it had a much cheaper reagent cost and was more easily acquired commercially. In addition, this fluorescent reagent has a similar molecular weight and charge to smFISH probes. The probe transport dynamic by fluorescence was recorded with whole field illumination on a fluorescence dissecting scope (Leica, MZ16F) with a frame rate of 5 fps, and a 100 ms exposure time. To quantify the dynamics and intensities, we used a custom MATLAB code. The plots and statistics were created using GraphPad Prism.

### 3.3.6 Multi-cycle smFISH

Probe design and the protocol to perform smFISH in *C. elegans* have been previously described.<sup>42</sup> In this study, I used a custom Stellaris smFISH probes for specific targeting *gpa-3* labeled with Cal Fluor Red 610 (mCherry or RFP equivalent), *tph-1* and

*tdc-1* in TAMRA, and *daf-7* and *cat-2* in Quasar 670 (Cy5 equivalent). The fixed and permeabilized samples were incubated in S Basal for 5 minutes. Next, they were washed with wash buffer (10% formamide, 2X SSC, in nuclease-free water) for 5 minutes. For off chip experiments, the worms were incubated in custom probes (1.25  $\mu$ M) in hybridization buffer (1 g dextran sulfate, 40  $\mu$ L RNase-free BSA (50 mg/mL), 10% formamide, 9 mL nuclease-free water) at 30°C. For on-chip experiments, worms were first manually loaded into the device. To transport the probes into the worms, we flowed the smFISH probes into the device using a syringe pump at 15  $\mu$ L/min for 3 minutes, applied -150 V from the input reservoir for 5 minutes, and continued flow for 2 minutes. The device was then incubated at 30°C while under slow flow (10  $\mu$ L/hr) to prevent evaporation. Prior to imaging, the worms were incubated in wash buffer for 30 minutes, following previous literature.<sup>42</sup> This short washing step was to remove free-floating probes in the microchannels which might interfere with the fluorescence imaging.

To strip the probes from the sample in the electrokinetic/microfluidic hybrid approach, we prepared a DNase I stripping reagent (0.5 U/  $\mu$ L). The reagent was flowed into the device at 15  $\mu$ L/min for 3 minutes, then 10  $\mu$ L/hr at 30 °C for 4 hours. To remove the stripped probes and DNase I, we applied +150 V from the input reservoir for 5 minutes. Prior to imaging, we washed the worms in wash buffer for 30 minutes at 15  $\mu$ L/min. To re-hybridize the worms, we followed the same protocol as above.

To strip the probes from the sample in the formamide-based microfluidic approach, I prepared stripping buffer as wash buffer with 60% formamide. The reagent was flowed into the device at 15  $\mu$ L/min for 30 minutes at 30 °C. Prior to imaging, the worms in wash

buffer for 30 minutes at 15  $\mu\text{L}/\text{min}$ . To re-hybridize the worms, I followed the same protocol as in the previous chapter.<sup>65</sup>

### 3.4 Results and Discussion for the Electrokinetic/Microfluidic Hybrid Approach

#### 3.4.1 Design of electrokinetic/microfluidic hybrid device to enhance transport

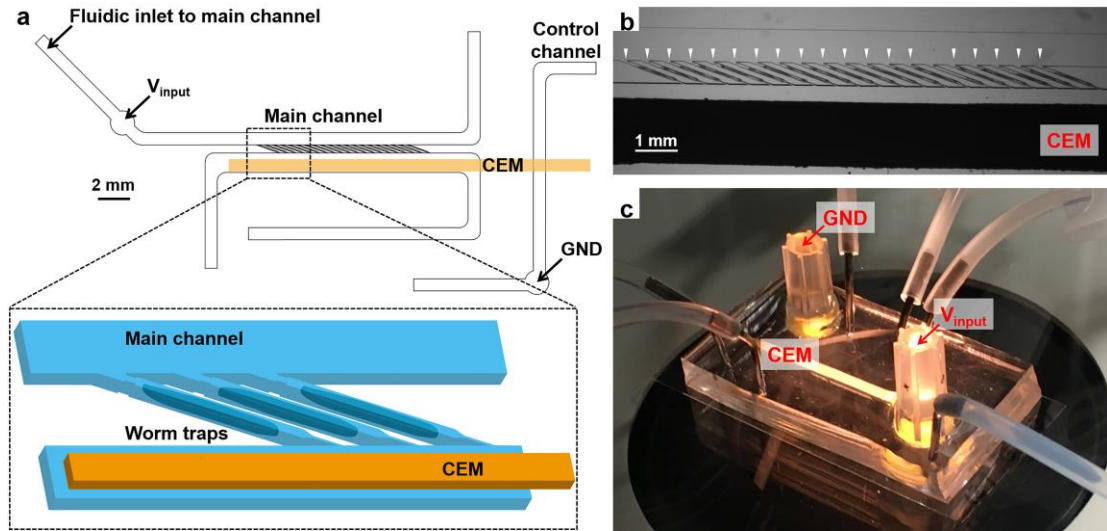


**Figure 3.1 Overview of device design.** (a) Schematic of the microfluidic/electrokinetic hybrid device. (b) Micrograph of individually loaded worms in worm traps. White arrowheads indicate individually loaded adult worms. (c) Image of the device setup.

To incorporate smFISH multiplexing techniques of whole organisms, it requires the preservation of individual identities of the animals throughout the entire process in order to quantify genes from multiple rounds per individual. In our platform, this is guaranteed by isolating individual *C. elegans* into an array of trackable worm traps (Fig. 3.1a). A group of age-synchronized adult worms can be loaded in traps within a minute by allowing fluidic flow across the trap array (Fig. 3.1b). As shown in Figure 1a, the ion pump is built by placing a strip of CEM on top of the main channel, closely adjacent to the end of the traps and bridging the main channel to a separated control channel. To induce the ion

concentration polarization and control the probe transport, DC electric fields are introduced to the worm traps through the CEM by inserting one electrode in the input reservoir on the main channel, and another electrode in the ground reservoir on the control channel (Fig. 3.1a, c).

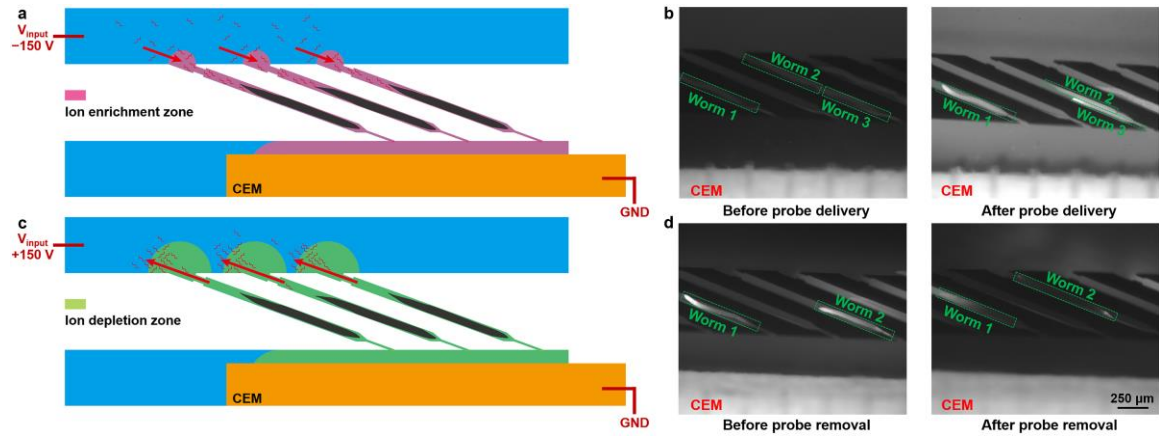


**Figure 3.2 Device operation schematic.** (a) Operating principle of probe delivery. (b) Fluorescent images of FITC-Dextran (model of smFISH probes) transport into individual worms before and after probe delivery process. The input reservoir received -150 V for 5 minutes. (c) Operating principle of probe removal. (d) Fluorescent images of FITC-Dextran transport out of individual worms before and after probe removal process. The input reservoir received +150 V for 7 minutes. The image settings (brightness and contrast) are consistent for all fluorescent images in (b) and (d).

Because of the charge selectivity of the cation-exchange membrane, ion concentration polarization can be established under DC electric fields in the vicinity of the CEM, which is, in our case, in the worm traps. When imposing a negative voltage at the input electrode, negatively charged nucleic acid probes are continuously transported by electrophoresis into the worm traps, where an ion enrichment zone is established (Fig. 3.2a). The electrophoretic force efficiently drives the probes through the cuticle and dense tissues of the fixed and permeabilized worms, and the negative gradient of electric field from the main channel to the traps ensures the probes concentrated in the worms. To

characterize the probe enrichment process, we used fluorescein isothiocyanate (FITC)-Dextran as a model for the smFISH probes because they have a similar molecular weight and charge. Figure 3.2b shows that after 5 minutes of enrichment by the ICP-based ion pump, FITC-Dextran molecules are predominately concentrated in the loaded worms, characterized by the elevated fluorescence intensity in the worm (Fig. 3.3).

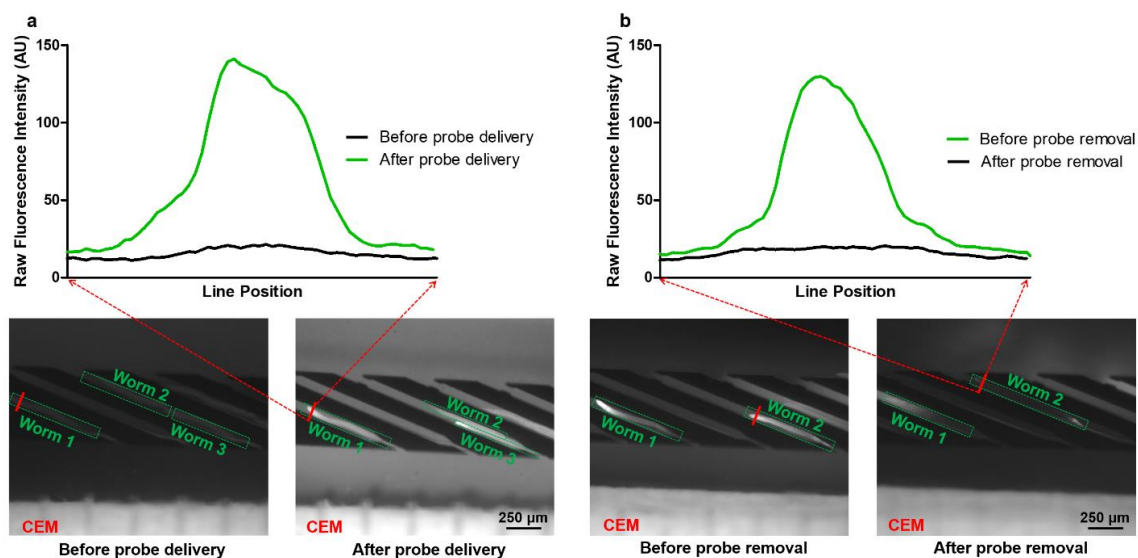


**Figure 3.3 Characterization of raw fluorescence intensity profiles of the worms.** (a) before and after probe delivery and (b) before and after probe removal. The image settings (brightness and contrast) are consistent for all fluorescent images

This electrokinetic probe enrichment strategy can drastically reduce the time required for smFISH in two stages: probe delivery and probe hybridization. The following is explained in much greater detail in Appendix B.1. Briefly, in the first stage, the electrophoretically driven transport accelerates the probe delivery to target mRNA molecules in the worm, compared with the traditional diffusion-dominated method. We can define the “acceleration” of probe transport by the ratio of characteristic diffusion-based probe delivery time,  $t_{diffusion}$ , to the characteristic electrokinetically-enhanced

time,  $t_{electrokinetics}$ . Based on the geometrical design of our microfluidic chip, the “acceleration”  $t_{diffusion}/t_{electrokinetics}$  is scaled with  $(\frac{d_{worm}}{l_{worm}})^2 \frac{V_{input}}{RT/F}$  (see Appendix B.1 for details). Here  $d_{worm}$  and  $l_{worm}$  are the diameter and length of the worm, respectively, and  $V_{input}$  is the applied electrical potential. Considering the aspect ratio of the worm and our ~150 V applied voltage, the probe delivery can be enhanced by at least 20 folds.

In the second stage, after probes are delivered into the worm, they are enriched; this higher probe concentration results in a rapid hybridization between probes and the target mRNA molecules. The kinetics of such hybridization can be approximated as a second-order reaction. The characteristic time for 90% target mRNA molecules hybridized with at least 20 probes,  $\tau_{90\%}$ , is given by  $\tau_{90\%} = -\ln(1 - \sqrt[20]{0.9}) / k_{on} C_{probe}^0$ , where  $C_{probe}^0$  is the enriched initial concentration of probes and  $k_{on}$  is the hybridization rate constant (see Appendix B.2 for details). Based on the numerical simulation of ion concentration profile near an ion-selective media<sup>84,85</sup> and the ion current profile during our experiments, we estimate the ion and probe concentration in the worm are enriched by 3-5 folds during the non-equilibrium probe delivery step. In contrast, using the traditional diffusion-based protocol, the maximum probe concentration in worms can only reach as high as the equilibrium concentration in the buffer. The elevated ion concentration does not affect the probe hybridization mechanism in the hybridization buffer,<sup>86</sup> nor the penetration of the probes into the worms.<sup>87</sup> Thus, the subsequent incubation time required for sufficient probe hybridization onto the target mRNAs can be reduced; this time is scaled inversely proportional to the enriched probe concentration. Traditional diffusion-based protocols require overnight incubation (12-24 hours) in order to complete the probe hybridization. In

contrast, combining the enhancement by probe delivery and probe hybridization with our non-equilibrium method, we can shorten the probing step during each round of smFISH to a few hours. Hence in later smFISH experiments, we chose to perform probe delivery with our ICP-based ion pump for 5 minutes and a subsequent 4-hour incubation for probe hybridization.

After the target mRNAs are probed and imaged, the probes can be stripped from the *in situ* mRNA with DNase I; this then allows for profiling of other genes. Once stripped, (1) the DNase I must be removed to allow for future probe hybridization, and (2) the de-hybridized fluorescent probes need to be removed from the animals; otherwise, the stripped probes are likely to elevate the background fluorescence level, which may overwhelm the true FISH signals. To accomplish this, we reverse the polarity of the input voltage to positive to develop an ion depletion zone in the traps for the probe removal. Within the ion depletion zone, the ionic strength can be reduced by 2 to 3 orders of magnitude.<sup>84</sup> As a result, the high electric field in the depletion zone can focus the charged probes at the depletion front isotachophoretically,<sup>88-91</sup> illustrated in Figure 3.2c. As the depletion zone grows and the depletion front passes through the loaded worms, charged unbound macromolecules can be removed from the animals almost completely, demonstrated by FITC-Dextran in Figure 3.2d. We designed the CEM surface to be parallel to the bottom wall of the microchannel with only 50  $\mu\text{m}$  separation. Therefore, the electroconvection vortices are effectively suppressed by the large hydrodynamic resistance to avoid arresting the depletion front.



### 3.4.2 Characterization of macromolecular transport through intact tissues

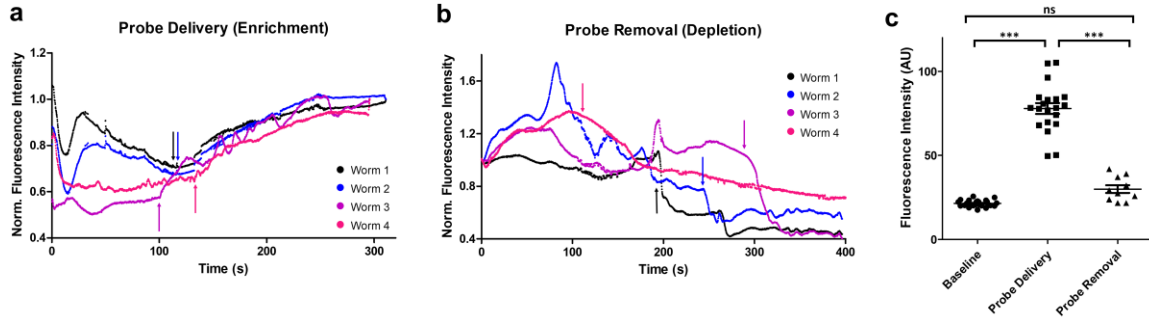


**Figure 3.4 Quantification of fluorescence intensity dynamics in individual worms during the probe delivery process.** (a) -150 V was applied at the input reservoir. Arrows indicate when the ion enrichment zone started to establish for each worm. (b) Quantification of fluorescence intensity dynamics in individual worms during the probe removal process. +150 V was applied at the input reservoir. Arrows indicate when the ion depletion front passed through each worm. (c) Quantification of fluorescence intensity of individual worms at baseline and after probe delivery and removal. A one-way ANOVA and Tukey's multiple comparison tests were performed. (\*\*\*)  $P < 0.001$ ; ns, not significant)

Using FITC-Dextran as a model, we further characterized the dynamics and robustness of the probe delivery (Fig. 3.4a) and removal process (Fig. 3.4b). We measured the fluorescence intensity in the whole worm over time. During the probe delivery step and before the onset of the ion enrichment, FITC-Dextran molecules that were pre-loaded in the traps but not in the worms were driven out of the traps, evident by the initial decrease of the fluorescence intensity (Fig. 3.4a). However, when the ion enrichment zone was established after about two minutes, the samples started to become brighter consistently due to the accumulation of FITC-Dextran molecules in the tissues (Fig. 3.4a). After five minutes of electrokinetic-assisted probe delivery, the samples in the device showed a significantly higher fluorescence intensity (Fig. 3.4c). Similarly, during the probe removal step, we observed a sudden drop of fluorescence intensity from the worms in Figure 3b, demonstrating the removal of these accumulated FITC-Dextran molecules by the depletion

front. While we noticed that FITC-Dextran molecules were removed at different rates in the samples, we found that after seven minutes of electrokinetic-assisted probe removal, the fluorescence intensity of all the worms returned to the baseline level (Fig. 3.4c). The heterogeneity was expected as tissue compositions varied from worm-to-worm, and depletion fronts developed at different time points across the trap array. The fast dynamics enabled by the ICP-based ion pump allows us to rapidly send charged molecular probes into the whole worms repeatedly and robustly, regardless of the tissue barrier of the multicellular organisms.

### 3.4.3 Demonstration of faster and multi-cycle smFISH with enhanced transport

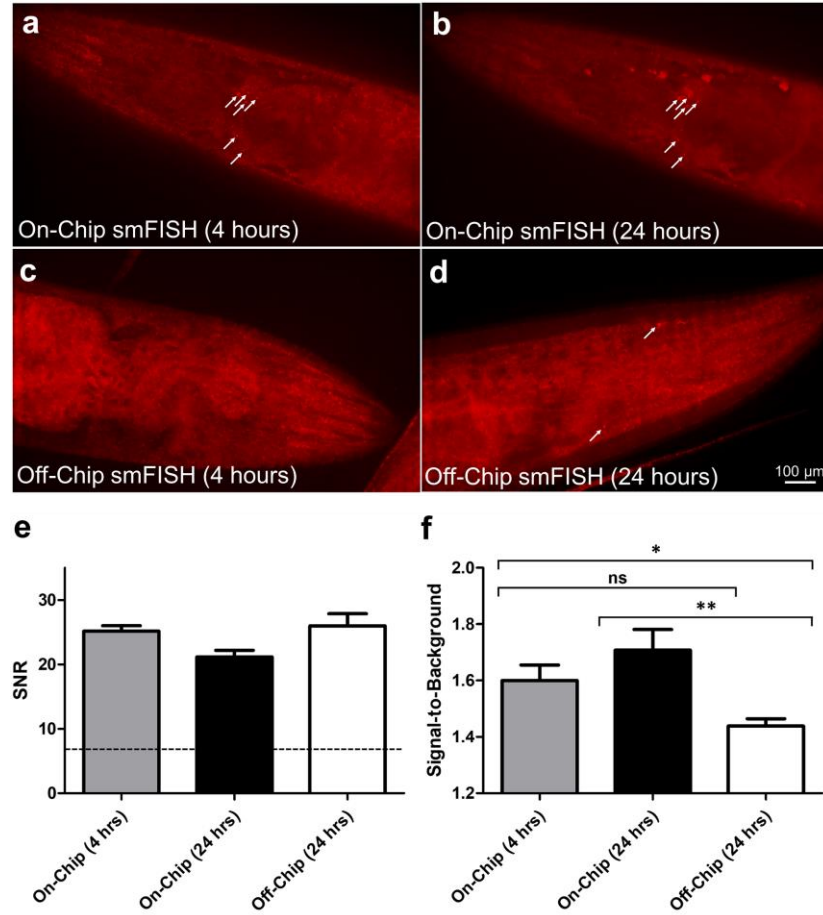


**Figure 3.5 Fluorescent images of individual puncta, each corresponding to a *gpa-3* mRNA molecule in the neuronal cells.** (a,b) On-chip probe delivery by the ICP-based ion pump in the same worm after (a) 4 hours and (b) 24 hours. (c,d) Off-chip diffusion-dominated delivery. (c) Individual puncta were not resolved after 4 hours of off-chip incubation. (d) Puncta are visible only after 24 hours of off-chip incubation. White arrows are added to aid puncta visualization. (e) Signal-to-noise ratio (SNR) of the puncta at each condition. The dotted line corresponds to the minimum value acceptable (SNR = 7). (f) Signal-to-background ratio of each punctum at each condition. An unpaired, two-tailed T test was performed. (\*\*P < 0.01, \*P < 0.05; ns, not significant)

To demonstrate the utility of this device for profiling gene expression, we performed smFISH for a neuronal-expressed gene, *gpa-3*, and compared its performance to the traditional off-chip approach (Fig. 3.5). *gpa-3*'s expression is age-related and its

function is involved in olfactory receptor binding, suggesting that it plays an important role in many biological processes such as gene expression regulation, aging and development.<sup>10,14</sup> Using our device, we improved the probe delivery and increased its local concentration into the worms, shortening the time required for smFISH hybridization step to only 4 hours from the traditional overnight incubation (Fig. 3.5a). After 24 hours of incubation on-chip, we found that the quality of smFISH did not change (Fig. 3.5b,e,f), confirming that our rapid on-chip hybridization step was sufficient to visualize the hybridized probes. In contrast, the diffusion-dominated off-chip approach was unable to produce any obvious puncta after 4 hours of incubation (Fig. 3.5c). Instead, for the off-chip condition, we were only able to resolve puncta after the 24 hour incubation period, which was the typical overnight protocol (Fig. 3.5d).<sup>42</sup>

In all the samples, we found the signal-to-noise ratio (SNR) to be much higher than 7 (Fig. 3.5e), the minimal acceptable SNR previously reported,<sup>68,92</sup> allowing us to confidently identify each punctum. Since unbound probes may contribute to the background fluorescence observed, we quantified the signal-to-background ratio at each time point to validate that the background fluorescence does not become too high to overwhelm the true signal (Fig. 3.5f). We observed that the signal-to-background ratio was significantly higher even with only 4 hours on-chip when compared to the 24 hour off-chip condition (Fig. 3.5f), indicating that smFISH on our platform achieves higher quality signal with less time required. Thus, by increasing the local concentration of probes and improving the probe delivery into the animals, we were able to shorten the time required for smFISH without compromising the quality. By achieving faster smFISH, this work

demonstrates a potential platform for larger-scale gene expression studies compared to the traditional smFISH protocol that takes longer by 1 order of magnitude.

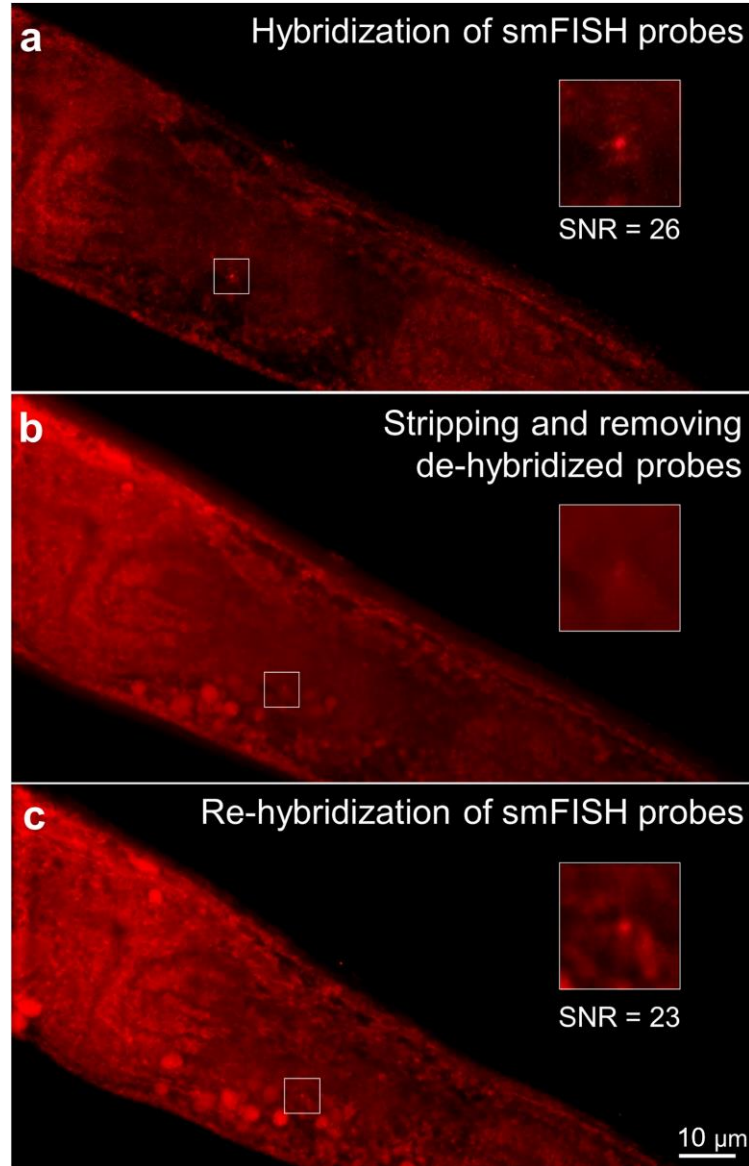


**Figure 3.6 Multi-cycle smFISH of *gpa-3* within the same worm using ICP-enhanced smFISH.** (a) Individual puncta were resolved after initial hybridization. (b) After DNase I treatment for 4 hours, probes were dehybridized and removed by ICP-based ion pump. (c) The same puncta were resolved again after re-hybridization enhanced by ICP. Insets show magnified area at the vicinity of the target mRNA molecule.

Next, we aimed to engineer our platform to enable multi-cycle smFISH to directly address the gene-throughput limitation (*i.e.*, number of resolvable fluorophores). By demonstrating multiple rounds of smFISH, we can provide a new protocol to examine more genes per animal. In this example, we probed for *gpa-3*, removed the probe using a DNase I stripping reagent, and re-probed *gpa-3* in the same single animals. Using traditional smFISH off-chip strategies, we incubated animals in the same DNase I stripping reagent, but we were unable to successfully strip the puncta (Appendix B.2.1). This suggests that diffusion alone may not be sufficient to transport DNase I into the animals' dense tissues. In contrast, we achieved multi-cycle smFISH on-chip. First, we probed for *gpa-3* using the ICP-enhanced delivery, and we were able to visualize puncta as expected, shown by a representative sample (Fig. 3.6a). Next, we delivered DNase I to strip the hybridized probes for 4 hours. Using depletion-assisted isotachophoresis, we removed both the DNase I and stripped probes (Fig. 3.6b). We then re-probed for *gpa-3* in the same sample and found its expression location and SNR are similar to the initial hybridization (Fig. 3.6c, Appendix B.2.2). The quality of the signal (SNR) was not compromised during the multi-cycle smFISH assay across all samples we tested (Appendix B.2.2). If the stripping reagent were still present in the system, the re-added probes would not be able to hybridize to the target mRNA molecules. Thus, this experiment demonstrated that we can efficiently deliver and remove both the probes and stripping reagents to perform multi-cycle smFISH.

### 3.5 Results and Discussion for the Formamide-based Approach to Multi-cycle smFISH

#### smFISH

#### 3.5.1 Validation of flow- and formamide-based stripping for multi-cycle smFISH

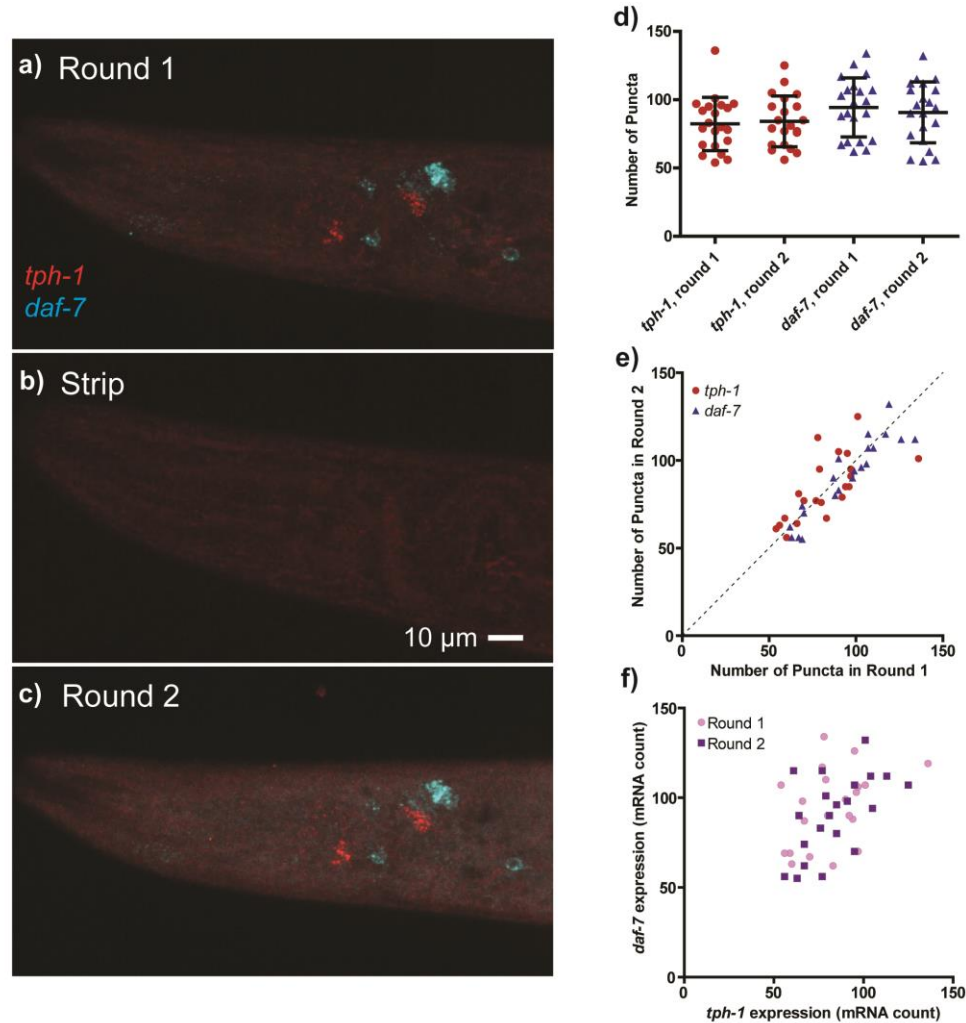


**Figure 3.7 Demonstration and validation of multicycle smFISH using two color imaging channels.** (a) smFISH on-chip protocol was used to quantify *tph-1* in red and *daf-7* in cyan. (b) Formamide-based stripping successfully washed away bound probes. (c) Re-probing the same sample resulted in similar quality of smFISH as Round 1. (d) Number of puncta between the rounds and genes were not significantly different. A paired, two-tailed T test was performed. (e) Each point is an individual animal and its gene quantification from the 2 rounds. Dotted line indicates a perfect relationship. (f) Each point is an individual animal and its expression for both genes. Images are maximum projections.

The previously described approach using the electrokinetic/microfluidic hybrid device (**Section 3.4**) allowed us to efficiently transport large, charged macromolecules and achieve smFISH an order of magnitude faster. However, due to the combination of relying on a harsh reagent (DNase I) and subjecting the samples to electric fields, there was qualitatively noticeable tissue degradation across the cycles (Fig. 3.6). Specifically, we hypothesize that the DNA and other structural elements within the cells and tissues were degraded, resulting in flattened cells which appear as large red blobs. Nonspecifically bound probes contributed to the elevated background fluorescence.

Although the transport is not as fast or efficient, this convection-based microfluidic approach that uses formamide-based stripping buffer to strip the smFISH probes could address these issues (Fig. 3.7). Formamide's stripping mechanism is gentler as it is based on increasing the stringency of the smFISH probes<sup>66</sup> and lowering the melting temperature of double-stranded species. In contrast, DNase I<sup>82</sup> enzymatically digests single- and double-stranded DNA by hydrolyzing phosphodiester bonds. The transport requirements of formamide are also less stringent as formamide is ~3 orders of magnitude smaller than DNase I, thus delivering the needed concentration of reagent may be more feasible.

To adapt the formamide-based stripping approach, I used a microfluidic chamber array described in previous literature from our lab that I worked with.<sup>78</sup> To validate this approach, I performed 2 cycles of smFISH on the same sample for the same genes, *tph-1* and *daf-7* using the microfluidic device. We chose these two neuronally-expressed genes as their spatial expression information has been previously quantified and well-documented;<sup>9,71,93-95</sup> this ensured that the probes were binding specifically to the transcripts at their known locations. By quantifying the number of puncta and quality of smFISH, we



could determine if our stripping and re-probing protocol is effective and validate that our protocol does not bias the biological samples. For example, if the stripping step damages the mRNA or if the re-probing protocol was not successful, we would expect lower or different mRNA counts in the second round. Further, I quantified the signal minus the background and signal-to-background ratios of these images (Appendix B.3.1). It is important to note that the signal-to-background ratio decreases in the second round. The two rounds here were successfully quantified, but it is possible that multiple rounds could lead to more difficulty in distinguishing the smFISH puncta from the background of the sample. In this thesis, I focused on creating the initial steps to address the gene-throughput limitations in traditional smFISH by optimizing two rounds of smFISH. Future studies may require quantifying more genes to answer other biological questions, and the data (Appendix B.3.1) suggests that one to two additional rounds of smFISH should be possible if the signal-to-background ratio decreases linearly. However, importantly, this requires further investigation and perhaps protocol optimization.

Here, I first followed the same protocol introduced in Chapter 2 to perform smFISH on young adult *C. elegans* in the microfluidic device. I probed for two genes each round (Fig. 3.7a). Our setup allows for a total of 3 colors (*e.g.*, red, green, and far-red), but I chose to exclude green due to the samples' high autofluorescence in that channel. Following the first round, I stripped the signal using a 60% formamide solution (Fig. 3.7b) and successfully re-probed the same sample (Fig. 3.7c). Qualitatively, this method was robust as the tissues remain well-preserved and the quality of smFISH was similar between the two rounds. Further quantification supports this; between the two rounds, there were no statistically significant differences between the number of puncta (*i.e.*, amount of mRNA

expression quantified), indicating the quality of mRNA is maintained between the two rounds (Fig. 3.7d). Importantly, the locations of mRNA molecules remain the same between the two rounds as well, supporting the notion that fixation of the samples retain mRNA locations even after stripping the probes.

Further, I show that we can analyze this information on a single animal basis. In Figure 3.7e, each point represents a single animal and its gene expression in the two rounds, and the dotted line indicates a perfect match between the rounds where the counts would be exactly the same. It is expected that there could be some variation due to changes in the orientation of the animals and slight differences between imaging sessions. Indeed, we see that most of the data points lie near the dotted line, and importantly, there is no significant bias towards one direction (*i.e.*, one round was not significantly greater than the other).

In addition, this pipeline was also created to study gene-gene relationships. In Figure 3.7f, each point represents a single animal and its expressions of *tph-1* and *daf-7*. I validated that the expression relationships are maintained between smFISH rounds ( $R = 0.4$  and  $0.5$  for rounds 1 and 2, respectively). In summary, this experiment validates our multi-cycle approach for 2 rounds of smFISH on the same sample (*i.e.*, worm). By demonstrating that this protocol is effective, we can study deeper questions in biology that require quantifying a greater number of genes beyond the gene-throughput limitations of traditional methods.

### 3.5.2 Experimental design to investigate the effects of an environmental perturbation on gene expression

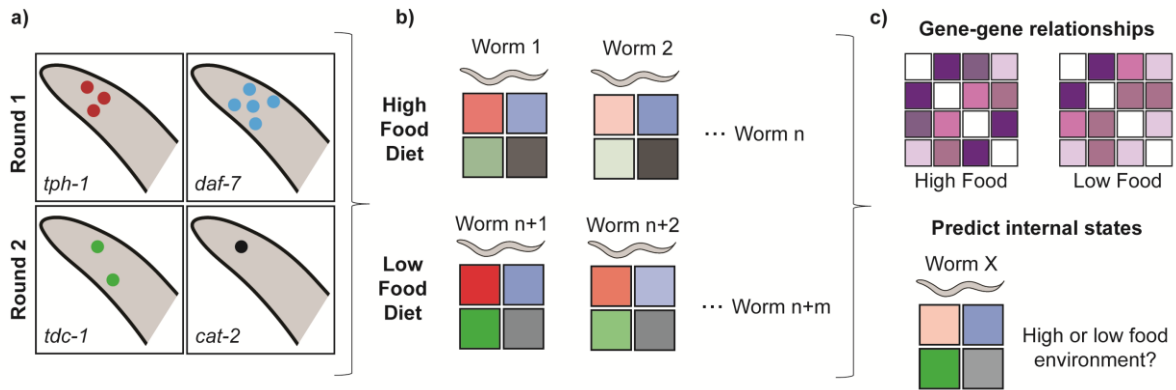


**Figure 3.8 Experimental design to study how diet influences gene expression.** (a) The first round of smFISH will probe for *tph-1* and *daf-7*; the second round will probe for *tdc-1* and *cat-2*. (b) After exposing the animals to high or low food diet, we quantify these 4 genes per animal. (c) With this data, we can investigate how diet may influence gene-gene relationships as well as further analyses such as predicting the internal state of the animal based on its gene expression profile.

This platform enabled us to quantify a panel of genes with high detail through multi-cycle smFISH (Fig. 3.8a). To demonstrate the utility of this pipeline, I investigated how an environmental perturbation, specifically the food levels on which the animals are grown, influenced the gene expression profiles. I grew populations of *C. elegans* on low food (OD<sub>600</sub> 1) and high food (OD<sub>600</sub> 10) to young adults (Day 0 adults) – see 3.3 Materials and Methods for more details. Following the cultivation, I performed 2 rounds of smFISH using the protocol described in the previous **Section 3.5.1**. For the first round, the samples were probed and imaged for *tph-1* and *daf-7*; in the second round, the samples were probed for *tdc-1* and *cat-2* (Fig. 3.8b). We selected these genes as they encompass a large set of environment-sensing pathways and involve all four biogenic amine neurotransmitters (serotonin, tyramine, octopamine, and dopamine) and transforming growth factor beta (TGFβ) in *C. elegans*.<sup>96</sup>

*tph-1* encodes tryptophan hydroxylase, the rate limiting enzyme for serotonin synthesis.<sup>94</sup> *daf-7* encodes a TGF $\beta$  family member.<sup>95</sup> The relationship between these two genes across different food levels have been previously investigated.<sup>9,97</sup> *tdc-1* encodes an enzyme needed to synthesize tyramine and octopamine,<sup>98</sup> and *cat-2* encodes a tyrosine hydroxylase, the rate limiting enzyme for synthesizing dopamine.<sup>99</sup> If we are able to measure all 4 genes on a single sample, we can investigate how this particular environmental stimulus might impact these pathways differently. Further, since this approach would provide single-animal level data, it is possible study gene-gene relationships and quantify how these relationships may change under different food levels. This dataset might allow for further analyses such as using an animal's gene expression profiles to predict its internal feeding states or other biological applications (Fig. 3.8c).

### 3.5.3 Quantifying changes of gene expression resulting from different food level diets

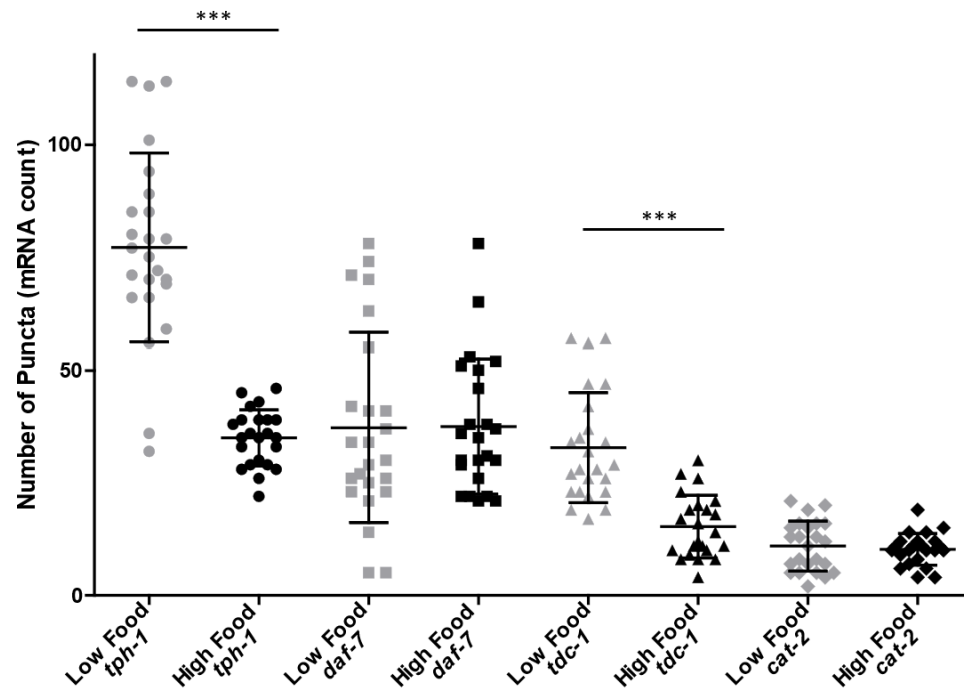


**Figure 3.9 Food levels influence gene expression profiles.** Quantification of gene expression profiles of animals grown on low and high food conditions. The external stimuli (food), influences *tph-1* and *tdc-1* levels significantly. Unpaired, two-tailed T test was performed (\*\*\* $P < 0.01$ ).

This platform enabled the quantification of 4 genes per individual by performing the two rounds of smFISH (Fig. 3.9). By comparing the gene expression profiles of two environmental conditions, low and high food, we are able to understand how these food levels may influence the different pathways in varying degrees. In this case, the data suggests that *tph-1* and *tdc-1* are more influenced by food levels under this particular experimental design; in contrast, *daf-7* and *cat-2* remain at relatively stable expression levels (Fig 3.9). This indicates that the serotonin and dopamine pathways may respond to food levels more dramatically than the other pathways, perhaps suggesting that they are more relevant pathways to food sensing. Even further, since these genes are expressed in

known neurons, it is possible to quantify gene expression with neuron specificity (Appendix B.3.2). It is important to note that growing animals on different food levels might also lead to different aging trajectories as well.<sup>2,3</sup> Thus, the differences in gene expression may reflect not only the responses to different environmental stimuli but also account for differences in developmental age states (*i.e.*, animals fed on the low food diet may be aging slower). This proof-of-concept demonstration is aimed to illustrate that this quantification pipeline can enable us to measure multiple gene expressions and discern differences such as these between the populations.

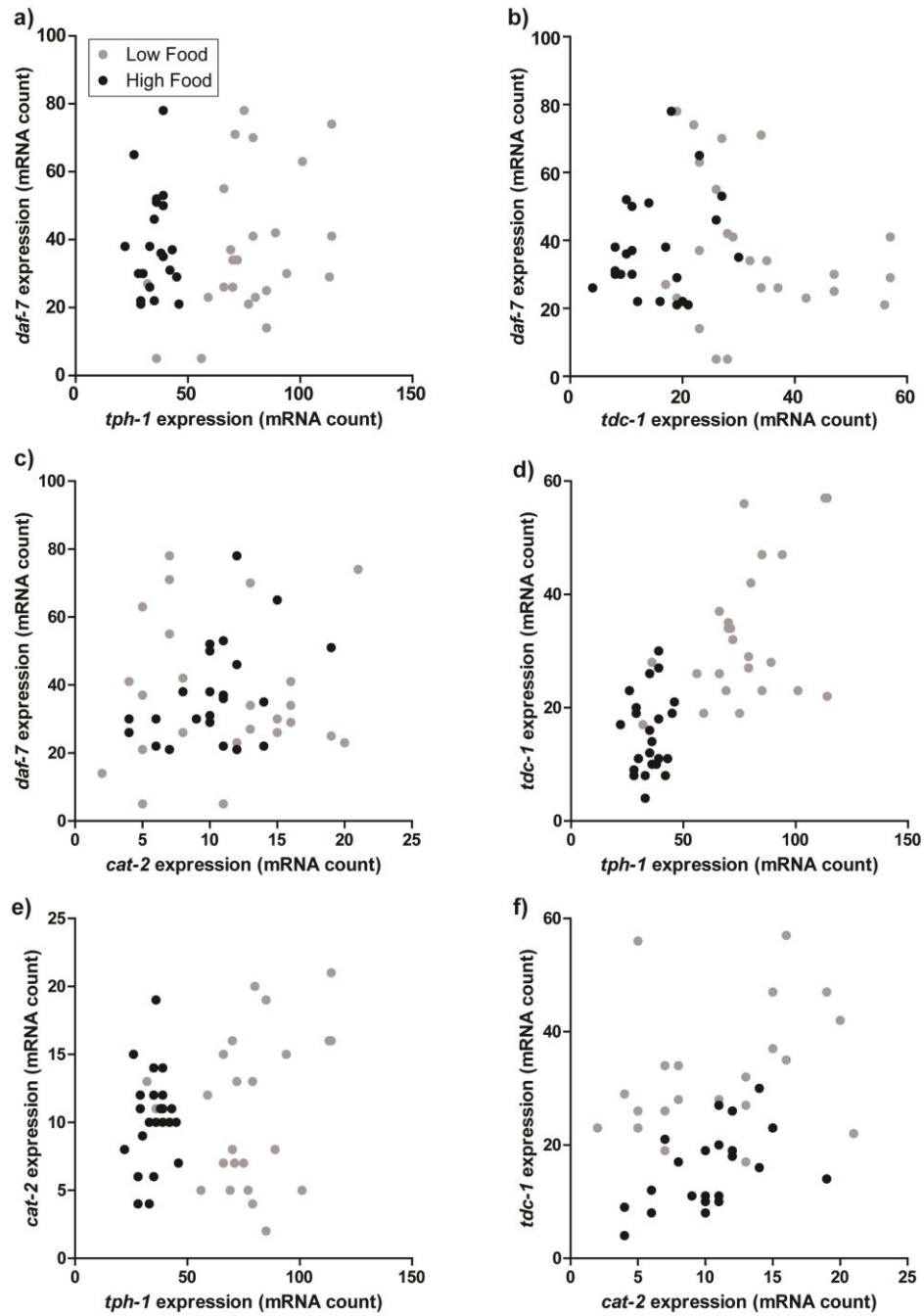


**Figure 3.10 Quantifying gene-gene relationships across different food levels.** Measuring 4 genes per animal allow us to measure 6 different gene-gene relationships: (a) *daf-7* and *tph-1*, (b) *daf-7* and *tdc-1*, (c) *daf-7* and *cat-2*, (d) *tdc-1* and *tph-1*, (e) *cat-2* and *tph-1*, and (f) *tdc-1* and *cat-2*. Each relationship has scaled axis. Each point represents a single animal and its expression levels.

Since our platform allows us to measure these 4 genes with individual-animal resolution, it is possible to investigate gene-gene relationships. In this approach specifically, I could quantify 6 different gene-gene relationships (Fig. 3.10): (a) *daf-7* and *tph-1*, (b) *daf-7* and *tdc-1*, (c) *daf-7* and *cat-2*, (d) *tdc-1* and *tph-1*, (e) *cat-2* and *tph-1*, and (f) *tdc-1* and *cat-2*. Further, since the animals were fed on different food levels, we could measure how diet influences these relationships. Perhaps most easily appreciable, relationships involving *tph-1* and *tdc-1* are strongly influenced by different food levels (Fig. 3.10a,b,d,e). This was expected as *tph-1* and *tdc-1* gene expressions are more individually influenced by food levels as well (Fig. 3.9). In Figure 3.10a, for example, the animals grown on low food levels have a positive *daf-7* and *tph-1* relationship ( $R = 0.4$ ). In contrast, the animals grown on high food levels have a tighter spread and overall lower *tph-1* expression, leading to no correlation between *daf-7* and *tph-1* ( $R = 0$ ).

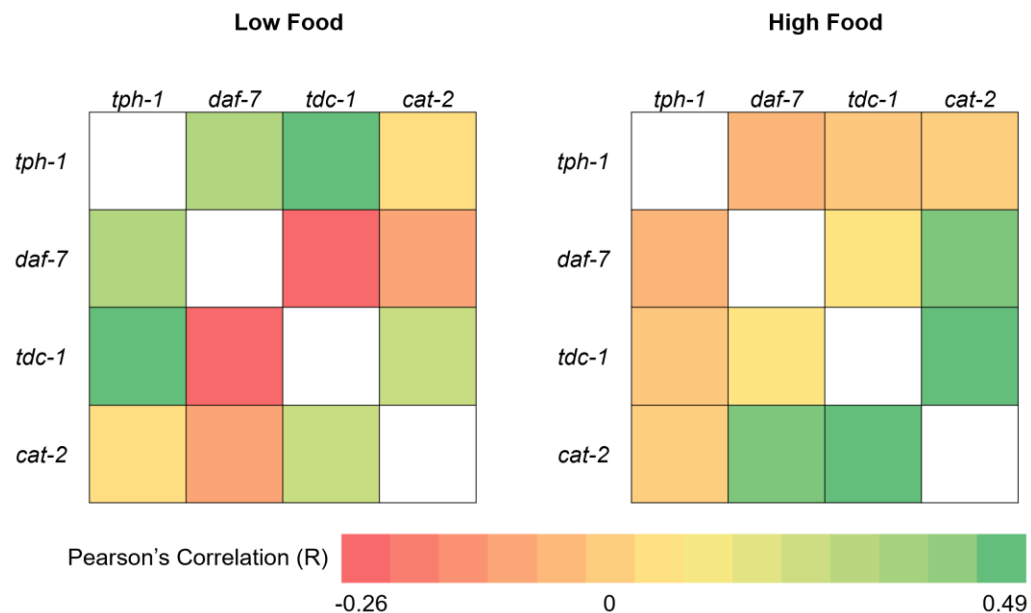


**Figure 3.11 Heat map visualization of gene-gene relationships.** Each square represents the value of the Pearson's Correlation (R) between two genes in each of the food conditions.



To visualize the relationships between the 4 genes more easily, we can also represent the same data as a heat map and simplify the relationships using Pearson's Correlation (R) (Fig. 3.11). There are notable differences between the two food level conditions. For example, the dynamic range of the correlation coefficient values (R) are much larger in the low food conditions. In contrast, the relationships in the high food condition remain relatively positive and stable across the genes but fewer strong correlations. A possible interpretation is that low food levels result in stronger gene-gene relationships (both positive and negative). In contrast, the relationships in the high food level condition are mostly neutral (close to  $R = 0$ ) or positive. This may suggest that higher food levels perturb the animal more globally, influencing the expression of all the genes in a more uniform manner. It may be possible that the presence of food triggers some upstream mechanism to maintain each of the pathways at a relatively stable expression; in contrast, the absence of food may cause certain pathways to become more sensitive to aid the animal to find sources of food. This difference is particularly noticeable in the relationship between *daf-7* and *tdc-1*. It has a negative relationship ( $R = -0.26$ ) in low food where *daf-7* and *tdc-1* have relatively similar expression levels (Fig 3.8). However, in the high food condition, *daf-7* levels remain at the same level while *tdc-1* decreases in expression, resulting in a positive relationship ( $R = 0.22$ ). Since *tph-1* and *tdc-1* gene expressions are more influenced by this food-level environmental perturbation, relationships involving those genes change more dramatically between food levels.

### 3.6 Conclusions

Techniques to study gene expression patterns in aging are limited. Fluorescent transcriptional reporters and traditional smFISH are both restricted to the number of

fluorophores a microscope setup can resolve (typically 2-3). To address this shortcoming, our new platforms discussed in this chapter are able to assay a panel of biomarker genes through achieving multi-cycle smFISH. The first technique is based on an electrokinetics/microfluidics hybrid device, and the second approach is based on using formamide as the stripping reagent in a more traditional microfluidic device.

In the first work, we engineered a microfluidic/electrokinetic hybrid platform to fluidically isolate whole organisms and efficiently manipulate macromolecule delivery in and out of the animals with controlled spatial and temporal resolution using an ICP-based ion pump. This unique approach has broad applications for many biological investigations. Here, we demonstrated its ability to enhance smFISH and enable smFISH multiplexing strategies. Using this device with an optimized protocol, we were able to perform smFISH in whole *C. elegans* on a much faster timescale at only 4 hours. With the capability of removing charged molecules on-demand, we also demonstrated that our platform is suitable to perform multiplexing strategies, which is difficult to achieve with traditional smFISH methods relying on DNase I stripping buffers. This platform provided a tool for us to study large-scale gene expression within individual animals. However, one notable limitation for this work is the degradation of tissue integrity over multiple cycles. Along with subjecting the animals to an electric field, this method relies on a harsh reagent, DNase I, which enzymatically cleaves phosphodiester linkages and damages DNA.

To address these limitations, I simultaneously developed an approach based on the stripping reagent, formamide. Formamide increases the stringency of annealing and can strip the smFISH probes from the mRNA. Along with a gentler mechanism of stripping the smFISH probes, formamide is ~3 orders of magnitude smaller than DNase I, which allows

for easier transport that can be achieved using traditional microfluidics. This work demonstrated and validated a new microfluidic-based platform to perform multiple cycles of smFISH on the same animals with inter-individual information. While slower and more reagent-limited than the electrokinetics/microfluidics hybrid approach, this alternative may be more accessible to others as it does not require an external sourcemeter, and importantly, we saw the tissue integrity remain well preserved. Along with validating 2 rounds of smFISH, I was also able to demonstrate the robust utility of this device. Using different food levels as an example of an environmental perturbation, I measured a panel of genes corresponding to different pathways and discerned which genetic pathways may be more food sensitive. This platform also enabled me to measure gene-gene relationships between 4 genes and compare how their interactions change based on the food levels the animals were exposed to.

Ultimately, this work served as a demonstration of multi-cycle smFISH to directly address the gene throughput limitations in traditional fluorescence imaging-based approaches. Along with establishing two complementary pipelines, we described how these platforms can be used to ask deeper questions in biology. We envision that the level of single-animal information we can collect from these methods will enable us to understand complex physiological systems rooted in gene expression, such as processes ranging from learning to development to aging.

# **CHAPTER 4. MICROFLUIDIC APPROACH TO CORRELATE *C. ELEGANS* NEURONAL FUNCTIONAL AGING AND UNDERLYING CHANGES OF GENE EXPRESSION IN MECHANOSENSATION**

This chapter is adapted from an upcoming publication done in collaboration with another graduate student, Jimmy Ding. Here, I aim to highlight my contributions and detail others' work briefly when needed.

## **4.1 Introduction**

The aging process has broad physiological impacts, including a significant decline in sensory function, which threatens both physical health and quality of life. One ideal model to study aging, neuronal function, and gene expression is the nematode *C. elegans*, which has a short lifespan and relatively simple, thoroughly mapped nervous system and genome. Previous works have identified that mechanosensory neuronal structure changes with age, but importantly, the actual age-related changes in the function and health of neurons, as well as the underlying genetic mechanisms responsible for these declines, are unclear. While advanced techniques such as scRNA-seq have been developed to quantify gene expression, it is difficult to relate this information to functional changes in aging due to a lack of tools available. To address these limitations, we present a platform capable of measuring both physiological function and its associated gene expression throughout the aging process in individuals. Using our pipeline, we specifically investigate the age-related changes in function of the mechanosensing ALM neuron in *C. elegans*, as well as relevant

gene expression patterns of *mec-4* and *mec-10*. Using our platform, we found an initial enhancement followed by a decline in neuronal function through aging and saw that this trend is similar to that in gene expression patterns. Our data demonstrate that our strategy is useful for identifying genetic factors involved in the decline in neuronal health. We envision that this framework could be applied to other systems as a useful tool for discovering new biology.

## 4.2 Background

Age-related declines in sensorimotor control are one of the most prominent hallmarks of aging.<sup>100-102</sup> In humans, progressive hearing loss, impaired balance, and an increase in falls have been shown to be age-related and pose major health concerns for the elderly population.<sup>103-106</sup> There are treatments and strategies to address many of these aging-related symptoms, but the underlying reasons for the decline in sensorimotor control remain unclear. This is perhaps due to the large number of factors contributing to the aging-dependent phenotypes and thus, a lack of comprehensive tools to study and quantify functional aging (*i.e.*, how functions, such as a neuron's ability to sense environmental cues, change with age). It is difficult to characterize aging because, unlike many other diseases, it cannot be traced to a single factor.

Due to the complexity and difficulty of conducting lifelong human studies, researchers often turn towards more well-defined model organisms such as mice, flies, yeast, and *C. elegans*. *C. elegans*, a microscopic roundworm, is an ideal model for aging research due to their short natural lifespan (~3 weeks), self-fertilization for easy culturing of large, isogenic populations, large genetic homology to humans, including especially

well-conserved aging pathways,<sup>3,6</sup> and a well-established genetic toolbox for gene expression-based studies. *C. elegans* are simultaneously a useful model for studying neurological function due to their simple and compact nervous system, well-defined physiology on molecular and functional levels,<sup>107,108</sup> fully mapped connectome,<sup>109,110</sup> and well-characterized behaviors.<sup>111,112</sup> Since these roundworms are optically transparent, they are also easily adaptable for high-throughput *in vivo* and *in situ* fluorescent imaging-based assays.<sup>23</sup> For example, several microfluidic platforms have been developed for *C. elegans* to image,<sup>67,113,114</sup> screen and sort individuals,<sup>113,115</sup> deliver reagents more efficiently,<sup>65,77</sup> study complex behaviors,<sup>116-119</sup> and perform long-term animal culture with single-animal resolution.<sup>78</sup>

While traditional methods have established our basic understanding of sensorimotor control, the approaches are limited as they either rely on indirect methods to suggest functional responses or require manual manipulation and expertise. For example, the classical mechanosensation assay involves manual delivery of mechanical stimulus with an eyebrow hair or metal pick and visual scoring of the behavior (*i.e.*, how the animal responds).<sup>120,121</sup> While it enabled important findings, this assay requires expertise and can vary between experimenters, both in the application of the stimulus and the scoring. A complimentary approach to measuring these behavioral responses is using fluorescence imaging to investigate the physical neuronal health.

For example, fluorescence imaging of transgenic strains of *C. elegans* allows researchers to visualize and quantify how touch receptor neurons – the most upstream component of the sensorimotor pathway – accumulate physical defects with age.<sup>100,122,123</sup> By measuring these trends across different genetic backgrounds, researchers also found

that gene expression and regulation of specific genes are essential to neuronal health.<sup>124</sup> For example, loss-of-function mutations in *mec-4* and *mec-10*, two genes that encode a protein complex that forms the transmembrane channel essential for mechanotransduction, result in an acceleration of age-dependent physical defects in neurons.<sup>100</sup> While these morphological changes, such as blebbing and branching of neurites, may suggest declines in function, they are only a proxy and require further, direct investigation to confirm whether function is actually affected.

To quantify neuronal cellular functional output, the most commonly used technique is patch-clamp electrophysiology.<sup>125,126</sup> While this technique allows for the highest precision, such as recording single channel currents, it requires dissection of an animal and expertise in locating a specific neuron of interest.<sup>127</sup> This limits the experimental throughput, does not allow for recovery of the animal for further experimentation, and both the gluing process and dissection are likely to alter the neuronal or circuit response and add to experimental variability.

To address these shortcomings, microfluidics devices designed specifically to deliver mechanical stimuli and measure the *in vivo* calcium response of *C. elegans*, using the genetically encoded calcium indicator GCaMP, have been developed to quantify mechanosensation.<sup>128,129</sup> These devices reduce the amount of manual labor needed and improve the consistency of the assay by delivering well-controlled mechanical stimuli using deformable polydimethylsiloxane (PDMS) membranes. In addition, these devices can deliver stimuli with different magnitudes, durations, and frequencies.<sup>128-130</sup> While these devices are foundational to improving mechanosensation assays, importantly, these findings do not demonstrate whether differences in calcium responses can attributed to

neuronal health or function (*i.e.*, a larger response may not necessarily indicate healthier function of a neuron). Additionally, these devices were designed for specific sizes of animals and do not extend their applications beyond measuring a single time point; thus, they cannot measure functional aging as they have not been developed for populations of different ages. To be able to attribute measured differences in function to age and not experimental variability, it is essential to keep the stimulus constant between age groups and individuals. This poses another significant challenge as the animals' size and other physical properties, such as cuticle thickness and elasticity, change with age.<sup>131,132</sup>

In this work, we aim to build upon previous designs and further improve these assays to quantify functional aging by adapting the microfluidic stimulus-delivery strategy to different aged animals and linking functional changes to gene expression patterns with single-animal precision. Using a computational model, we first design a microfluidic-based strategy to deliver a consistent, high-frequency gentle touch stimulus to animals sampled at different ages. Next, to ensure our platform can measure the subtle changes of functional aging *in vivo*, we validated our ability to quantify declines in neuronal function with a mock drug perturbation study. We then apply this microfluidic pipeline to measure the changes in aging. Together, our platform enabled us to correlate age-related changes in functional responses and gene expression with single-animal sub-cellular resolution. This work created a new opportunity to quantify neuron function with age and possibly link the change in function to an underlying genetic reason. This microfluidic-based strategy allowed easy manipulation and observation of a microscopic biological system during multiple points of its lifespan. This same framework can be applied to examine other types of functional aging, such as changes in behavior, the genetic and cellular mechanisms that



are necessary to maintain proper physiological integrity with age and may identify therapeutic targets to attenuate the negative impacts of the aging process.

### 4.3 Materials and Methods

#### 4.3.1 *C. elegans* strains

The *C. elegans* strains used in this work were GT372 (aSi31[lox2272 Cbr-unc-119(+) lox2272 + pmec-7::GCaMP7F::ras-2CAAX::SL2::mScarlet-I::ras-2CAAX] II; unc-119(ed3) III) and GT379 (aEx48[*pmec-4::mec-4::mNeonGreen* + *pmec-10::mec-10::mScarlet-I* + Cbr-unc-119(+)]; *unc-119*(ed3)). The promoters were PCR amplified from N2 genomic DNA using NEB Q5 High-Fidelity 2x Master Mix, and assemblies were verified by restriction enzyme digest prior to microinjection.

For the GCaMP calcium reporter strain GT372, the construction of this strain was done by another member of our lab following a MosSCI protocol for transgene integration.<sup>62</sup> For the MEC4::mNeonGreen and MEC10::mScarlet-I reporter strain GT379, I created plasmids of *pmec-4::mec-4::mNeonGreen* and *pmec-10::mec-10::mScarlet-I* were following previously published methods.<sup>133,134</sup> Briefly, *pmec-4::mec-4::mScarlet-I*, *pmec-10::mec-10::mNeonGreen*, and a positive selection marker that rescues *unc-119* were co-injected at 50 ng/μL into QL74 (*unc-119*(ed3) *ttTi5605mos*). Following injections, animals with rescued *unc-119* (i.e., animals with rescued wild-type movement) were selected and examined under a fluorescence dissecting scope for MEC4::mNeonGreen and MEC10::mScarlet-I expression. Each injected parent animal was propagated separately and only one strain was selected for the experiments in this work. We found that the

extrachromosomal constructs were passed down with high efficiency where all animals imaged had *pmec-4::mec-4::mNeonGreen* and *pmec-10::mec-10::mScarlet-I*.

#### 4.3.2 *C. elegans culture*

The *C. elegans* strains used in this work were GT372 and GT379. Worms were grown following standard protocols on NGM agar plates fed on *E. coli* OP50 lawns and maintained at 20 °C for at least two generations. For aging studies, synchronized L1 larvae of the F2 generation animals were obtained from a 2 hour hatch-off of each strain and grown on NGM agar plates until L4 stage on separate plates. At L4, animals were transferred to NGM plates supplemented with 5  $\mu$ M C22, a compound that interrupts eggshell formation and prevents viable progeny without impacting the development or longevity of adults.<sup>135,136</sup> Animals were transferred every day for the first 5 days of adulthood (when the majority of eggs are laid) and then transferred every other day until day 10 adults on NGM plates with C22.

#### 4.3.3 *Device design and fabrication*

The device design is adapted from a previous work<sup>129</sup> and modified to interrogate different age animals. As *C. elegans* age, they increase in size and then decrease at the end of their life. Since the length of the channel was already long enough to accommodate the animals, we needed to focus on the width. To accommodate for this, we designed several variants of the device with different imaging channel widths ranging from 50-75  $\mu$ m. Day 2 and Day 15 animals fit best in the 50  $\mu$ m wide device, and Day 5 and Day 10 animals fit best in the 60  $\mu$ m wide device.

Microfluidic device fabrication has been previously described in greater detail.<sup>129</sup> Briefly, the master mold of the microfluidic device was fabricated with SU-8 2015 (Microchem), a negative photoresist using standard UV photolithography. Since the worms were not immobilized using drugs or cooling, the animals' head or tail can move in the imaging channel of the microfluidic chip; this movement can blur images. To reduce the movement of the head or tail part of the worms, a three-step vertical tapering of the imaging channel was used. The thickness of the first layer was 20  $\mu\text{m}$ , and the second and third layers were 15  $\mu\text{m}$  for the 50  $\mu\text{m}$  deep imaging channel. The design of the width of the actuated membrane is 150  $\mu\text{m}$ , the distance between the first and second sets of membranes is 200  $\mu\text{m}$ , and the distance between the second and third sets of membranes is 250  $\mu\text{m}$ . All microfluidic master wafers were then treated with tridecafluoro-1,1,2,2-tetrahydrooctyl-1-trichlorosilane vapor (Sigma-Aldrich).

The microfluidic devices were fabricated in polydimethylsiloxane (PDMS, Dow Corning Sylgard 184) by traditional soft lithography. To create the actuated PDMS structure to touch and trap worms, a multi-layer soft lithography process was used. For the bottom flow layer of features, PDMS in a 23:1 ratio between the elastomer and curing agent was deposited via spin coating to create a thin layer. For the top control layer, 10:1 PDMS was directly poured onto a blank master to create a thick and mechanically rigid handle layer. Both layers were then baked at 70 °C for 30 minutes until the control layer was still underbaked and slightly sticky. The layers were manually aligned and additional 10:1 PDMS was poured and cured for several hours.

#### 4.3.4 Computational deformation modelling

The computational deformation modelling was important to this work to validate and ensure the efficiency of our stimulus strategy. This work was led by Jimmy Ding and explained in much greater detail in Appendix C.1. Briefly, The COMSOL stationary solver was used to analyze the effect of varying pressure on the deformation of the stimulus valve membrane. The values for the material properties of the PDMS and *C. elegans*, such as Young's Modulus and density, were taken from several sources and a range of potential PDMS material properties based on a 20% variation in cross-linker ratio and temperature were estimated<sup>137-140</sup>. Using these literature sources, the range of material properties used was estimated as follows:

**Table 4.1. Material properties used in the COMSOL model**

$E_{\text{PDMS High}}$ <sup>138,139</sup>	1.1 MPa
$E_{\text{PDMS Low}}$ <sup>137,138</sup>	.6 MPa
$\rho_{\text{PDMS}}$ <sup>141</sup>	0.965 g/cm <sup>3</sup>
$E_{\text{Cuticle}}$ <sup>131</sup>	1.3 MPa
$\rho_{\text{Cuticle}}$ <sup>132</sup>	1.070 g/cm <sup>3</sup>

#### 4.3.5 Device operation and imaging

All imaging experiments were performed using a Leica DMIRB inverted microscope equipped with a Hamamatsu EM-CCD camera using 100 ms exposure time at 40x (air objective, NA 0.75). A DV2 beamsplitter (Photometrics) with a GFP/RFP filter set was used for simultaneous two-color imaging, and the excitation light was delivered through a projector system.<sup>142</sup> To image, animals were loaded into the microfluidic channel and rested for 90 s to acclimate to any mechanical stimulus to loading and return to an

inactive baseline state. Stimuli were delivered 10 s after recording the baseline activity of neurons using the pneumatically actuated valves on the microfluidic device.

For strain validation and qualitative imaging (Figure 4.1e), we used a spinning disk confocal microscope (PerkinElmer UltraVIEW VoX) equipped with a Hamamatsu FLASH 4 sCMOS camera and a 60x oil immersion objective.

#### 4.3.6 Image processing and analysis

A custom MATLAB script was used to track the neuron and extract the fluorescence intensities for each frame of the video.<sup>129</sup> Fluorescence values were computed by subtracting the background intensity ( $F = I_{G\_ROI} - I_{G\_Back}$ ). GCaMP intensities were measured as the mean pixel intensity of the 100 brightest pixels of a circular region of interest (ROI) of 20-pixel radius. Background intensities were measured as the mean pixel intensity of a ring surrounding the ROI and were subsequently subtracted. Calcium traces were computed as the change in  $F$ , ( $\frac{\Delta F}{F_0} = \frac{F - F_0}{F_0}$ ). Baseline values were computed as the mean of  $F$  prior to stimulus delivery.

All statistical tests and graphs were performed and plotted in GraphPad Prism. For the amiloride drug screen comparison between treated and untreated animals, we used a one-tailed, unpaired t test (Fig. 4.3). When analyzing the differences between peaks with age and gene expression changes (Fig 4.2 and 4.4), we used a Kruskal-Wallis test followed by Dunn's Multiple Comparison Test. To quantify the dynamics of the calcium imaging, one-phase association and one-phase dissociation non-linear curves were fit using GraphPad Prism (Fig. 4.3).

## 4.4 Results and Discussion

### 4.4.1 Integrated microfluidic pipeline to measure neuronal functional aging and gene expression

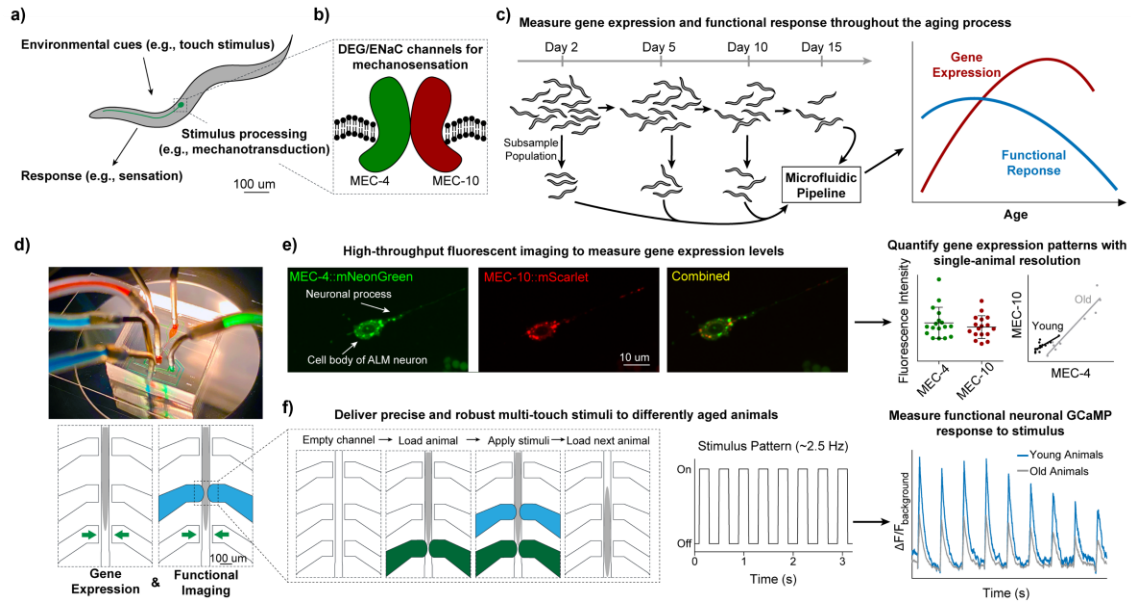


**Figure 4.1 Microfluidic-based approach to correlate age-related changes in gene expression and neuronal function.** (a) Information from the environment is processed within the animal to elicit a response. (b) The DEG/ENaC channels are responsible for mechanosensation in *C. elegans* gentle touch neurons and have a transmembrane complex made of MEC-4 and MEC-10. (c) The populations are subsampled at different ages, and (d) the microfluidic pipeline enables measuring both gene expression and neuronal function to relate the age-related trends. (e) Imaging fluorescent gene reporters enables gene expression quantification with sub-cellular resolution. (f) Delivering precise, robust, high-frequency stimuli to differently aged animals enables measurement of neuronal function.

To deliver precise stimuli to individual animals and quantify their stimulus-evoked calcium response (*i.e.*, functional neuronal activity) and gene expression profiles *in vivo*, we created a semi-automated microfluidic-based pipeline (Fig. 4.1). The degenerin/epithelial sodium channels (DEG/ENaC) are known to be responsible for mechanotransduction in the mechanosensory gentle touch neurons (GTNs) in *C. elegans*

(Fig. 4.1a,b).<sup>143,144</sup> While there are other components to this larger family of genes and proteins, here we focused on MEC-4 and MEC-10 as they form the transmembrane channel essential to the neurons' mechanosensation function (Fig. 4.1b). Further, to characterize the age-dependent neuronal changes, we use the activities and channel-expressions specifically in the ALM touch receptor neuron as a model system for the GTNs.

Previous fluorescence-based studies have established platforms to measure gene expression but relating that information to a biological function is difficult without further investigation.<sup>100</sup> Similarly, studies based on neuronal function are limited as they typically require large perturbations, such as genetic mutations, to measure how gene expression and regulation influence function. For example, null mutations in the DEG/ENaC gene *mec-4* eliminated mechanoreceptor currents in *C. elegans* touch receptor neurons.<sup>126</sup> While this concludes that *mec-4* is essential to mechanotransduction and mechanosensation, these harsh genetic perturbations may lose more subtle details. For example, there may a threshold of *mec-4* expression needed for proper mechanosensation functionality, and a complete knockout of *mec-4* does not allow for this type of analysis. Even worse, genetic manipulations may influence the lifespan of the animal and possibly alter the trajectories of aging.<sup>6,123</sup>

Further understanding the effects of aging on neuronal function requires complex methods and tools designed to correlate function and gene expression in aging populations of animals. We designed a new pipeline to address these limitations (Fig. 4.1c,d). Two populations were aged following standard plate-based protocols and subsampled at different ages. The subsamples were then used in our microfluidic pipeline. Here, one population of calcium-reporting animals was used to quantify neuronal function and the

second population of translational-reporting animals was imaged for gene expression quantification. By measuring each population's aging trends with our platform, we could correlate neuronal function and gene expression in the context of aging, enabling us to ask how age-related changes of gene expression may influence neuronal function. To quantify the expression levels of *mec-4* and *mec-10*, we used our microfluidic platform for high-throughput imaging of fluorescent translational reporters (Fig. 4.1e), a common technique that can provide a proxy readout of the genes' expressions.<sup>133,134,145</sup>

While much of my thesis is based on smFISH to measure spatial gene expression, this work used translational reporters. A limitation of smFISH is requiring sample fixation, thus killing the animal. In contrast, translational reporters allow for long-term live imaging, which may be useful for follow-up aging studies using this platform that require longitudinal tracking of individual animals. In this work, we image single neurons and quantify their expression profiles. This same platform could also serially load individual animals with a genetically encoded calcium indicator (GCaMP), apply a touch stimulus, monitor the functional response of the mechanosensory neuron, and then empty the channel for the next animal (Fig. 4.1f). While single touches could evoke a neuronal response, we found that delivering multiple mechanical stimuli at a high frequency (~2.5 Hz) resulted in a larger, more robust neuronal response.<sup>128</sup> Together, we used this integrated microfluidic pipeline across different ages and measured how the aging process may affect both neuronal function and gene expression in mechanosensation.



#### 4.4.2 *Computational modelling and empirical validation to measure neuronal health in different aged populations of C. elegans*

The computational deformation modelling was important to this work to validate and ensure the efficiency of our stimulus strategy across animals of different ages. This work was led by Jimmy Ding and explained in much greater detail in Appendix C.1 as well as an upcoming publication.

*C. elegans* increase in size appreciably as they age and then decrease during the very end of the lifespan.<sup>146,147</sup> Designing devices for each age of the animal thus required scaling the imaging channel of the device to different widths and heights. While the geometry is important, delivering consistent stimuli with the pneumatic valves across different ages and devices is key to measuring functional aging. This helps ensure that changes detected in neuronal function are indeed due to aging and not due to inconsistent stimulus delivery. For example, if one age group of animals were subjected to gentle touch stimulus and another at a different age group were subjected to harsh touch stimulus, the differences in responses would most likely be due to a combination of both age and stimulus. While not discussed in this dissertation in depth, our computational model and empirical validation demonstrated that regardless of the age of the animal, we could deliver consistent mechanical stimuli to evaluate functional aging.

#### 4.4.3 *Validating the microfluidic-based strategy to evaluate neuronal health*

GCaMP has been used as a proxy for neuronal activity, but its use in measuring function has been typically limited to measuring only whether a neuron is activated or not. This resolution was enough for some broad studies, such as finding which neurons respond

to stimuli of a certain magnitude or applied to a specific region of the animal, but its use as a measurement for neuronal health is not yet well established. In other words, it is unclear whether a larger stimulus-evoked response is due to a healthier neuron. Because we are interested in the graded response, we first wanted to ensure that our platform was capable of quantifying calcium dynamics, and that varying calcium dynamics reflect relevant biological changes, such as those possibly found in the aging process. This experiment is discussed in further detail in an upcoming publication.

To accomplish this, we validated our system in a pseudo drug perturbation application. Briefly, we compared two populations: a control, untreated group and a group treated with 3 mM amiloride. Amiloride specifically inhibits DEG/ENaC channels,<sup>148,149</sup> and when applied to *C. elegans*, we were able to measure its influence on the neuronal response dynamics. By quantifying the peaks of each animal's stimulus-evoked response, we found that the drug treatment, as expected, significantly decreases the neuronal response. Previous studies showed similar trends using the patch-clamping technique,<sup>126,150</sup> reinforcing our demonstration that this calcium-sensitive indicator was similarly capable of measuring *in vivo* neuronal function without requiring dissection of the animal. This indicated that our platform can not only measure whether a neuron responds or not but also the strength and general health of its functional response.

#### 4.4.4 Age-related declines of neuronal function in a mechanosensory neuron

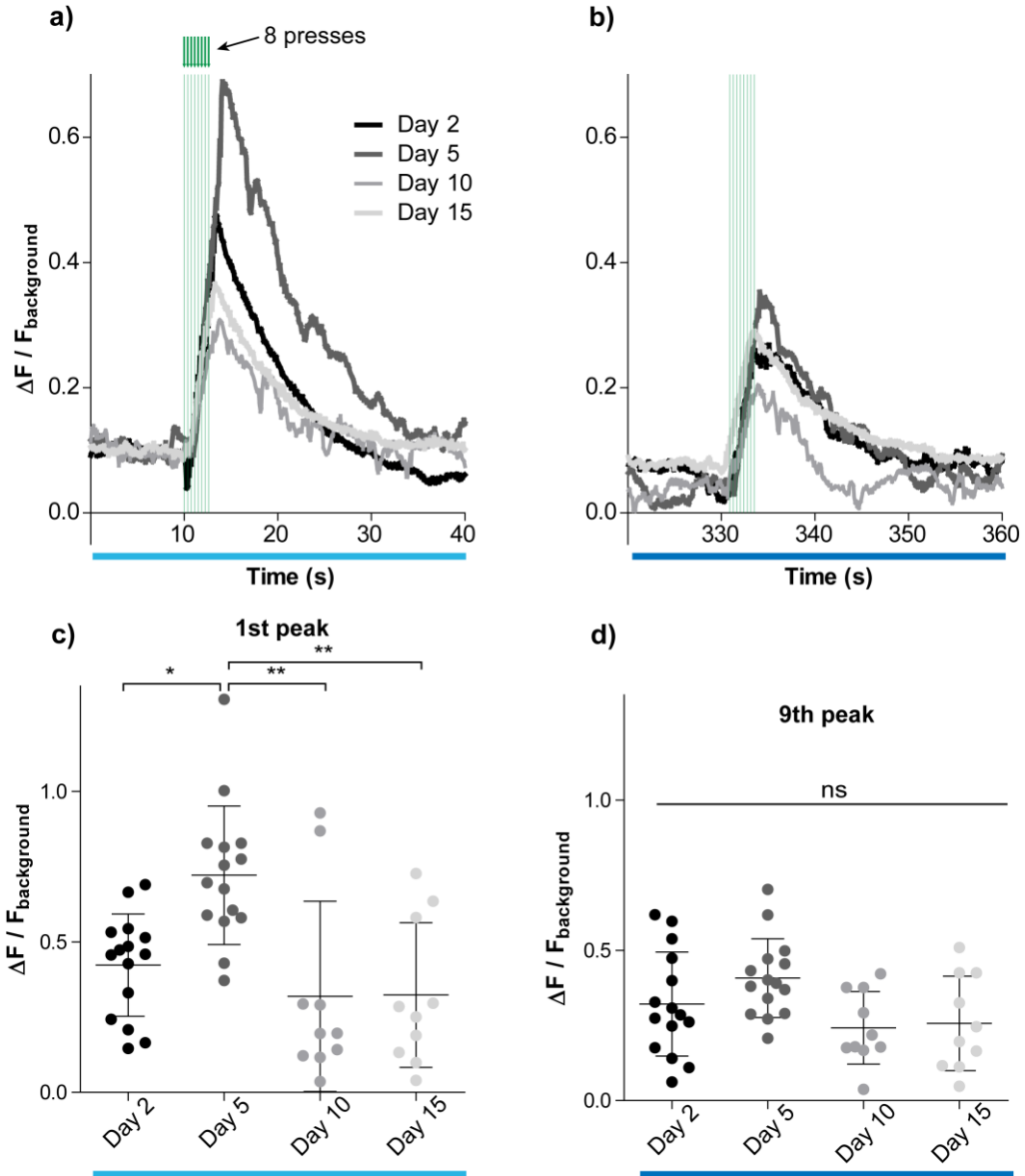


**Figure 4.2. Aging leads to a decline in neuronal function in mechanosensation.** Each animal was loaded into the microfluidic chip, which applied stimulus pulses (8 gentle touch presses at ~2.5 Hz) for 3 seconds followed by a 40 second gap. This was repeated 9 times, followed by a longer 30 second stimulus also delivered at ~2.5 Hz. (a,b) The first and 9<sup>th</sup>, stimulus results enlarged. (c) First peaks from individual animals reveal there is a significant increase in neuronal response from Day 2 to 5, followed by a decrease. (d) 9<sup>th</sup> peaks from individual animals reveal no significant differences. The Kruskal-Wallis test was performed followed by Dunn's multiple comparison test (\* $P < 0.05$ , \*\* $P < 0.01$ ).

We engineered a microfluidic-based functional aging assay to help answer how neuronal health and function were changing with age. In this work, the imaging and processing of the neuronal functional data was done by Jimmy Ding, and the device operation and optimization will be discussed in an upcoming publication. My contributions to this work were on aging the animals and analyzing/interpreting the data. Animals were cultured and sub-sampled at different time points (Days 2, 5, 10, and 15 of adulthood) during the lifespan (~20 days) (Fig. 4.1c). Each sampled group was then loaded into our pipeline to measure gene expression and neuronal activity. Briefly, each animal was loaded into the microfluidic chip, which applied stimulus pulses comprised of 8 gentle touch presses at ~2.5 Hz for 3 seconds with 40 second gaps between each pulse. A single pulse was sufficient to produce a consistent neuronal response, and we extended the stimulus protocol to allow for the measurement of additional features of neuronal function. In total, each animal was stimulated 9 times with this brief pulse (Fig. 4.4). The repeated pulses acted as an assay for habituation, a form of learning that can imply that neuronal plasticity is functioning properly.

Comparing the average neuronal responses of each age group revealed stark differences and trends in aging (Fig. 4.2). The first peak (Fig. 4.2a) demonstrated a stereotypical neuronal response from a single applied stimulus pulse. The overall age-related trend showed an initial increase in max amplitude, suggesting improvement in neuronal function between Day 2 and Day 5 animals, followed by a decline in function at Days 10 and 15. The first peak indicated that the younger animals responded to the initial touch stimulus much more strongly than older animals (Fig. 4.2a,c). This may suggest that younger animals are more responsive and sensitive to mechanical stimulus.

Habituation was also demonstrated, as subsequent peaks from the first stimulus pulse resulted in reduced magnitudes. This was much more appreciable when comparing the differences between the first (Fig. 4.2a,c) and ninth peaks (Fig. 4.2b,d). The difference between peak heights, and thus the presence of habituation, was much more apparent at Days 2 and 5 and insignificant at the older ages. This indicates that the animals' ability to habituate to mechanical stimuli increases and then decreases with age and suggests that younger animals are better at learning and adapting to their environment, possibly due to an enhanced neuronal plasticity compared to the older animals.

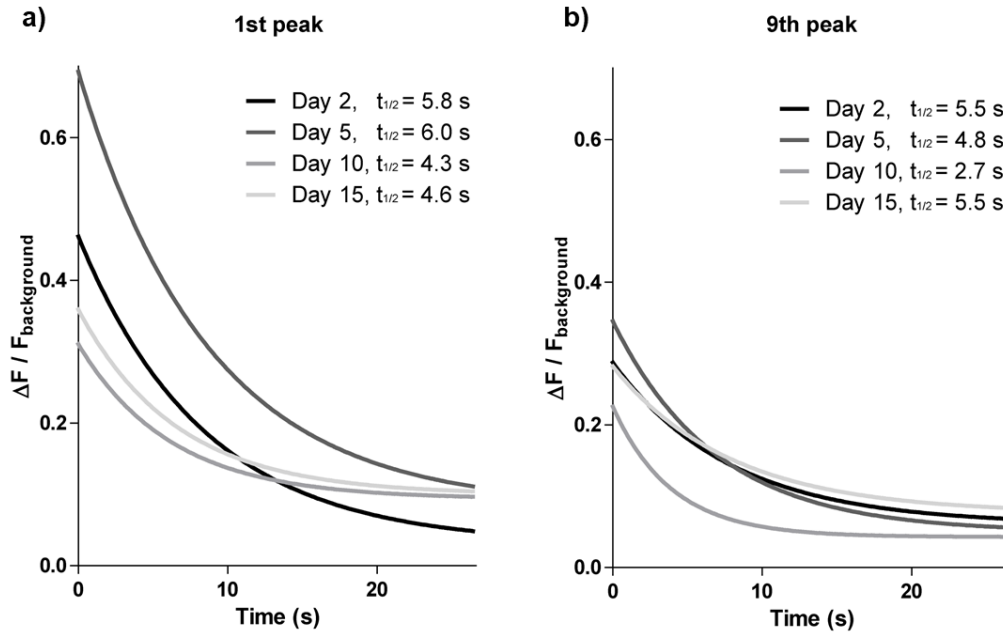


**Figure 4.3. Age-related changes in dynamics of neuronal function.** (a,b) Following the stimulus, there is a recovery period to baseline. To quantify the changes in dynamics, we fit a one-phase decay curve to the data for the (a) first and (b) 9<sup>th</sup> peaks.

Along with the peaks of the neuronal responses, aging also influenced the dynamics (*e.g.*, decay rate) of the neuronal traces (Fig. 4.3). A one-phase decay curve was fit to the data for the (a) first and (b) 9<sup>th</sup> peaks and the half-life ( $t_{1/2}$ ) of decay was calculated for each

age group. From the initial stimulus, younger animals had a slightly longer half-life, indicating it took longer for the animals' calcium levels to return to baseline expression compared to older animals (Fig 4.3a). This is likely due to the differences in initial peak heights. Since younger animals reached a much higher peak in calcium response (Fig. 4.2a, 4.3a), they require more time to return to baseline. However, it may also indicate that older animals have more efficient, established machinery to return calcium levels to baseline levels after a mechanical stimulus. This trend was not seen after the 9<sup>th</sup> stimulus, indicating habituation affects the curves' dynamics (Fig. 4.3b). Here, the half-life of each age group is similar except for Day 10 where the half-life is much shorter. Since all the peak heights after habituation (the 9<sup>th</sup> peak) are quite comparable (Fig. 4.2d), the differences here may be more reflective of the neuronal health in contrast to the first peak (Fig. 4.3a). These results suggest that Day 10 animals are the most efficient at returning to baseline after habituation (Fig. 4.3b). The efficiency of returning to baseline may indicate that the animal is more temporally responsive to future mechanical stimulation.

These results together suggested that aging first leads to an improvement in sensory function followed by a decline in older animals. This is possibly linked to a biological incentive to be most responsive during the reproductive period, which peaks and ends in early adulthood, and a reduced need after this stage of life. Motor neurons follow the same trend in literature;<sup>151</sup> to the best of our knowledge, these aging trends in mechanosensory neurons in general have not yet been reported. It may be possible that there is a more global mechanism regulating functional aging common to multiple neuron types.

#### 4.4.5 Age-related changes of gene expression in *mec-4* and *mec-10*

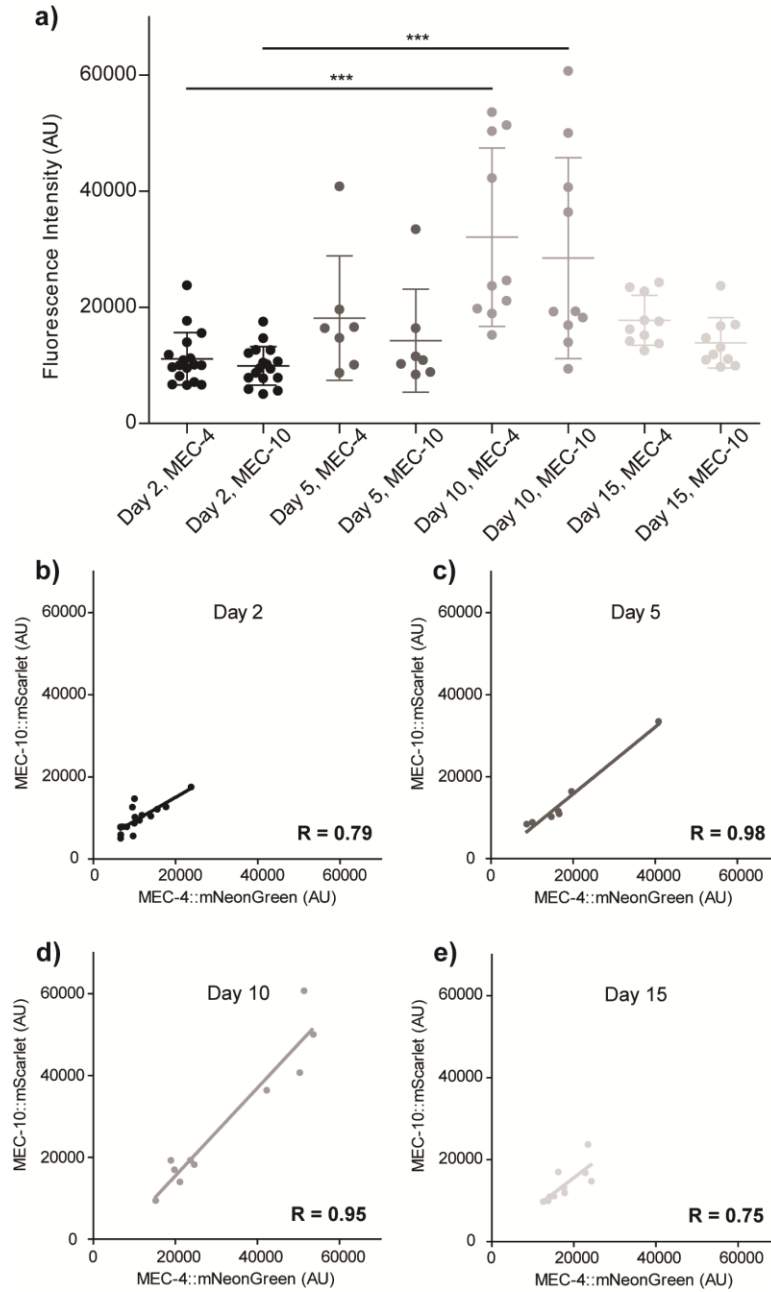


**Figure 4.4. Aging leads to changes in gene expression patterns while regulation is well maintained.** (a) Gene expression patterns across different ages reveals significant increases in MEC-4::mNeonGreen and MEC-10::mScarlet-I expression with age up to Day 10, followed by a decrease at Day 15. (b,c,d,e) With individual-level data, we could examine gene expressions within the same animal across different ages. There is a strong positive correlation between the two genes across the different ages, indicating that the regulation of the genes is well maintained regardless of age.

To correlate the functional output measured (Fig. 4.4) to molecular mechanisms, I next looked to measure gene expression patterns in the context of aging. While the literature concludes that genetic loss-of-function mutations can impair biological function, expressions/maintenance/changes over age of these channels have not been characterized. Our platform, in contrast, enables us to measure gene expression and couple this information to the trends in functional aging to identify how these genetic players (*mec-4* and *mec-10*) may be behind these age-related changes. We imaged fluorescent translational reporters where the fluorescence intensity levels correspond to the gene expression patterns.<sup>145</sup>

Looking at population-level data, there was an increase in expression of both *mec-4* and *mec-10* with age, followed by a decrease at the final time point (Fig. 4.4a). At first it seems that the spread of expressions, and thus variability, increases with age, and this possible dysregulation of gene expression may contribute to the changes in neuronal response. However, since our platform enables single-animal resolution, we are able to inspect expression levels and compare them within individual animals. In Figures 4.4b-e, each point corresponds to a single animal and its *mec-4* and *mec-10* expression levels. The expression levels of the two genes across the different ages indicated a strong positive correlation, perhaps with the tightest correlation at around early-to-mid-life (Fig. 4.4c,d). These results suggested that the regulatory elements and the relationship between *mec-4* and *mec-10* seem to be well-maintained with age. This was expected as MEC-4 and MEC-10 physically form a complex together, suggesting that they may be regulated by similar mechanisms. Surprisingly, we found that the Day 10 increase in both gene expressions was primarily driven by a group of high-expressing animals rather than the whole population



(Fig. 4.4d and Appendix C.2.1). This natural gene expression variability within the population seemed to have impacted both *mec-4* and *mec-10* expression similarly, suggesting that there is a more global/upstream regulator that was influenced possibly by aging. Further, the population of high expressers were not present in the Day 15 group (Fig. 4.4e and Appendix C.2.1), implying that high expressing animals may be more short-lived. This is because at Day 15, a large proportion of the population have already passed away due to natural aging; thus, it may be possible that this time point is biased towards a healthier, long-lived sub-population.

We developed a microfluidic pipeline capable of correlating functional responses and gene expression patterns across different ages. This allowed us to reinforce observed trends in aging and possibly discover new biology. As *mec-4* and *mec-10* expression increased in early life, the mechanosensory neuronal function improved (Fig. 4.2 and 4.4). However, overexpression may lead to early death, as seen by the lack of high expressing animals at Day 15 (Fig. 4.4b and Appendix C.2.1). We propose a potential explanation where steadily increasing channel proteins (*mec-4* and *mec-10*) produces an increase in calcium flow in early-age animals, resulting in healthier neuron function. This is followed by an increase of gene expression beyond a healthy threshold, leading to neuronal functional degradation in Day 10 and 15 animals and suggests that there is an optimal level of *mec-4* and *mec-10* expression. This is further supported in literature as both loss-of-function and gain-of-function mutations in *mec-4* are detrimental to mechanosensory neuronal health,<sup>100,123,144</sup> again suggesting there is an optimal level of expression. Furthermore, even in isogenic populations of *C. elegans* grown on the same conditions, there is animal-to-animal variability in lifespan. Since Day 15 is towards the end of the

lifespan, it is reasonable to assume that perhaps the animals measured here are the longer-lived, and perhaps represent a healthier portion of the population. This would further support the notion that relatively well-controlled, low expression of *mec-4* and *mec-10* contributes to healthier aging and prevents earlier death.

## 4.5 Conclusions

A major bottleneck in aging studies is the lack of tools available to measure both functional aging and its associated underlying molecular mechanisms. While there are platforms to measure function, including those that deliver mechanical stimuli and measure the stimulus-evoked neuronal response, they have not been adapted for aging studies.<sup>128,129</sup> Further, these functional assays generally cannot identify or evaluate which genes are relevant to the function without large genetic perturbations, such as genetic mutations. Similarly, while there have been advancements to measure gene expression in whole animals, such as microfluidic tools for high-throughput fluorescence-based imaging,<sup>9,65,113</sup> it is difficult to tie together gene expression with a meaningful biological function without expansive prior knowledge of the gene's role. Without the development of new, more comprehensive tools, the field is limited to assays measuring either a biological function or gene expression at single timepoints.

This work demonstrates that adapting high-throughput, high-content microfluidic platforms to measure both functional and gene expression data can yield meaningful findings and correlations in aging. This strategy can be easily applied to other platforms. For example, microfluidic-based lifespan platforms have already been developed.<sup>114,136,152</sup> While they were created to study behavior or physical structures, perhaps incorporating

gene expression quantification can further elucidate underlying mechanisms of aging. A well-studied phenotype in *C. elegans*, for example, is a decline in movement with age where young animals move much more than old animals.<sup>117,136,153-155</sup> By measuring how other sensorimotor-related genes change with age, it may be possible to identify which genes need to be maintained to prevent the decline in movement and other healthspan metrics. We created our current pipeline to investigate age-related decline in mechanosensation, and we hope to establish this work as a framework for future functional aging studies.

## CONCLUSIONS AND FUTURE DIRECTIONS

### 4.6 Thesis Contributions

The objective of this thesis was to engineer new microfluidic-based tools that allow for high-throughput gene expression studies with individual- and tissue-specific resolution. Traditional reagents and assays such as fluorescent transcriptional reporters and smFISH have proven to be powerful tools that can enable these types of studies, but they have notable limitations: sample/reagent handling throughput, gene throughput, and relating gene expression to function. Together, the work presented in this thesis address these traditional assay limitations and improve the content of information we can gather on a single-animal level.

In **Chapter 2**, I developed a pipeline to enable single-animal gene expression quantification with sub-cellular resolution by adapting smFISH in adult *C. elegans* using microfluidics. Traditional smFISH requires multiple manual reagent exchanges typically done on a population-level: ~100s-1000s of animals are transferred into a tube, spun down in the centrifuge, and the supernatant is replaced with the next reagent. Along with needing these reagent exchanges that could potentially damage older animal's more fragile tissues, smFISH's use as a gene expression quantification method is not widely used in *C. elegans*, perhaps due to its limitation as an endpoint assay. For example, if there was individual-level information about each animal, such as a phenotypic behavior metric, their identities are lost while performing the smFISH reagent exchanges as all the animals are placed in the same tube together. Along with creating a microfluidic-based pipeline that addresses the sample/reagent handling throughput with semi-automation, this work enables us to

retain inter-individuality. This allowed us to couple live phenotypic information (*daf-7::Venus* expression) and the smFISH-based gene expression (*gpa-3* mRNA counts) to quantify their relationship. This work directly addressed the throughput of sample handling, the limitation of smFISH as an endpoint assay, and related smFISH-based gene expression quantification to live phenotypic information. This platform was a foundation to build upon in Chapters 3 and 4 for both technological advancements and biological investigations.

In **Chapter 3**, I engineered two different approaches to enable multiple cycles of smFISH. Traditional single-animal approaches, such as fluorescent gene reporters and smFISH, rely on fluorescence imaging. Typically, the expression of each gene is quantified using a separate color so the number of genes that can be studied from a single sample is equal to the number of resolvable fluorophores of an imaging setup. For example, typical fluorescence microscopes can resolve 2-3 colors/fluorophores; thus, in a single sample, it is only possible to quantify 2-3 genes. In this work, in contrast, I designed two approaches to perform smFISH on a population of animals (similar to Chapter 2), strip the smFISH probes and signals, and re-probe the same sample. By enabling two rounds of smFISH, we can double the number of genes studied per animal. The first design was done in collaboration with Dr. Gongchen Sun, and it was based on a microfluidic/electrokinetic hybrid device to enable the delivery and removal of large, charged macromolecules. This approach was based on enzymatically cleaving the probes from the mRNA with DNase I. While this technique allowed us to perform smFISH one order of magnitude faster and perform two rounds of smFISH, it can damage the tissues of the animals due to the combination of using a harsh reagent (DNase I) and subjecting the samples to electric

fields. The second approach resolves these issues by using formamide as the stripping buffer in a traditional microfluidic device. Formamide has a gentler mechanism of probe removal and is more easily transported into the samples. While this second approach may be slower than the electrokinetic/hybrid device, it robustly enables two rounds of smFISH while retaining the tissue integrity of the samples. Further, by quantifying 4 environment-sensing genes from 4 distinct pathways, we demonstrated a platform that can determine which pathways are more affected by certain environmental perturbations. In this work, we determined 2 pathways that are perhaps more relevant to food sensing and quantified 6 gene-gene relationships on a per animal basis. This highlights the power and versatility of the approaches to be used for a wide range of biological questions that need high-content information on a panel of genes.

In **Chapter 4**, in collaboration with Jimmy Ding, I developed a platform to measure aging-related changes in neuronal functional strength and gene expression. The aging process has broad physiological impacts, including a significant decline in sensory function, which threatens both physical health and quality of life. Previous works have identified that mechanosensory neuronal structures changes with age, but importantly, the actual related changes in the function/health of neurons, as well as the underlying genetic mechanisms responsible for these declines, are unclear. Advanced techniques, such as scRNA-seq, have been developed to quantify gene expression and the aging process, but it is difficult to relate this information to functional changes due to a lack of tools available. To address these limitations, I created a platform capable of measuring both physiological function and its associated gene expression throughout the aging process in individuals. With a series of devices for animals of different ages, we found an initial enhancement

followed by decline in neuronal function through aging, and this trend is similar to that in gene expression patterns. Together, our data demonstrate that our strategy is useful for identifying genetic factors involved in the decline in neuronal health, and ultimately, this platform and framework could be applied to other systems as a useful tool for discovering new biology.

## 4.7 Future Directions

The work described in this thesis is aimed to create new microfluidic-based tools to address the limitations and shortcomings of traditional gene expression quantification assays including fluorescence-based gene reporters and smFISH. Together, I created four different platforms to improve the content of information we can quantify on a single-animal level. In this section, I discuss a few possible areas of future developments in technological improvements as well as biological applications for these tools.

### 4.7.1 *Coupling behaviors and other phenotypic information with gene expression*

In **Chapter 2**, I detailed a microfluidic-based pipeline to adapt smFISH to adult *C. elegans*. We demonstrated that our device enables single-animal resolution so we can relate live phenotypic information with smFISH-based gene expression measurements. In this example, we imaged a live fluorescent transcriptional reporter for *daf-7* gene expression and then performed smFISH for *gpa-3* gene expression. The live phenotypic data can be extended to other metrics as well, such as behavior.

A potential area of work is adapting smFISH to the Health And Lifespan Testing Hub (HeALTH) developed in our lab.<sup>78</sup> HeALTH is an automated microfluidic-based

platform to monitor long-term behavior and healthspan in *C. elegans* under precise environmental control. Currently, findings from this work are based on measuring how behavioral metrics, such as the speed of movement, or types of behaviors, such as swimming/thrashing and crawling, change with age. Reinforcing the literature, these studies have demonstrated there is correlated individual-to-individual variability in lifespan and behavior. Specifically, the longer-lived proportion of an isogenic population exhibited slower behaviors (*e.g.*, crawling) sooner in their relative lifespans; in contrast, the shorter-lived animals tend to have behavioral declines quite quickly but later in their relative lifespans. It has been suggested that part of this variability is due to gene expression variability between the animals due to natural stochastic processes.

To better quantify this phenomenon, it may be possible to perform the lifespan on the HeALTH platform and then perform smFISH on the same animals. In fact, the formamide-based multicycle smFISH work presented in **Chapter 3** is based on using this same microfluidic device as the HeALTH platform. Further, the HeALTH pipeline has the ability to efficiently culture animals with precise environmental control. By altering factors such as food levels or temperature, we can examine how these environmental perturbations may alter behaviors and gene expressions together. Ultimately, this future work would enable studies that examine and quantify lifespan-long behavior metrics along with the underlying genetic mechanisms perhaps responsible for inter-individual variability with minor modifications to existing platforms.



#### 4.7.2 *Increasing gene-throughput and expanding spatial gene expression*

In **Chapter 3**, I present two different approaches to increase gene throughput. In each of these cases, I demonstrate and validate two rounds of smFISH. From initial studies, it is reasonable to assume that we can extend this protocol to at least 3-5 rounds of smFISH. Qualitatively, the quality of smFISH does not change; however, this needs to be measured quantitatively to ensure that this protocol performs properly without damaging the mRNA. Other multi-cycle smFISH protocols, such as seqFISH<sup>79</sup>, done on thin tissue samples (~10  $\mu\text{m}$  thick) or mounted cells have achieved multiple rounds (>5). Adapting these approaches to larger, whole animals present other challenges such as transporting reagents in and out of dense, heterogeneous tissues, and the pipelines established in this thesis can efficiently deliver reagents. Although validation must be done, it should be possible to achieve more cycles with minor modifications to the protocol. Further, if we are able to maintain the samples' locations more accurately – specifically transcript-level rather than individual-level – with each reagent exchange, we can increase gene-throughput exponentially as  $F^N$  ( $F$  is number of resolvable fluorophores and  $N$  is number of rounds) by using barcoding approaches.

In addition to measuring gene expression, one of the major advantages of smFISH is localizing the expression information with high spatial resolution. The datasets generated from this thesis already incorporate genes with well-defined expression locations (*e.g.*, all genes quantified in Chapter 3 have known expression patterns in defined neurons). This thesis focuses on the tool development, but further analysis of the existing data with tissue specificity may reveal interesting trends in biology. For example, *tph-1* was found to be a strong responder to different food levels (Fig. 3.8), and it is predominantly expressed in

the NSM and ADF neurons. It is possible that not only is *tph-1* more responsive to food levels but also perhaps only one set of the neurons are more responsive as well. Manually quantifying expression levels per neuron in each animal can be time consuming, but there are computational approaches developing both within and outside of our lab to semi-automate the quantification pipeline. By employing these techniques, we can ask deeper questions based on spatial information, such as identifying the neurons more sensitive to food or do expression levels between different pairs of neurons have different correlations.

#### 4.7.3 *Correlating function and gene expression on an individual level*

In **Chapter 4**, I detailed a microfluidic-based pipeline that can image both neuronal health and underlying gene expressions in the context of aging. There are many techniques to measure function, and one powerful tool to measure neuronal function is using GCaMP as a proxy for neuronal activity. In this work, we used two different strains of *C. elegans*. One strain had the GCaMP genetically encoded into the GTNs. The other was a fluorescent translational fusion reporter to measure *mec-4* and *mec-10* gene expression levels, which are genes expressed in GTNs. While we were able to correlate the trends in aging by imaging these two different populations grown in the same conditions, we were not able to capture both neuronal activity and gene expression in the same animal. This is because the GCaMP strain uses both the red and green fluorescence channels (red for reference and green for GCaMP), and the translational fusion strain uses red and green fluorescence channels as well (red for MEC-10::mScarlet and green for MEC-4::mNeonGreen). Here, I present two possible techniques to gather both neuronal activity and gene expression information from the same animal.

One solution is creating a new strain using similar molecular biology techniques described in **Chapter 4**. A potential strategy is creating MEC-4::CyOFP1 and injecting that construct into the existing GCaMP strain. CyOFP1 is a long stokes shift fluorophore (Excitation peak at 497 nm, Emission peak at 589 nm). This fluorophore can be easily imaged without any physical modifications to our imaging setup. It is excited in the same way as GFP and emits as RFP. While this does not allow for the use of quantifying *mec-10* expression, literature suggests that *mec-4* plays a more major role in the biological processes.<sup>126,133,144</sup> This would require the least number of modifications to the currently available reagents. If both *mec-4* and *mec-10* expression information is required, however, there are also other solutions. In this case, we require a GCaMP strain with only green and no red – this could be added as the construct, *pmec-7::GCaMP*. Since this requires the green channel, the *mec-4* reporting strategy must be modified as well. By injecting MEC-4::CyOFP1 and MEC-10::mScarlet-I into the new GCaMP strain described, we can capture the gene expression information of MEC-4 and MEC-10 while measuring neuronal activity with GCaMP as well. Creating a new GCaMP strain with *mec-4* or *mec-10* as the driving promoter may also be possible; however, previous works from collaborators have suggested that these promoters are not as strongly expressed as *mec-7*.

Another solution to gather both gene expressions and the neuronal functional information from a single animal is recovery after functional imaging and then performing smFISH. After imaging the functional responses of the animals, device modifications can perhaps allow these animals to be recovered and isolated for further analysis. Whether through manually sorting animals into different tubes or perhaps designing a more complex, robust microfluidic approach to load them into chambers, keeping individual

identities is key. Following the functional imaging and isolation of each animal, smFISH can be performed on these animals to quantify *mec-4* and *mec-10* gene expression levels. This solution requires more device modifications, but it can perhaps be more readily applied to other biological questions as well since smFISH does not have any strain requirements.

Similar to other proposed future works, smFISH serves as a powerful tool to help answer deeper questions in biology. There are many available microfluidic-based tools that can measure phenotypic information, such as live transcriptional levels, behavioral metrics, and functional imaging, on a single-animal level. By incorporating smFISH to these workflows, we can directly measure underlying gene expression patterns related to the live imaging. These simple modifications can create powerful tools to investigate the diverse roles of gene expression on a sub-cellular level to improve the content of information we can gather on a single-animal level.

## APPENDIX A. CHAPTER 2 SUPPLEMENTARY MATERIALS

The figures below are adapted from the research article, “smFISH in chips: a microfluidic-based pipeline to quantify *in situ* gene expression in whole organisms” published in 2020 in *Lab on a Chip*.<sup>65</sup>

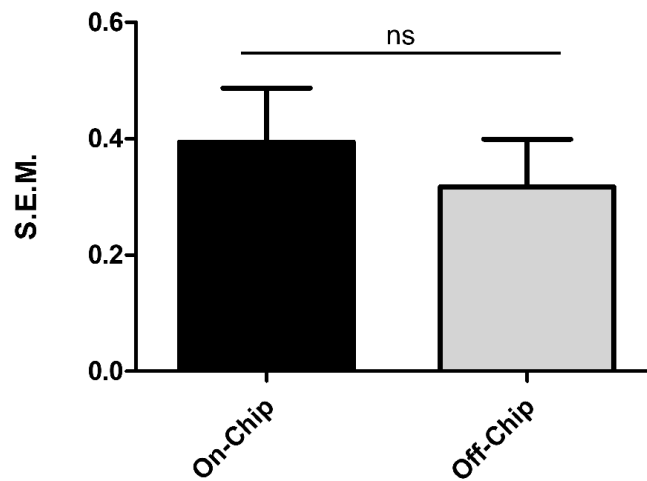
### A.1 Raw Data for *Pdaf-7::Venus* and *gpa-3* expression

**Table A.1.1. Expression data per individual animal.**

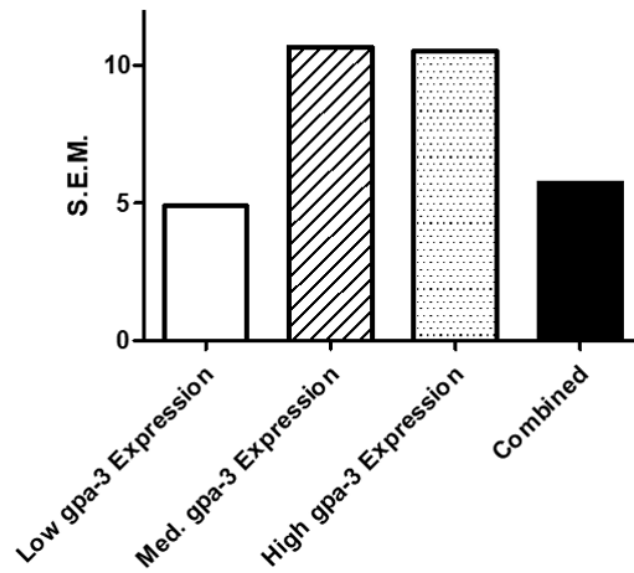
Worm ID	<i>Pdaf-7::Venus</i> (AU)	<i>gpa-3</i> (mRNA counts)
1	0	1
2	0.2	7
3	0.5	1
4	0.5	17
5	1.4	3
6	1.7	9
7	2.6	3
8	2.7	2
9	2.8	2
10	3.8	6
11	4.1	12
12	6.1	15
13	11	13
14	13.9	4
15	17.4	3
16	24.3	3
17	28.3	1
18	28.8	9
19	35.8	2
20	42.6	22
21	44.5	2
22	44.6	6
23	48.5	5
24	53.9	5
25	59.7	17
26	60.9	14
27	62.1	5

Table A.1.1. Continued		
28	69	8
29	71	24
30	73.4	9
31	80.8	8
32	84.8	14
33	106.6	6
34	112.4	21

## A.2 Supplemental Figures for Chapter 2



**Appendix A.2.1. Standard error of the mean (S.E.M.) of *gpa-3* mRNA counts is not significantly different between on- and off-chip conditions.** Each group represents the mean S.E.M. of the three independent experiments, and the error bars represent S.E.M. An unpaired T-test was performed. (ns, not significant)



**Appendix A.2.2. Standard error of the mean (S.E.M.) of *Pdaf-7::Venus* expression in each population bin.** S.E.M. increases as *gpa-3* expression increases, but this information is lost when considering the whole population (combined).

## APPENDIX B. CHAPTER 3 SUPPLEMENTARY MATERIALS

The material below are adapted from the research article, “Rapid and multi-cycle smFISH enabled by microfluidic ion concentration polarization for *in situ* profiling of tissue-specific gene expression in whole *C. elegans*,” published in 2019 in *Biomicrofluidics*.<sup>77</sup>

### B.1 Supplementary Text for the Electrokinetic/Microfluidic Hybrid Device

This work was done in collaboration with Dr. Gongchen Sun, and much of the theory presented here was led by him.

#### B.1.1 Estimating the enhancement of probe transport in the worm by electrokinetics

We estimate the enhancement of probe transport in the worm by characteristic times. In the traditional diffusion-based method, the characteristic time for sufficient probe delivery,  $t_{diffusion}$ , is scaled with:

$$d_{worm}^2/D$$

$d_{worm}$  is the diameter of the worm and  $D$  represents the probe diffusivity in the permeabilized worm.

On the other hand, the characteristic time for probe delivery enhanced by our ICP-based ion pump,  $t_{electrokinetics}$ , is scaled with:

$$l_{worm}/\mu E$$

Here  $l_{worm}$  is the length of the worm across which the electric field is applied (Fig.2),  $\mu$  the electromobility of the probe, and  $E$  the local electric field.



The electromobility  $\mu$  can be related to diffusivity  $D$  by Einstein-Stokes relationship:

$$\frac{D}{\mu} = \frac{RT}{F}$$

Here,  $F$ ,  $R$  and  $T$  represent Faraday constant, ideal gas constant, and temperature, respectively.

We can define the “acceleration” of probe transport by the ratio of characteristic diffusion-based probe delivery time to the characteristic electrokinetically-enhanced time:

$$t_{diffusion}/t_{electrokinetics} \sim \frac{F}{RT} \left(\frac{d_{worm}}{l_{worm}}\right)^2 l_{worm} E$$

Due to the geometrical design of our microfluidic chip (shown in Fig. 1a), the applied electric field is mostly focused in the worm trap region. Therefore, we have  $l_{worm} E \sim V_{input}$ . Hence, the probe transport “acceleration” is scaled with:

$$\left(\frac{d_{worm}}{l_{worm}}\right)^2 \frac{V_{input}}{RT/F}$$

We are especially interested in gene expression in adult *C. elegans*, whose characteristic length  $l_{worm}$  is  $\sim 1$  mm, and characteristic diameter  $d_{worm}$  is  $\sim 60$   $\mu$ m. The absolute value of  $V_{input}$  that we applied is 150 V. Altogether, it yields an over 20 folds enhancement in probe delivery in the worm.

### *B.1.2 Estimating the enhancement of probe hybridization onto target mRNAs by probe enrichment*

We approximate the hybridization between probes and target mRNA molecules as a second-order reaction.<sup>156,157</sup> The reaction kinetics can hence be expressed by:

$$\frac{dC_{probe-mRNA}}{dt} = k_{on} C_{probe} C_{mRNA} - k_{off} C_{probe-mRNA}$$

Here  $C_{probe}$ ,  $C_{mRNA}$ , and  $C_{probe-mRNA}$  are the concentration of the probes, the target mRNAs, and the hybridized probe-mRNA complexes respectively.  $k_{on}$  and  $k_{off}$  denote reaction on- and off- rate constant.

In our case of smFISH experiments, we can assume the probes are in excess ( $C_{probe} \gg C_{mRNA}$ ) and the equilibrium constant is sufficiently low ( $k_{on} \gg k_{off}$ ). Therefore, the fraction of mRNAs hybridized with one probe,  $f = C_{probe-mRNA} / C_{mRNA}$ , can be expressed as:

$$f = 1 - e^{-k_{on}C_{probe}^0 t}$$

Here,  $C_{probe}^0$  denotes the initial probe concentration in the worm after probe delivery.

For each individual mRNA molecule to be visible as a punctum, it requires at least 20 probes to be bound on the same mRNA molecule. These 20 probes are optimally designed to hybridize onto different sequence segments on one mRNA molecule, and their hybridization can be considered as independent reactions. Therefore, the fraction of “visible” mRNA molecules (hybridized with 20 probes),  $F$ , is given by:

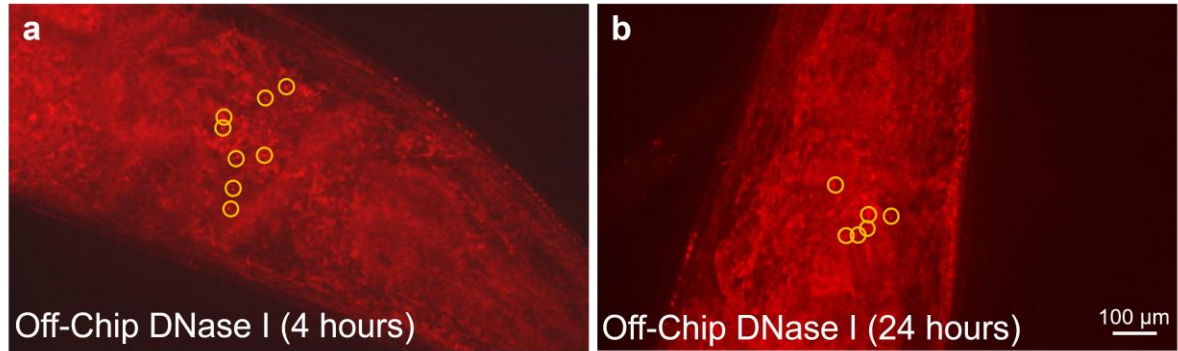
$$F = f^{20} = (1 - e^{-k_{on}C_{probe}^0 t})^{20}$$

We define the characteristic time to complete the smFISH hybridization step,  $\tau_{90\%}$ , as 90% mRNA molecules hybridized with at least 20 probes.  $\tau_{90\%}$  is then given by

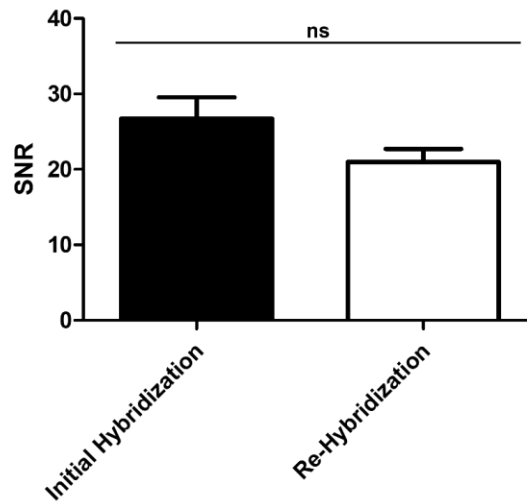
$$\tau_{90\%} = -\ln(1 - \sqrt[20]{0.9}) / k_{on}C_{probe}^0$$

Hence the incubation time required for sufficient probe hybridization onto the target mRNAs is inversely proportional to the enriched probe concentration. We estimate the ion and probe concentration in the worm are enriched by 3-5 folds by our ICP-based method compared with their equilibrium concentration. Therefore, the incubation time required for probe hybridization by our method can be reduced by 3-5 folds correspondingly, compared with traditional methods.

## B.2 Supplementary Figures for the Electrokinetic/Microfluidic Hybrid Device

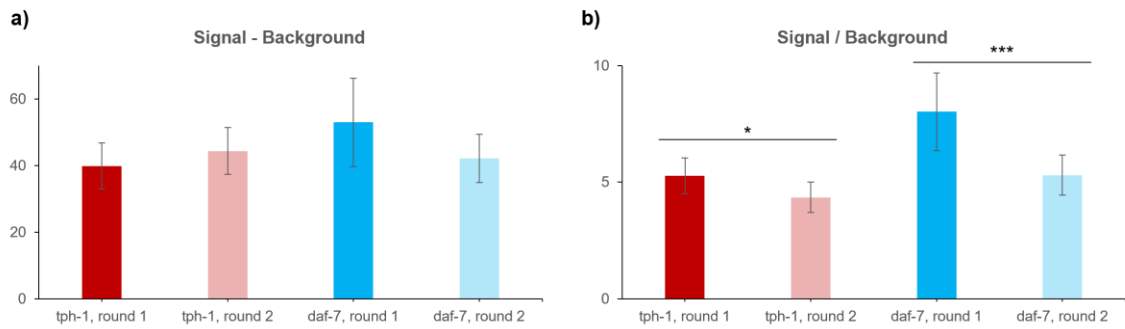


**Appendix B.2.2 Fluorescent images of individual puncta, each corresponding to a *gpa-3* mRNA molecule in the neuronal cells.** Puncta were still visible in the samples after (a) 4 hours and (b) 24 hours of off-chip incubation in the DNase I stripping reagent

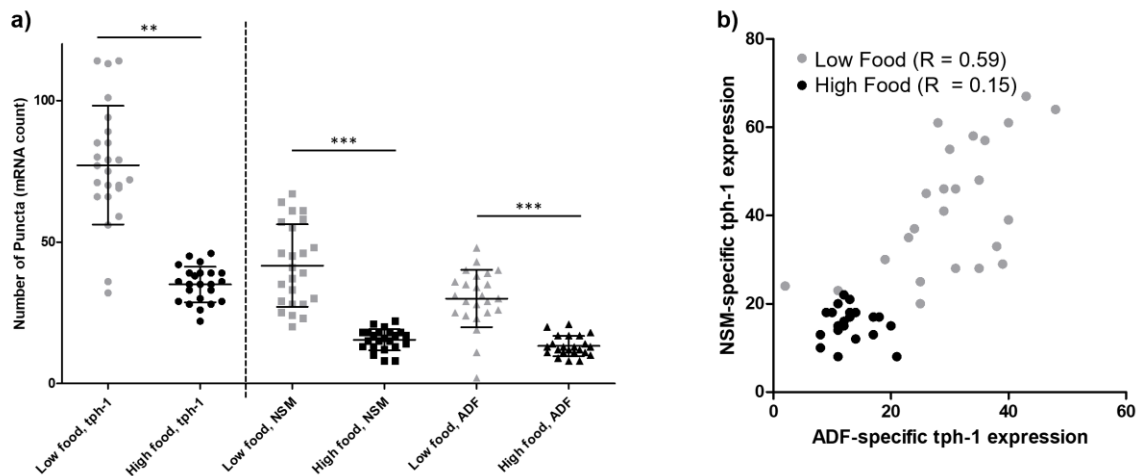


**Appendix B.2.3. Signal-to-noise (SNR) quantification of individual puncta in the multi-cycle smFISH assay.** Puncta signal quality was not significantly different from the initial hybridization to the re-hybridization. An unpaired, two-tailed T test was performed. (ns, not significant)

### B.3 Supplementary Figure for the Formamide-based Stripping Approach



**Appendix B.3.1. Signal minus background and signal-to-background ratio of individual puncta.** While (a) there were no statistically significant differences in the signal minus background between the two rounds, there were (b) significant decreases in the signal-to-background ratio. This suggests that more rounds lead to increased difficulty in distinguishing puncta from the background. A paired, two-tailed T test was performed. (\* $P < 0.05$ , \*\*\* $P < 0.001$ )



**Appendix B.3.2. *tph-1* gene expression in NSM and ADF neurons.** *tph-1* is primarily expressed in the NSM and ADF neurons. (a) The smFISH dataset enables tissue-specific gene expression quantification in these neurons. (b) The tissue-specific gene expression relationships between the two neurons are different under different food conditions. Unpaired, two-tailed T tests were performed between the food conditions (\*\* $P < 0.01$ , \*\*\* $P < 0.001$ ).

#### B.4 Gene expression data for each individual animal

**Table B.4.1. Multicycle smFISH validation with *tph-1* and *daf-7***

	<i>tph-1</i>		<i>daf-7</i>	
<b>Worm ID</b>	<b>Round 1</b>	<b>Round 2</b>	<b>Round 1</b>	<b>Round 2</b>
1	90	105	99	94
2	66	64	98	90
3	97	95	70	70
4	94	85	88	80
5	77	77	117	115
6	67	81	87	90
7	70	77	67	56
8	60	56	63	56
9	59	67	69	74
10	83	67	62	62
11	92	79	90	101
12	79	95	110	107
13	95	104	126	112
14	96	85	103	96
15	80	76	90	83
16	78	113	134	112
17	136	101	119	132
18	56	63	69	55
19	101	125	107	107
20	54	61	107	115
21	97	91	106	98

**Table B.4.2. Multicycle smFISH with *tph-1*, *daf-7*, *cat-2*, and *tdc-1* at OD1**

<b>OD1</b>	<b>Round 1</b>		<b>Round 2</b>	
<b>Worm ID</b>	<i>tph-1</i>	<i>daf-7</i>	<i>tdc-1</i>	<i>cat-2</i>
1	85	14	23	2
2	70	26	34	8
3	36	5	28	11
4	113	29	57	16
5	77	21	56	5
6	56	5	26	5
7	69	37	23	5
8	79	70	27	13
9	80	23	42	20

Table B.4.2 Continued				
10	79	41	29	4
11	75	78	19	7
12	85	25	47	19
13	114	41	57	16
14	72	34	32	13
15	71	71	34	7
16	70	34	35	16
17	94	30	47	15
18	59	23	19	12
19	66	55	26	7
20	66	26	37	15
21	114	74	22	21
22	32	27	17	13
23	101	63	23	5
24	89	42	28	8

**Table B.4.3. Multicycle smFISH with *tph-1*, *daf-7*, *cat-2*, and *tdc-1* at OD10**

OD10	Round 1		Round 2	
Worm ID	<i>tph-1</i>	<i>daf-7</i>	<i>tdc-1</i>	<i>cat-2</i>
1	39	78	18	12
2	35	22	16	14
3	26	65	23	15
4	30	30	11	9
5	33	38	8	10
6	39	53	27	11
7	39	50	11	10
8	46	21	21	7
9	35	22	12	6
10	43	37	11	11
11	36	52	10	10
12	35	46	26	12
13	33	26	4	4
14	39	35	30	14
15	36	51	14	19
16	29	21	19	12
17	28	30	8	6
18	22	38	17	8
19	42	31	8	10
20	38	36	10	11
21	45	29	19	10
22	28	30	9	4
23	29	22	20	11

## APPENDIX C. CHAPTER 4 SUPPLEMENTARY MATERIALS

The material below is adapted from the research article, “Microfluidic approach to correlate *C. elegans* neuronal functional aging and underlying changes of gene expression in mechanosensation,” currently (2022) in submission.

### C.1 Supplementary Text for the Computational Deformation Modeling

This work was done in collaboration with Jimmy Ding and much of the details presented here was led by him. The COMSOL stationary solver was used to analyze the effect of varying pressure on the deformation of the stimulus valve membrane. The values for the material properties of the PDMS and *C. elegans*, such as Young’s Modulus and density, were taken from several sources and a range of potential PDMS material properties based on a 20% variation in cross-linker ratio and temperature were estimated<sup>137-140</sup>. Using these literature sources, the range of material properties used was estimated (Table 4.1).

To accommodate the extreme deformations produced, both the PDMS and cuticle were modeled as a hyperelastic materials. The hyperelastic material model is commonly applied to biological tissues and rubbers and has been previously used for both PDMS and *C. elegans*<sup>158-161</sup>. The model chosen was simplified to follow a non-compressible Neo-Hookean model, where the Lamé parameter was defined as  $\mu = E/3$ , as the compression of the PDMS membrane was not the point of interest of the study.

A 2D cross sectional view of the imaging channel was used in the study, for both a 50  $\mu\text{m}$  and 60  $\mu\text{m}$  channel width and matching worm diameter. The bottom and top edges of the device were constrained to zero deformation to simulate their attachment to glass

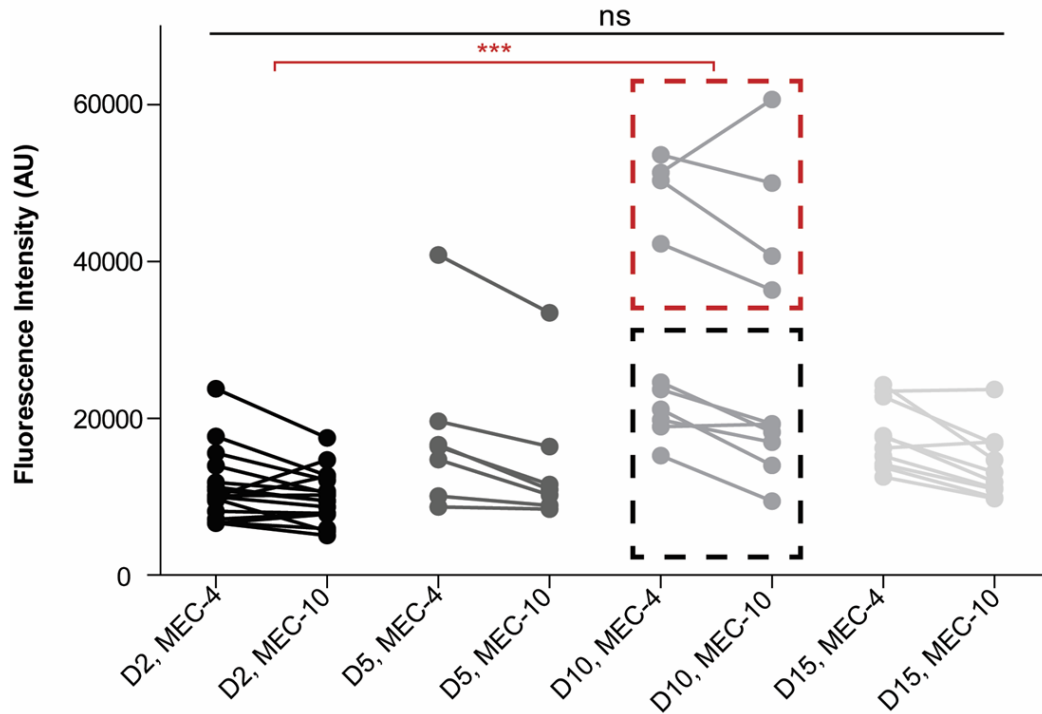
and the massive amount of significantly stiffer PDMS surrounding the membrane. The outside faces of the valves were assigned a boundary pressure, whereas the insides and the entire outside of the worm were paired into contact pairs. The worm was modeled as a ring of hyperelastic material based on the properties of the cuticle. Following COMSOL application model 206, which assumes ideal gas law, an internal pressure was defined within the ring, increasing in magnitude as the area of the ring decreased according to  $P_{int} = (0.1 \text{ MPa}) * [(Area_{t=0}/Area_{enclosed})^{1.4} - 1]$ , where  $Area_{enclosed}$  is calculated by integrating the inner boundary of the ring.

Because compressibility of the worm has been observed in <sup>137</sup>, and furthermore the model does not consider the sections of the worm before and beyond the valve, about 90% of the total length of the animal, which would experience the large majority of the resulting forces and deformation produced by the compression, the interior of the worm is considered to be a compressible fluid rather than an incompressible liquid (i.e. water). The initial pressure value implies that at approximately 40% deformation of the modeled section, about 4% of the entire animal, the internal pressure is .1 MPa, which roughly agrees with the observed results in prior literature <sup>137</sup>.

The pressure applied to the deformable membrane was parametrically increased and contact between the PDMS membrane and the animal was solved for nonlinearly. A cut-line drawn through the center of each membrane was used to extract the distance between the two membranes during deformation and estimate percent deformation.



## C.2 Supplemental Figures for Chapter 4



**Appendix C.2.1. Individual animals' *mec-4* and *mec-10* expressions are strongly correlated and the high-expressing population in Day 10 is responsible for the differences between the ages.** Each animal's *mec-4* and *mec-10* expression levels were related (line between the points). While there is an increase at Day 10, only the high-expressing animals of the population are responsible for the significant difference between other ages (red box). There is perhaps a bimodal distribution of animals at Day 10, where the high expressing population is not present at Day 15.

## REFERENCES

- 1     United Nations, D. o. E. a. S. A. World Population Ageing 2017 - Highlights. *Population Division* (2017).
- 2     Guarente, L. & Kenyon, C. Genetic pathways that regulate ageing in model organisms. *Nature* **408**, 255-262, doi:10.1038/35041700 (2000).
- 3     Kenyon, C. J. The genetics of ageing. *Nature* **464**, 504-512, doi:10.1038/nature08980 (2010).
- 4     Jin, K. Modern Biological Theories of Aging. *Aging Dis* **1**, 72-74 (2010).
- 5     Partridge, L. & Gems, D. Mechanisms of ageing: public or private? *Nat. Rev. Genet.* **3**, 165-175, doi:10.1038/nrg753 (2002).
- 6     Kenyon, C., Chang, J., Gensch, E., Rudner, A. & Tabtiang, R. A *C. elegans* mutant that lives twice as long as wild type. *Nature* **366**, 461-464, doi:10.1038/366461a0 (1993).
- 7     Shaye, D. D. & Greenwald, I. OrthoList: a compendium of *C. elegans* genes with human orthologs. *PLoS One* **6**, e20085, doi:10.1371/journal.pone.0020085 (2011).
- 8     Fontana, L., Partridge, L. & Longo, V. D. Extending healthy life span--from yeast to humans. *Science* **328**, 321-326, doi:10.1126/science.1172539 (2010).
- 9     Entchev, E. V. *et al.* A gene-expression-based neural code for food abundance that modulates lifespan. *Elife* **4**, e06259, doi:10.7554/eLife.06259 (2015).
- 10    Meisel, J. D., Panda, O., Mahanti, P., Schroeder, F. C. & Kim, D. H. Chemosensation of bacterial secondary metabolites modulates neuroendocrine signaling and behavior of *C. elegans*. *Cell* **159**, 267-280, doi:10.1016/j.cell.2014.09.011 (2014).
- 11    Rangaraju, S. *et al.* Suppression of transcriptional drift extends *C. elegans* lifespan by postponing the onset of mortality. *Elife* **4**, e08833, doi:10.7554/eLife.08833 (2015).
- 12    Elowitz, M. B., Levine, A. J., Siggia, E. D. & Swain, P. S. Stochastic gene expression in a single cell. *Science* **297**, 1183-1186, doi:10.1126/science.1070919 (2002).
- 13    Raj, A. & van Oudenaarden, A. Nature, nurture, or chance: stochastic gene expression and its consequences. *Cell* **135**, 216-226, doi:10.1016/j.cell.2008.09.050 (2008).

- 14 Hahm, J. H., Kim, S. & Paik, Y. K. Endogenous cGMP regulates adult longevity via the insulin signaling pathway in *Caenorhabditis elegans*. *Aging Cell* **8**, 473-483, doi:10.1111/j.1474-9726.2009.00495.x (2009).
- 15 Pincus, Z., Smith-Vikos, T. & Slack, F. J. MicroRNA predictors of longevity in *Caenorhabditis elegans*. *PLoS Genet.* **7**, e1002306, doi:10.1371/journal.pgen.1002306 (2011).
- 16 Shaw, W. M., Luo, S., Landis, J., Ashraf, J. & Murphy, C. T. The *C. elegans* TGF-beta Dauer pathway regulates longevity via insulin signaling. *Curr. Biol.* **17**, 1635-1645, doi:10.1016/j.cub.2007.08.058 (2007).
- 17 Lans, H. & Jansen, G. Multiple sensory G proteins in the olfactory, gustatory and nociceptive neurons modulate longevity in *Caenorhabditis elegans*. *Dev. Biol.* **303**, 474-482, doi:10.1016/j.ydbio.2006.11.028 (2007).
- 18 Bahar, R. *et al.* Increased cell-to-cell variation in gene expression in ageing mouse heart. *Nature* **441**, 1011-1014, doi:10.1038/nature04844 (2006).
- 19 Bashkeel, N., Perkins, T. J., Kaern, M. & Lee, J. M. Human gene expression variability and its dependence on methylation and aging. *BMC Genomics* **20**, 941, doi:10.1186/s12864-019-6308-7 (2019).
- 20 Kirkwood, T. B. *et al.* What accounts for the wide variation in life span of genetically identical organisms reared in a constant environment? *Mech Ageing Dev* **126**, 439-443, doi:10.1016/j.mad.2004.09.008 (2005).
- 21 Martinez-Jimenez, C. P. *et al.* Aging increases cell-to-cell transcriptional variability upon immune stimulation. *Science* **355**, 1433-1436, doi:10.1126/science.aah4115 (2017).
- 22 Liu, P., Song, R., Elison, G. L., Peng, W. & Acar, M. Noise reduction as an emergent property of single-cell aging. *Nat Commun* **8**, 680, doi:10.1038/s41467-017-00752-9 (2017).
- 23 Wan, J. & Lu, H. Enabling high-throughput single-animal gene-expression studies with molecular and micro-scale technologies. *Lab Chip* **20**, 4528-4538, doi:10.1039/d0lc00881h (2020).
- 24 Kulkarni, A., Anderson, A. G., Merullo, D. P. & Konopka, G. Beyond bulk: a review of single cell transcriptomics methodologies and applications. *Curr. Opin. Biotechnol.* **58**, 129-136, doi:10.1016/j.copbio.2019.03.001 (2019).
- 25 Liao, J., Lu, X., Shao, X., Zhu, L. & Fan, X. Uncovering an Organ's Molecular Architecture at Single-Cell Resolution by Spatially Resolved Transcriptomics. *Trends Biotechnol.* **39**, 43-58, doi:10.1016/j.tibtech.2020.05.006 (2021).

- 26 Zhao, S., Fung-Leung, W. P., Bittner, A., Ngo, K. & Liu, X. Comparison of RNA-Seq and microarray in transcriptome profiling of activated T cells. *PLoS One* **9**, e78644, doi:10.1371/journal.pone.0078644 (2014).
- 27 Mantione, K. J. *et al.* Comparing bioinformatic gene expression profiling methods: microarray and RNA-Seq. *Med Sci Monit Basic Res* **20**, 138-142, doi:10.12659/MSMBR.892101 (2014).
- 28 Girardot, F., Lasbleiz, C., Monnier, V. & Tricoire, H. Specific age-related signatures in *Drosophila* body parts transcriptome. *BMC Genomics* **7**, 69, doi:10.1186/1471-2164-7-69 (2006).
- 29 Zhan, M. *et al.* Temporal and spatial transcriptional profiles of aging in *Drosophila melanogaster*. *Genome Res.* **17**, 1236-1243, doi:10.1101/gr.6216607 (2007).
- 30 Golden, T. R. & Melov, S. Microarray analysis of gene expression with age in individual nematodes. *Aging Cell* **3**, 111-124, doi:10.1111/j.1474-9728.2004.00095.x (2004).
- 31 Ma, S. *et al.* Caloric Restriction Reprograms the Single-Cell Transcriptional Landscape of *Rattus Norvegicus* Aging. *Cell* **180**, 984-1001 e1022, doi:10.1016/j.cell.2020.02.008 (2020).
- 32 Pacifico, R., MacMullen, C. M., Walkinshaw, E., Zhang, X. & Davis, R. L. Brain transcriptome changes in the aging *Drosophila melanogaster* accompany olfactory memory performance deficits. *PLoS One* **13**, e0209405, doi:10.1371/journal.pone.0209405 (2018).
- 33 Serra, L. *et al.* Adapting the Smart-seq2 Protocol for Robust Single Worm RNA-seq. *Bio Protoc* **8**, e2729, doi:10.21769/BioProtoc.2729 (2018).
- 34 Wood, S. H., Craig, T., Li, Y., Merry, B. & de Magalhaes, J. P. Whole transcriptome sequencing of the aging rat brain reveals dynamic RNA changes in the dark matter of the genome. *Age (Dordr)* **35**, 763-776, doi:10.1007/s11357-012-9410-1 (2013).
- 35 Kolodziejczyk, A. A., Kim, J. K., Svensson, V., Marioni, J. C. & Teichmann, S. A. The technology and biology of single-cell RNA sequencing. *Mol. Cell* **58**, 610-620, doi:10.1016/j.molcel.2015.04.005 (2015).
- 36 Brennecke, P. *et al.* Accounting for technical noise in single-cell RNA-seq experiments. *Nat. Methods* **10**, 1093-1095, doi:10.1038/nmeth.2645 (2013).
- 37 Liu, S. & Trapnell, C. Single-cell transcriptome sequencing: recent advances and remaining challenges. *F1000Res* **5**, F1000 Faculty Rev-1182, doi:10.12688/f1000research.7223.1 (2016).

- 38 Wildt, S. & Deuschle, U. *cobA*, a red fluorescent transcriptional reporter for *Escherichia coli*, yeast, and mammalian cells. *Nat. Biotechnol.* **17**, 1175-1178, doi:10.1038/70713 (1999).
- 39 He, L., Binari, R., Huang, J., Falo-Sanjuan, J. & Perrimon, N. In vivo study of gene expression with an enhanced dual-color fluorescent transcriptional timer. *Elife* **8**, e46181, doi:10.7554/eLife.46181 (2019).
- 40 Boulin, T., Etchberger, J. F. & Hobert, O. (WormBook, The *C. elegans* Research Community, 2006).
- 41 Pichon, X., Lagha, M., Mueller, F. & Bertrand, E. A Growing Toolbox to Image Gene Expression in Single Cells: Sensitive Approaches for Demanding Challenges. *Mol. Cell* **71**, 468-480, doi:10.1016/j.molcel.2018.07.022 (2018).
- 42 Raj, A., van den Bogaard, P., Rifkin, S. A., van Oudenaarden, A. & Tyagi, S. Imaging individual mRNA molecules using multiple singly labeled probes. *Nat. Methods* **5**, 877-879, doi:10.1038/nmeth.1253 (2008).
- 43 Chen, K. H., Boettiger, A. N., Moffitt, J. R., Wang, S. & Zhuang, X. RNA imaging. Spatially resolved, highly multiplexed RNA profiling in single cells. *Science* **348**, aaa6090, doi:10.1126/science.aaa6090 (2015).
- 44 Eng, C. L. *et al.* Transcriptome-scale super-resolved imaging in tissues by RNA seqFISH. *Nature* **568**, 235-239, doi:10.1038/s41586-019-1049-y (2019).
- 45 Xia, C., Fan, J., Emanuel, G., Hao, J. & Zhuang, X. Spatial transcriptome profiling by MERFISH reveals subcellular RNA compartmentalization and cell cycle-dependent gene expression. *Proc Natl Acad Sci U S A* **116**, 19490-19499, doi:10.1073/pnas.1912459116 (2019).
- 46 Asp, M., Bergenstrahle, J. & Lundeberg, J. Spatially Resolved Transcriptomes-Next Generation Tools for Tissue Exploration. *Bioessays* **42**, e1900221, doi:10.1002/bies.201900221 (2020).
- 47 Stahl, P. L. *et al.* Visualization and analysis of gene expression in tissue sections by spatial transcriptomics. *Science* **353**, 78-82, doi:10.1126/science.aaf2403 (2016).
- 48 Rodriques, S. G. *et al.* Slide-seq: A scalable technology for measuring genome-wide expression at high spatial resolution. *Science* **363**, 1463-1467, doi:10.1126/science.aaw1219 (2019).
- 49 Cao, J. *et al.* Comprehensive single-cell transcriptional profiling of a multicellular organism. *Science* **357**, 661-667, doi:10.1126/science.aam8940 (2017).
- 50 Islam, S. *et al.* Quantitative single-cell RNA-seq with unique molecular identifiers. *Nat. Methods* **11**, 163-166, doi:10.1038/nmeth.2772 (2014).

- 51 Satija, R., Farrell, J. A., Gennert, D., Schier, A. F. & Regev, A. Spatial reconstruction of single-cell gene expression data. *Nat. Biotechnol.* **33**, 495-502, doi:10.1038/nbt.3192 (2015).
- 52 Achim, K. *et al.* High-throughput spatial mapping of single-cell RNA-seq data to tissue of origin. *Nat. Biotechnol.* **33**, 503-509, doi:10.1038/nbt.3209 (2015).
- 53 Shalek, A. K. *et al.* Single-cell RNA-seq reveals dynamic paracrine control of cellular variation. *Nature* **510**, 363-369, doi:10.1038/nature13437 (2014).
- 54 Vera, M., Tutucci, E. & Singer, R. H. in *Imaging Gene Expression: Methods and Protocols* (ed Yaron Shav-Tal) 3-20 (Springer New York, 2019).
- 55 Tutucci, E. *et al.* An improved MS2 system for accurate reporting of the mRNA life cycle. *Nat. Methods* **15**, 81-89, doi:10.1038/nmeth.4502 (2018).
- 56 Pichon, X., Robert, M.-C., Bertrand, E., Singer, R. H. & Tutucci, E. in *RNA Tagging: Methods and Protocols* (ed Manfred Heinlein) 121-144 (Springer US, 2020).
- 57 Abudayyeh, O. O. *et al.* RNA targeting with CRISPR-Cas13. *Nature* **550**, 280-284, doi:10.1038/nature24049 (2017).
- 58 Chalfie, M., Tu, Y., Euskirchen, G., Ward, W. W. & Prasher, D. C. Green fluorescent protein as a marker for gene expression. *Science* **263**, 802-805, doi:10.1126/science.8303295 (1994).
- 59 Phillips, N. E., Mandic, A., Omid, S., Naef, F. & Suter, D. M. Memory and relatedness of transcriptional activity in mammalian cell lineages. *Nat Commun* **10**, 1208, doi:10.1038/s41467-019-09189-8 (2019).
- 60 Li, X. *et al.* Generation of destabilized green fluorescent protein as a transcription reporter. *J. Biol. Chem.* **273**, 34970-34975, doi:10.1074/jbc.273.52.34970 (1998).
- 61 Snapp, E. L. Fluorescent proteins: a cell biologist's user guide. *Trends Cell Biol.* **19**, 649-655, doi:10.1016/j.tcb.2009.08.002 (2009).
- 62 Frokjaer-Jensen, C. *et al.* Single-copy insertion of transgenes in *Caenorhabditis elegans*. *Nat. Genet.* **40**, 1375-1383, doi:10.1038/ng.248 (2008).
- 63 Posner, R. *et al.* Neuronal Small RNAs Control Behavior Transgenerationally. *Cell* **177**, 1814-1826 e1815, doi:10.1016/j.cell.2019.04.029 (2019).
- 64 Trcek, T. *et al.* *Drosophila* germ granules are structured and contain homotypic mRNA clusters. *Nat Commun* **6**, 7962, doi:10.1038/ncomms8962 (2015).

- 65 Wan, J., Sun, G., Dicient, J., Patel, D. S. & Lu, H. smFISH in chips: a microfluidic-based pipeline to quantify in situ gene expression in whole organisms. *Lab Chip* **20**, 266-273, doi:10.1039/c9lc00896a (2020).
- 66 Ji, N. & van Oudenaarden, A. in *WormBook* (ed The C. elegans Research Community) (WormBook).
- 67 Lee, H. *et al.* A multi-channel device for high-density target-selective stimulation and long-term monitoring of cells and subcellular features in C. elegans. *Lab Chip* **14**, 4513-4522, doi:10.1039/c4lc00789a (2014).
- 68 Mueller, F. *et al.* FISH-quant: automatic counting of transcripts in 3D FISH images. *Nat. Methods* **10**, 277-278, doi:10.1038/nmeth.2406 (2013).
- 69 Hammarlund, M., Hobert, O., Miller, D. M., 3rd & Sestan, N. The CeNGEN Project: The Complete Gene Expression Map of an Entire Nervous System. *Neuron* **99**, 430-433, doi:10.1016/j.neuron.2018.07.042 (2018).
- 70 de Bono, M., Tobin, D. M., Davis, M. W., Avery, L. & Bargmann, C. I. Social feeding in *Caenorhabditis elegans* is induced by neurons that detect aversive stimuli. *Nature* **419**, 899-903, doi:10.1038/nature01169 (2002).
- 71 Gallagher, T., Kim, J., Oldenbroek, M., Kerr, R. & You, Y. J. ASI regulates satiety quiescence in C. elegans. *J. Neurosci.* **33**, 9716-9724, doi:10.1523/JNEUROSCI.4493-12.2013 (2013).
- 72 Hilliard, M. A., Bergamasco, C., Arbucci, S., Plasterk, R. H. & Bazzicalupo, P. Worms taste bitter: ASH neurons, QUI-1, GPA-3 and ODR-3 mediate quinine avoidance in *Caenorhabditis elegans*. *EMBO J.* **23**, 1101-1111, doi:10.1038/sj.emboj.7600107 (2004).
- 73 Jansen, G. *et al.* The complete family of genes encoding G proteins of *Caenorhabditis elegans*. *Nat. Genet.* **21**, 414-419, doi:10.1038/7753 (1999).
- 74 Kim, K. *et al.* Two chemoreceptors mediate developmental effects of dauer pheromone in C. elegans. *Science* **326**, 994-998, doi:10.1126/science.1176331 (2009).
- 75 Chung, K. *et al.* A microfluidic array for large-scale ordering and orientation of embryos. *Nat. Methods* **8**, 171-176, doi:10.1038/nmeth.1548 (2011).
- 76 Chung, K., Rivet, C. A., Kemp, M. L. & Lu, H. Imaging single-cell signaling dynamics with a deterministic high-density single-cell trap array. *Anal Chem* **83**, 7044-7052, doi:10.1021/ac2011153 (2011).
- 77 Sun, G., Wan, J. & Lu, H. Rapid and multi-cycle smFISH enabled by microfluidic ion concentration polarization for in-situ profiling of tissue-specific gene

- expression in whole *C. elegans*. *Biomicrofluidics* **13**, 064101, doi:10.1063/1.5124827 (2019).
- 78 Le, K. N. *et al.* An automated platform to monitor long-term behavior and healthspan in *Caenorhabditis elegans* under precise environmental control. *Commun Biol* **3**, 297, doi:10.1038/s42003-020-1013-2 (2020).
  - 79 Eng, C.-H. L. *et al.* Transcriptome-scale super-resolved imaging in tissues by RNA seqFISH+. *Nature* **568**, 235-239, doi:10.1038/s41586-019-1049-y (2019).
  - 80 Rea, S. L., Wu, D., Cypser, J. R., Vaupel, J. W. & Johnson, T. E. A stress-sensitive reporter predicts longevity in isogenic populations of *Caenorhabditis elegans*. *Nat. Genet.* **37**, 894-898, doi:10.1038/ng1608 (2005).
  - 81 Wernet, M. F. *et al.* Stochastic spineless expression creates the retinal mosaic for colour vision. *Nature* **440**, 174-180, doi:10.1038/nature04615 (2006).
  - 82 Lubeck, E., Coskun, A. F., Zhiyentayev, T., Ahmad, M. & Cai, L. Single-cell in situ RNA profiling by sequential hybridization. *Nat. Methods* **11**, 360-361, doi:10.1038/nmeth.2892 (2014).
  - 83 Harterink, M. *et al.* Neuroblast migration along the anteroposterior axis of *C. elegans* is controlled by opposing gradients of Wnts and a secreted Frizzled-related protein. *Development* **138**, 2915-2924, doi:10.1242/dev.064733 (2011).
  - 84 Yossifon, G., Mushenheim, P., Chang, Y. C. & Chang, H. C. Nonlinear current-voltage characteristics of nanochannels. *Phys Rev E Stat Nonlin Soft Matter Phys* **79**, 046305, doi:10.1103/PhysRevE.79.046305 (2009).
  - 85 Yossifon, G. & Chang, H. C. Selection of nonequilibrium overlimiting currents: universal depletion layer formation dynamics and vortex instability. *Phys Rev Lett* **101**, 254501, doi:10.1103/PhysRevLett.101.254501 (2008).
  - 86 Tsuruoka, M. *et al.* Optimization of the rate of DNA hybridization and rapid detection of methicillin resistant *Staphylococcus aureus* DNA using fluorescence polarization. *J. Biotechnol.* **48**, 201-208, doi:10.1016/0168-1656(96)01510-6 (1996).
  - 87 Fujimoto, B. S., Miller, J. M., Ribeiro, N. S. & Schurr, J. M. Effects of different cations on the hydrodynamic radius of DNA. *Biophys. J.* **67**, 304-308, doi:10.1016/S0006-3495(94)80481-3 (1994).
  - 88 Marczak, S., Senapati, S., Slouka, Z. & Chang, H. C. Induced nanoparticle aggregation for short nucleic acid quantification by depletion isotachopheresis. *Biosens Bioelectron* **86**, 840-848, doi:10.1016/j.bios.2016.07.093 (2016).
  - 89 Qu, Y., Marshall, L. A. & Santiago, J. G. Simultaneous purification and fractionation of nucleic acids and proteins from complex samples using



- bidirectional isotachopheresis. *Anal Chem* **86**, 7264-7268, doi:10.1021/ac501299a (2014).
- 90 Quist, J., Janssen, K. G., Vulto, P., Hankemeier, T. & van der Linden, H. J. Single-electrolyte isotachopheresis using a nanochannel-induced depletion zone. *Anal Chem* **83**, 7910-7915, doi:10.1021/ac2018348 (2011).
- 91 Quist, J., Vulto, P., van der Linden, H. & Hankemeier, T. Tunable ionic mobility filter for depletion zone isotachopheresis. *Anal Chem* **84**, 9065-9071, doi:10.1021/ac301612n (2012).
- 92 Bharadwaj, R., Santiago, J. G. & Mohammadi, B. Design and optimization of on-chip capillary electrophoresis. *Electrophoresis* **23**, 2729-2744, doi:10.1002/1522-2683(200208)23:16<2729::AID-ELPS2729>3.0.CO;2-I (2002).
- 93 Sawin, E. R., Ranganathan, R. & Horvitz, H. R. C. elegans Locomotory Rate Is Modulated by the Environment through a Dopaminergic Pathway and by Experience through a Serotonergic Pathway. *Neuron* **26**, 619-631, doi:10.1016/s0896-6273(00)81199-x (2000).
- 94 Sze, J. Y., Victor, M., Loer, C., Shi, Y. & Ruvkun, G. Food and metabolic signalling defects in a *Caenorhabditis elegans* serotonin-synthesis mutant. *Nature* **403**, 560-564, doi:10.1038/35000609 (2000).
- 95 Ren, P. *et al.* Control of *C. elegans* larval development by neuronal expression of a TGF-beta homolog. *Science* **274**, 1389-1391, doi:10.1126/science.274.5291.1389 (1996).
- 96 Chase, D. L. & Koelle, M. R. in *WormBook* (ed The *C. elegans* Research Community) (WormBook).
- 97 Diana, G. *et al.* Genetic control of encoding strategy in a food-sensing neural circuit. *Elife* **6**, e24040, doi:10.7554/eLife.24040 (2017).
- 98 Alkema, M. J., Hunter-Ensor, M., Ringstad, N. & Horvitz, H. R. Tyramine Functions independently of octopamine in the *Caenorhabditis elegans* nervous system. *Neuron* **46**, 247-260, doi:10.1016/j.neuron.2005.02.024 (2005).
- 99 Lints, R. & Emmons, S. W. Patterning of dopaminergic neurotransmitter identity among *Caenorhabditis elegans* ray sensory neurons by a TGFbeta family signaling pathway and a Hox gene. *Development* **126**, 5819-5831, doi:10.1242/dev.126.24.5819 (1999).
- 100 Pan, C. L., Peng, C. Y., Chen, C. H. & McIntire, S. Genetic analysis of age-dependent defects of the *Caenorhabditis elegans* touch receptor neurons. *Proc Natl Acad Sci U S A* **108**, 9274-9279, doi:10.1073/pnas.1011711108 (2011).

- 101 Hunter, S. K., Pereira, H. M. & Keenan, K. G. The aging neuromuscular system and motor performance. *J Appl Physiol* (1985) **121**, 982-995, doi:10.1152/jappphysiol.00475.2016 (2016).
- 102 Degens, H. & Korhonen, M. T. Factors contributing to the variability in muscle ageing. *Maturitas* **73**, 197-201, doi:10.1016/j.maturitas.2012.07.015 (2012).
- 103 Maki, B. E. & McIlroy, W. E. Control of rapid limb movements for balance recovery: age-related changes and implications for fall prevention. *Age Ageing* **35 Suppl 2**, ii12-ii18, doi:10.1093/ageing/afl078 (2006).
- 104 Seidman, M. D., Ahmad, N. & Bai, U. Molecular mechanisms of age-related hearing loss. *Ageing Res Rev* **1**, 331-343, doi:10.1016/s1568-1637(02)00004-1 (2002).
- 105 Campbell, A. J., Reinken, J., Allan, B. C. & Martinez, G. S. Falls in old age: a study of frequency and related clinical factors. *Age Ageing* **10**, 264-270, doi:10.1093/ageing/10.4.264 (1981).
- 106 Yamasoba, T. *et al.* Current concepts in age-related hearing loss: epidemiology and mechanistic pathways. *Hear Res* **303**, 30-38, doi:10.1016/j.heares.2013.01.021 (2013).
- 107 Wicks, S. R. & Rankin, C. H. Integration of mechanosensory stimuli in *Caenorhabditis elegans*. *J. Neurosci.* **15**, 2434-2444, doi:10.1523/JNEUROSCI.15-03-02434.1995 (1995).
- 108 Chalfie, M. *et al.* The neural circuit for touch sensitivity in *Caenorhabditis elegans*. *J. Neurosci.* **5**, 956-964, doi:10.1523/JNEUROSCI.05-04-00956.1985 (1985).
- 109 White, J. G., Southgate, E., Thomson, J. N. & Brenner, S. The structure of the nervous system of the nematode *Caenorhabditis elegans*. *Philos Trans R Soc Lond B Biol Sci* **314**, 1-340, doi:10.1098/rstb.1986.0056 (1986).
- 110 Varshney, L. R., Chen, B. L., Paniagua, E., Hall, D. H. & Chklovskii, D. B. Structural properties of the *Caenorhabditis elegans* neuronal network. *PLoS Comput Biol* **7**, e1001066, doi:10.1371/journal.pcbi.1001066 (2011).
- 111 Liu, M., Sharma, A. K., Shaevitz, J. W. & Leifer, A. M. Temporal processing and context dependency in *Caenorhabditis elegans* response to mechanosensation. *Elife* **7**, e36419, doi:10.7554/eLife.36419 (2018).
- 112 Porto, D. A., Giblin, J., Zhao, Y. & Lu, H. Reverse-Correlation Analysis of the Mechanosensation Circuit and Behavior in *C. elegans* Reveals Temporal and Spatial Encoding. *Sci Rep* **9**, 5182, doi:10.1038/s41598-019-41349-0 (2019).

- 113 Chung, K., Crane, M. M. & Lu, H. Automated on-chip rapid microscopy, phenotyping and sorting of *C. elegans*. *Nat. Methods* **5**, 637-643, doi:10.1038/nmeth.1227 (2008).
- 114 Saberi-Bosari, S., Huayta, J. & San-Miguel, A. A microfluidic platform for lifelong high-resolution and high throughput imaging of subtle aging phenotypes in *C. elegans*. *Lab Chip* **18**, 3090-3100, doi:10.1039/c8lc00655e (2018).
- 115 Crane, M. M., Chung, K., Stirman, J. & Lu, H. Microfluidics-enabled phenotyping, imaging, and screening of multicellular organisms. *Lab Chip* **10**, 1509-1517, doi:10.1039/b927258e (2010).
- 116 McClanahan, P. D., Xu, J. H. & Fang-Yen, C. Comparing *Caenorhabditis elegans* gentle and harsh touch response behavior using a multiplexed hydraulic microfluidic device. *Integr Biol (Camb)* **9**, 800-809, doi:10.1039/c7ib00120g (2017).
- 117 Churgin, M. A. *et al.* Longitudinal imaging of *Caenorhabditis elegans* in a microfabricated device reveals variation in behavioral decline during aging. *Elife* **6**, e26652, doi:10.7554/eLife.26652 (2017).
- 118 Chronis, N., Zimmer, M. & Bargmann, C. I. Microfluidics for in vivo imaging of neuronal and behavioral activity in *Caenorhabditis elegans*. *Nat. Methods* **4**, 727-731, doi:10.1038/nmeth1075 (2007).
- 119 Rahman, M. *et al.* NemaLife chip: a micropillar-based microfluidic culture device optimized for aging studies in crawling *C. elegans*. *Sci Rep* **10**, 16190, doi:10.1038/s41598-020-73002-6 (2020).
- 120 Chalfie, M. & Sulston, J. Developmental genetics of the mechanosensory neurons of *Caenorhabditis elegans*. *Dev. Biol.* **82**, 358-370, doi:10.1016/0012-1606(81)90459-0 (1981).
- 121 Hobert, O., Moerman, D. G., Clark, K. A., Beckerle, M. C. & Ruvkun, G. A conserved LIM protein that affects muscular adherens junction integrity and mechanosensory function in *Caenorhabditis elegans*. *J. Cell Biol.* **144**, 45-57, doi:10.1083/jcb.144.1.45 (1999).
- 122 Herndon, L. A. *et al.* Stochastic and genetic factors influence tissue-specific decline in ageing *C. elegans*. *Nature* **419**, 808-814, doi:10.1038/nature01135 (2002).
- 123 Chen, Y., Bharill, S., O'Hagan, R., Isacoff, E. Y. & Chalfie, M. MEC-10 and MEC-19 Reduce the Neurotoxicity of the MEC-4(d) DEG/ENaC Channel in *Caenorhabditis elegans*. *G3 (Bethesda)* **6**, 1121-1130, doi:10.1534/g3.115.023507 (2016).

- 124 Toth, M. L. *et al.* Neurite sprouting and synapse deterioration in the aging *Caenorhabditis elegans* nervous system. *J. Neurosci.* **32**, 8778-8790, doi:10.1523/JNEUROSCI.1494-11.2012 (2012).
- 125 Goodman, M. B., Hall, D. H., Avery, L. & Lockery, S. R. Active currents regulate sensitivity and dynamic range in *C. elegans* neurons. *Neuron* **20**, 763-772, doi:10.1016/s0896-6273(00)81014-4 (1998).
- 126 O'Hagan, R., Chalfie, M. & Goodman, M. B. The MEC-4 DEG/ENaC channel of *Caenorhabditis elegans* touch receptor neurons transduces mechanical signals. *Nat. Neurosci.* **8**, 43-50, doi:10.1038/nn1362 (2005).
- 127 Goodman, M. B., Lindsay, T. H., Lockery, S. R. & Richmond, J. E. in *Methods in Cell Biology* Vol. 107 (eds Joel H. Rothman & Andrew Singson) 409-436 (Academic Press, 2012).
- 128 Nekimken, A. L. *et al.* Pneumatic stimulation of *C. elegans* mechanoreceptor neurons in a microfluidic trap. *Lab Chip* **17**, 1116-1127, doi:10.1039/c6lc01165a (2017).
- 129 Cho, Y. *et al.* Automated and controlled mechanical stimulation and functional imaging in vivo in *C. elegans*. *Lab Chip* **17**, 2609-2618, doi:10.1039/c7lc00465f (2017).
- 130 Cho, Y., Oakland, D. N., Lee, S. A., Schafer, W. R. & Lu, H. On-chip functional neuroimaging with mechanical stimulation in *Caenorhabditis elegans* larvae for studying development and neural circuits. *Lab Chip* **18**, 601-609, doi:10.1039/c7lc01201b (2018).
- 131 Backholm, M., Ryu, W. S. & Dalnoki-Veress, K. Viscoelastic properties of the nematode *Caenorhabditis elegans*, a self-similar, shear-thinning worm. *Proc Natl Acad Sci U S A* **110**, 4528-4533, doi:10.1073/pnas.1219965110 (2013).
- 132 Reina, A., Subramaniam, A. B., Laromaine, A., Samuel, A. D. & Whitesides, G. M. Shifts in the distribution of mass densities is a signature of caloric restriction in *Caenorhabditis elegans*. *PLoS One* **8**, e69651, doi:10.1371/journal.pone.0069651 (2013).
- 133 Chen, Y., Bharill, S., Isacoff, E. Y. & Chalfie, M. Subunit composition of a DEG/ENaC mechanosensory channel of *Caenorhabditis elegans*. *Proc Natl Acad Sci U S A* **112**, 11690-11695, doi:10.1073/pnas.1515968112 (2015).
- 134 Chatzigeorgiou, M. *et al.* Spatial asymmetry in the mechanosensory phenotypes of the *C. elegans* DEG/ENaC gene *mec-10*. *J. Neurophysiol.* **104**, 3334-3344, doi:10.1152/jn.00330.2010 (2010).

- 135 Weicksel, S. E. *et al.* A novel small molecule that disrupts a key event during the oocyte-to-embryo transition in *C. elegans*. *Development* **143**, 3540-3548, doi:10.1242/dev.140046 (2016).
- 136 Le, K. N. *et al.* An automated platform to monitor long-term behavior and healthspan in *Caenorhabditis elegans* under precise environmental control. *Communications Biology* **3**, 297, doi:10.1038/s42003-020-1013-2 (2020).
- 137 Gilpin, W., Uppaluri, S. & Brangwynne, C. P. Worms under Pressure: Bulk Mechanical Properties of *C. elegans* Are Independent of the Cuticle. *Biophys. J.* **108**, 1887-1898, doi:10.1016/j.bpj.2015.03.020 (2015).
- 138 Johnston, I. D., McCluskey, D. K., Tan, C. K. L. & Tracey, M. C. Mechanical characterization of bulk Sylgard 184 for microfluidics and microengineering. *Journal of Micromechanics and Microengineering* **24**, 035017, doi:10.1088/0960-1317/24/3/035017 (2014).
- 139 Wang, Z., Volinsky, A. A. & Gallant, N. D. Crosslinking effect on polydimethylsiloxane elastic modulus measured by custom-built compression instrument. *J. Appl. Polym. Sci.* **131**, n/a-n/a, doi:10.1002/app.41050 (2014).
- 140 Essmann, C. L. *et al.* Mechanical properties measured by atomic force microscopy define health biomarkers in ageing *C. elegans*. *Nat Commun* **11**, 1043, doi:10.1038/s41467-020-14785-0 (2020).
- 141 Mark, J. *Polymer Data Handbook*. *Oxford University Press*, (1999).
- 142 Stirman, J. N. *et al.* Real-time multimodal optical control of neurons and muscles in freely behaving *Caenorhabditis elegans*. *Nat. Methods* **8**, 153-158, doi:10.1038/nmeth.1555 (2011).
- 143 Huang, M. & Chalfie, M. Gene interactions affecting mechanosensory transduction in *Caenorhabditis elegans*. *Nature* **367**, 467-470, doi:10.1038/367467a0 (1994).
- 144 Driscoll, M. & Chalfie, M. The *mec-4* gene is a member of a family of *Caenorhabditis elegans* genes that can mutate to induce neuronal degeneration. *Nature* **349**, 588-593, doi:10.1038/349588a0 (1991).
- 145 Boulin, T., Etchberger, J. F. & Hobert, O. (WormBook, The *C. elegans* Research Community).
- 146 Bolanowski, M. A., Russell, R. L. & Jacobson, L. A. Quantitative measures of aging in the nematode *Caenorhabditis elegans*. I. Population and longitudinal studies of two behavioral parameters. *Mech Ageing Dev* **15**, 279-295, doi:10.1016/0047-6374(81)90136-6 (1981).
- 147 Collins, J. J., Huang, C., Hughes, S. & Kornfeld, K. in *WormBook* (ed The *C. elegans* Research Community) (WormBook).

- 148 Goodman, M. B. *et al.* MEC-2 regulates C. elegans DEG/ENaC channels needed for mechanosensation. *Nature* **415**, 1039-1042, doi:10.1038/4151039a (2002).
- 149 Chelur, D. S. *et al.* The mechanosensory protein MEC-6 is a subunit of the C. elegans touch-cell degenerin channel. *Nature* **420**, 669-673, doi:10.1038/nature01205 (2002).
- 150 Geffeney, S. L. *et al.* DEG/ENaC but not TRP channels are the major mechanoelectrical transduction channels in a C. elegans nociceptor. *Neuron* **71**, 845-857, doi:10.1016/j.neuron.2011.06.038 (2011).
- 151 Liu, J. *et al.* Functional aging in the nervous system contributes to age-dependent motor activity decline in C. elegans. *Cell Metab* **18**, 392-402, doi:10.1016/j.cmet.2013.08.007 (2013).
- 152 Hulme, S. E. *et al.* Lifespan-on-a-chip: microfluidic chambers for performing lifelong observation of C. elegans. *Lab Chip* **10**, 589-597, doi:10.1039/b919265d (2010).
- 153 Huang, C., Xiong, C. & Kornfeld, K. Measurements of age-related changes of physiological processes that predict lifespan of Caenorhabditis elegans. *Proc Natl Acad Sci U S A* **101**, 8084-8089, doi:10.1073/pnas.0400848101 (2004).
- 154 Newell Stamper, B. L. *et al.* Movement decline across lifespan of Caenorhabditis elegans mutants in the insulin/insulin-like signaling pathway. *Aging Cell* **17**, e12704, doi:10.1111/accel.12704 (2018).
- 155 Glenn, C. F. *et al.* Behavioral deficits during early stages of aging in Caenorhabditis elegans result from locomotory deficits possibly linked to muscle frailty. *J Gerontol A Biol Sci Med Sci* **59**, 1251-1260, doi:10.1093/gerona/59.12.1251 (2004).
- 156 Bercovici, M., Han, C. M., Liao, J. C. & Santiago, J. G. Rapid hybridization of nucleic acids using isotachopheresis. *Proc Natl Acad Sci U S A* **109**, 11127-11132, doi:10.1073/pnas.1205004109 (2012).
- 157 Tsourkas, A., Behlke, M. A., Rose, S. D. & Bao, G. Hybridization kinetics and thermodynamics of molecular beacons. *Nucleic Acids Res.* **31**, 1319-1330, doi:10.1093/nar/gkg212 (2003).
- 158 Nunes, L. C. S. Mechanical characterization of hyperelastic polydimethylsiloxane by simple shear test. *Materials Science and Engineering: A* **528**, 1799-1804, doi:10.1016/j.msea.2010.11.025 (2011).
- 159 Cardoso, C., Fernandes, C. S., Lima, R. & Ribeiro, J. Biomechanical analysis of PDMS channels using different hyperelastic numerical constitutive models. *Mechanics Research Communications* **90**, 26-33, doi:10.1016/j.mechrescom.2018.04.007 (2018).

- 160 Tansel, D. Z., Brenneman, J., Fedder, G. K. & Panat, R. Mechanical characterization of polydimethylsiloxane (PDMS) exposed to thermal histories up to 300 °C in a vacuum environment. *Journal of Micromechanics and Microengineering* **30**, 067001, doi:10.1088/1361-6439/ab82f4 (2020).
- 161 Ciarletta, P., Ben Amar, M. & Labouesse, M. Continuum model of epithelial morphogenesis during *Caenorhabditis elegans* embryonic elongation. *Philos Trans A Math Phys Eng Sci* **367**, 3379-3400, doi:10.1098/rsta.2009.0088 (2009).